R. & M. No. 3591

MINISTRY OF TECHNOLOGY

AERONAUTICAL RESEARCH COUNCIL
REPORTS AND MEMORANDA

The Effect of Combined Boundary-Layer Suction and Base Bleed on the Drag of a 10 Degree Cone at M = 2·58

By E. L. GOLDSMITH, N. A. EVANS and G. V. F. SMITH

Aerodynamics Dept. R.A.E. Bedford

LONDON: HER MAJESTY'S STATIONERY OFFICE
1970
PRICE £1 12s od [£1.60]

The Effect of Combined Boundary-Layer Suction and Base Bleed on the Drag of a 10 Degree Cone at M = 2·58

By E. L. Goldsmith, N. A. Evans and G. V. F. Smith

Aerodynamics Dept. R.A.E. Bedford

Reports and Memoranda No. 3591*
August, 1967

Summary

It has been shown experimentally at M = 2·58 that by removing a small quantity of air from the boundary layer through fine slits in the surface of a cone the transition Reynolds number can be increased from its natural value of $2{\cdot}5 \times 10^6$ to 9×10^6. The air sucked from the surface has been discharged into the cone base region and it has been shown that the measured axial force on the body at zero incidence has been reduced over the whole test Reynolds number range ($2{\cdot}5 - 14 \times 10^6$).

CONTENTS

*Replaces RAE Technical Report No. 67218 (A.R.C. 29 946).

---

1. *Introduction*

It is possible to design wing shapes or combinations of wings and bodies which have low wave drag at supersonic speeds. Some of these shapes such as combinations of bodies and complete or half ring wings have very large wetted surface areas. Under these circumstances the skin-friction drag, as at subsonic speeds, becomes a large proportion of the total zero lift drag and hence it becomes important to try to reduce it. Maintaining a laminar boundary layer is one way to decrease skin-friction drag substantially. At supersonic speeds the favourable effect on base pressure of bleeding fairly small quantities of low velocity, low total-head air into a base region is well known. Thus there appears to be a superficial attraction in allowing air to bleed from a body surface to its base to maintain a laminar boundary layer and simultaneously to reduce the base drag.

From the experimental viewpoint there are further advantages. Sucking the laminar boundary layer does not require extensive ducting either inside or outside the wind tunnel together with suction pumps etc. It is also possible to mount the model on a simple axial force balance so that complete measurement of all forces is obtained, including the internal drag due to ducting air from the body surface to the base region.

The experiment described in this Report has been done to explore this possibility of combining a laminar boundary layer with a base bleed using a 5° semi-angle cone followed by a short boattailed portion whose angle was varied from 0° to 9° in steps of 3°. The cone only was slotted and the air was bled directly into its interior and then exhausted back into the tunnel stream at the base of the model. Total axial force, base pressure and total pressure of the flow issuing at the exit were measured. Some traversing of the boundary layer at the end of the 0° boattail model was done to try to separate wake and internal drags.

2. *Design of Slotted Cone*

2.1. *General*

The model consists of a hollow slotted conical forebody followed by an unslotted parallel or boattailed section as shown in Fig. 1. The slots communicate directly through the 0·094 inch thick walls with the hollow interior, the air being exhausted through an annular hole at the base of the model. On any axial station the slots necessarily cannot be continuous right round the circumference. The form of the slots is shown in Fig. 2 and as will be seen the ends of the slots have been arranged in a spiral fashion around the circumference to prevent the build up of end disturbances which might occur if they were on radial lines through the cone tip. The slots were cut using a circular saw and vary in width between 0·004 inch and 0·009 inch. This cone is known as the discrete slot cone.

A continuous slot cone which leads to a far more complex construction was also designed and manufactured but this has not been tested.

2.2. *Calculation of Slot Positions*

The model was designed for an 8 inch × 9 inch supersonic wind tunnel which had fixed nozzles giving Mach numbers of 2·5 and 3·0 and having a total pressure range from approximately half to four atmospheres. From the viewpoint of reflected shocks it was desirable to operate the tunnel at M = 3·0 and the object of the design was to provide natural transition well forward on the cone at the upper end of the stagnation pressure range of the tunnel. The evidence of Ref. 1 suggests (Fig. 3) that natural transition at M = 3·0 and four atmospheres stagnation pressure will be about 3 inches downstream of the cone tip provided the tip radius is kept very small. Thus the first slot was placed at this position and subsequent slot positions were calculated from the following analysis.

For a segment of a cone length ds, radius r:

$$\tfrac{1}{2}\rho V^2 C_f 2\pi r\, ds = \frac{d}{ds}(\rho V^2 2\pi r\theta)\, ds \tag{1}$$

so that

$$\frac{rC_f}{2} = \frac{r\, d\theta}{ds} + \frac{\theta\, dr}{ds}. \tag{2}$$

Now

$$r = s\eta$$

where η is the sine of the cone semi-angle, so that

$$s\frac{d\theta}{ds} + \theta = \frac{s}{2}C_f \tag{3}$$

where for given R_s and a laminar boundary layer the local skin-friction coefficient for a cone

$$C_f = \sqrt{3}\bar{C}_f \tag{4}$$

where $\bar{C}_f$ is the local skin-friction coefficient for a flat plate.

Alternatively

$$C_f = \frac{A}{R_\theta} \tag{5}$$

(where A has the Blasius value of $0{\cdot}664^2$ for incompressible flow but has been modified to $0{\cdot}62^2$ to take into account compressibility effects at M = 3·0) so that equation (5) becomes

$$\frac{d\theta}{ds} + \frac{\theta}{s} = \frac{C_f}{2} = \frac{A}{2R_\theta} \tag{6}$$

or

$$\frac{dR_\theta}{dR_s} + \frac{R_\theta}{R_s} = \frac{A}{2R_\theta}.$$

$$\frac{d}{dR_s}(R_s^2 R_\theta^2) = AR_s^2$$

and hence

$$R_\theta = \left\{\frac{AR_s}{3} + \frac{C}{R_s^2}\right\}^{\frac{1}{2}}. \tag{7}$$

Now provided a small quantity of air is removed at each slot

$$-\rho V^2 \Delta\theta = V m_{sl} \tag{8}$$

where $m_{sl} = \rho v R_{sl}$ and $R_{sl} = Q_{sl}/v$ the slot Reynolds number.

So that

$$-\rho V^2 \Delta\theta = \rho V v R_{sl}$$

or

$$\Delta R_\theta = -R_{sl}. \tag{9}$$

To calculate the slot positions (in terms of R_s) equation (7) can be applied if it is assumed that a slot will be placed just forward of a natural transition position as we proceed downstream from the cone tip. The first slot has been placed at 3·1 inches downstream from the tip in accordance with the data shown in Fig. 3 and subsequent slot positions have been calculated assuming that $R_{\theta_{\text{transition}}} \simeq 600$[1] and slot Reynolds number $R_{sl} = 100$. Applying equation (7):

For the first slot, when $R_\theta = 0$, $R_s = 0$ so that $C_1 = 0$, thus:

$$600 = \frac{0{\cdot}62}{\sqrt{3}} R_{s_1}^{\frac{1}{2}}$$

therefore

$$R_{s_1} = \frac{600^2 \times 3}{0{\cdot}62^2} = 2{\cdot}81 \times 10^6.$$

For the second slot,

$$500 = \left\{\frac{0{\cdot}384 \times 2{\cdot}81 \times 10^6}{3} + \frac{C_2}{(2{\cdot}81 \times 10^6)^2}\right\}^{\frac{1}{2}}$$

therefore

$$C_2 = -6{\cdot}76 \times 10^{18}.$$

Hence for the second slot position:

$$600 = \frac{0{\cdot}62}{\sqrt{3}}\left\{R_{s_2} + \frac{3C_2}{R_{s_2}^2}\right\}^{\frac{1}{2}}$$

therefore

$$R_{s_2} = 3{\cdot}397 \times 10^6$$

and $R_{s_2} - R_{s_1} = 0{\cdot}587 \times 10^6$.

Now if we take a Reynolds number of $0{\cdot}917 \times 10^6$/inch (which corresponds to the M = 3, $P_\infty = 4$ atmospheres condition):

$$\text{Spacing between 1st and 2nd slots} = \frac{0{\cdot}587 \times 10^6}{0{\cdot}917 \times 10^6} = 0{\cdot}64 \text{ inch}.$$

Subsequent slot spacing was calculated in a similar manner.

3. *Models, Apparatus and Test Conditions*

(a) *Models and apparatus*

The model was made up of a conical forebody of 5° semi-angle followed by a short parallel section and then by a conical boattailed section of 0°, 3°, 6° or 9° semi-angle. The whole of the interior of the model was hollow and plugs of differing exit area could be inserted into the rear of the model. The exit plugs and their area are shown in Fig. 4.

For comparison purposes an unslotted forecone was made and this together with a base plug which left only a small clearance around the balance windshield provided a datum case for each boattail angle. The two versions of the forecone are subsequently referred to as the slotted and plain cone models respectively.

As can be seen in Figs. 5 and 6 the model was mounted on an axial force balance. Three pitot rakes at 120° were mounted on the sting windshield to measure base pressure and total pressure of the flow issuing from the annular hole in the base. Some pitot tubes to measure the boundary layer on the external surface of the model were also included in these rakes but were not used for quantitative measurement due to the difficulty of deciding their precise location with respect to the model.

External boundary-layer profiles at the rear of the model were measured however with the rakes shown in Fig. 7 in a separate experiment on the cone-cylinder body only. The rakes were placed in two circumferential positions so that profiles were obtained every 60 deg around the circumference.

(b) *Test conditions*

Tests were made in the 8 inch × 9 inch supersonic tunnel in the High Speed Laboratory at R.A.E. Bedford during 1964 and 1965. This tunnel is of the continuous flow closed circuit type and is powered by a four-stage variable-speed centrifugal compressor. An auxiliary compressor enables the stagnation pressure to be varied up to a maximum of four atmospheres. Mach number is changed by means of replaceable fixed nozzle liners and a nozzle exists for a nominal Mach number of 3·0. The model was designed for testing with this nozzle. At M = 3 the reflected nose shock is well downstream of the model base. Unfortunately before the tests were initiated but after the model had been designed cracks were discovered in the main compressor impeller. These necessitated modifications to the rotor resulting in a deterioration in compressor pressure ratio and reduction in the possible maximum Mach number to about 2·6. At this Mach number the reflected nose shock is just clear of the model base.

Tests were made at total pressures of 20, 35, 50, 65, 80, 95, and 110 inches of Mercury. This gives the Reynolds numbers Re_L (i.e. based on total length L of the model) shown in the following Table, the range at each total pressure being due to small stagnation temperature variations which could not easily be controlled.

P_∞ in Hg	$Re_L \times 10^{-6}$
20	2·653– 2·768
35	4·615– 4·824
50	6·521– 6·791
65	8·362– 8·740
80	10·155–10·601
95	11·873–12·432
110	13·525–14·132

4. *Measurements*

Axial force was measured at zero incidence on a strain gauge balance the output from which was recorded on a standard R.A.E. self-balancing bridge unit. Temperature was measured in the sealed balance chamber by means of a thermocouple to enable the strain gauge readings to be corrected for temperature variation. Balance calibrations were made at the beginning and end of each day's running.

Base pressures and exit total pressures were all measured on a silicon oil manometer with respect to one particular base pressure which was measured absolutely on a standard capsule-type (Midwood) manometer.

The flow was observed with the normal schlieren optical system and transition point could be fairly easily located on top and bottom generators. Some initial experiments were done with the unslotted cone to find transition location all round the circumference by spraying the model with acenaphthene and observing the resulting pattern.

5. *Data Reduction*

5.1. *External Drag*

The forces acting on the model are shown in Fig. 8. The axial force measured on the balance is:

$$F_{\text{balance}} = p_{\text{cone}}A_{\text{cone}} + D_{\text{friction}} + D_{\text{internal}} - p_{\text{base}}A_{\text{base}} - p_{\text{boattail}}A_{\text{boattail}} - p_{\text{sting}}A_{\text{sting}}. \tag{10}$$

We define and present the total drag as the axial force measured on the balance with the sting pressures as measured in the balance chamber corrected to mean base pressure:

$$C_{D_{\text{total}}} = \frac{D_{\text{total}}}{q_\infty S_{\text{total}}} = \frac{F_{\text{balance}} + (p_{\text{sting}} - \bar{p}_{\text{base}})A_{\text{sting}}}{q_\infty S_{\text{total}}}. \tag{11}$$

For the 0° boattail skin friction plus internal drag can be obtained from:

$$C_{D_f} + C_{D_{\text{int}}} = C_{D_{\text{total}}} - C_{D_{\text{cone}}} - C_{D_{\text{base}}} \tag{12}$$

(based on S_{total}) where

$$C_{D_{\text{cone}}} = \left(\frac{p_c}{p_\infty} - 1\right)\frac{A_{\max}}{(q_\infty/p_\infty)S_{\text{total}}}$$

$$-C_{D_{\text{base}}} = \left(\frac{\bar{p}_{\text{base}}}{p_\infty} - 1\right)\frac{A_{\max}}{(q_\infty/p_\infty)S_{\text{total}}}.$$

For the other boattail angles:

$$C_{D_f} + C_{D_{\text{int}}} = C_{D_{\text{total}}} - C_{D_{\text{cone}}} - C_{D_{\text{base}}} - C_{D_{\text{boattail}}} \tag{13}$$

where now

$$-C_{D_{\text{base}}} = \left(\frac{\bar{p}_{\text{base}}}{p_\infty} - 1\right)\frac{A_{\text{base}}}{(q_\infty/p_\infty)S_{\text{total}}}$$

$$-C_{D_{\text{boattail}}} = \left(\frac{\bar{p}_{\text{boattail}}}{p_\infty} - 1\right)\frac{A_{\text{boattail}}}{(q_\infty/p_\infty)S_{\text{total}}}.$$

$C_{D_{\text{boattail}}}$ has been evaluated by the process described in Section 6.2.

5.2. *Accuracy*

The accuracy of the total drag coefficient is mainly dependent on balance accuracy, whilst that of the base drag coefficient is a function of the cumulative errors associated with reading manometers. A Table showing maximum errors which might be expected is shown below:

P_∞ in Hg	Max. % error in $C_{D_{\text{tot}}}$	Max. % error in $C_{D_{\text{base}}}$	Max. % error in $C_{D_f} + C_{D_{\text{int}}}$
20	±2·3	±2·4	±16·5
65	±0·8	±0·8	±8·3
110	±0·6	±0·4	±3·4

5.3. *Internal Drag*

It should be emphasised here that 'internal' drag is probably a misnomer, i.e. it is not what would be obtained by a summation of pressure forces on the internal surfaces of the model. In fact 'internal' drag is defined solely as a quantity which accords with the other drag terms that have been measured or can be calculated so that the total is consistent with the total axial force as measured on the balance.

For simplicity consider the 0° boattail and apply the momentum equation to $ABCDED'C'B'A'$ in Fig. 9 where BC ($B'C'$) defines the dividing surface between flow which is proceeding internally and that which is to continue externally.

The pressure force on $ABCDED'C'B'A'$

$$F = p_\infty A_\infty + \rho_\infty V_\infty^2 A_\infty - p_b A_{ex} - \rho_\infty V_\infty A_\infty V_{ex}. \tag{14}$$

The total drag (as defined in the previous section) is:

$$D_{total} = \bar{p}_s(A_{max} - A_\infty) + D_{wake} - p_b(A_{max} - A_{ex}) + F \tag{15}$$

where $\bar{p}_s$ is the mean static pressure on stream surface BC ($B'C'$).

If it is assumed that $\bar{p}_s \simeq p_c$ the cone surface pressure then

$$D_{total} = p_c A_{max} - p_c A_\infty + p_\infty A_\infty - p_b A_{ex} - p_b A_{max} + p_b A_{ex} + \rho_\infty V_\infty A_\infty (V_\infty - V_{ex}) + D_{wake} \tag{16}$$

$$= (p_c - p_\infty)A_{max} - A_{max}(p_b - p_\infty) + D_{wake} + \rho_\infty V_\infty A_\infty (V_\infty - V_{ex}) - (p_c - p_\infty)A_\infty. \tag{17}$$

Now

$$(p_c - p_\infty)A_{max} = \text{cone wave drag}$$

$$(p_b - p_\infty)A_{max} = \text{base drag}$$

so that,

$$D_{internal} = \rho_\infty V_\infty A_\infty (V_\infty - V_{ex}) - (p_c - p_\infty)A_\infty \tag{18}$$

and hence

$$C_{D_{internal}} = \frac{D_{internal}}{q_\infty S_{total}} = \frac{2A_\infty}{S_{total}} - \frac{2q_{ex}}{q_\infty}\frac{A_{ex}}{S_{total}} - \frac{[(p_c/p_\infty) - 1]A_\infty}{(q_\infty/p_\infty)S_{total}}. \tag{19}$$

Now

$$C_Q = \frac{m_{ex}}{\rho_\infty V_\infty S_{cone}} = \frac{A_\infty}{S_{cone}}$$

and for a cone semi-angle of 5° at M = 2·58 $p_c/p_\infty = 1{\cdot}029$, so that

$$\frac{[(p_c/p_\infty) - 1]A_\infty}{(q_\infty/p_\infty)S_{total}} = 0{\cdot}029\, C_Q \times \frac{S_{cone}}{S_{total}} \tag{20}$$

therefore

$$C_{D_{internal}} = 1{\cdot}971\, C_Q \frac{S_{cone}}{S_{total}} - \frac{(2q_{ex}/P_{ex}).(\bar{P}_{ex}/P_\infty).(P_\infty/p_\infty).(A_{ex}/S_{total})}{q_\infty/p_\infty}. \tag{21}$$

Internal drag can also be obtained from equation (17) if D_{wake} is measured by boundary-layer traverses.

5.4. *Exit Mass Flow, Total Pressure and Mach Number*

Mass flow through the model has been evaluated from the measurement of total pressure at the exit plane and base pressure.

From continuity:

$$P_\infty A^*_\infty f(T_{t_\infty}) = P_{ex} A^*_{ex} f(T_{t_{ex}}). \tag{22}$$

Assuming total temperature of the flow through the model remains constant, then:

$$\frac{\rho_\infty V_\infty A_\infty}{\rho_\infty V_\infty S_{cone}} = \frac{m_{ex}}{\rho_\infty V_\infty S_{cone}} = C_Q = \frac{P_{ex}}{P_\infty} \cdot \frac{A^*_{ex}}{A^*_\infty} \cdot \frac{A_\infty}{S_{cone}}$$

$$= \frac{P_{ex}}{P_\infty} \cdot \frac{A^*_{ex}}{A_{ex}} \cdot \frac{A_\infty}{A^*_\infty} \cdot \frac{A'_{ex}}{S_{cone}} \tag{23}$$

where A'_{ex} is the annular area $A_{ex} - A_{sting}$.

Thus for each rake m_{ex} and hence A^*_{ex}/A_{ex} have been evaluated from $\bar{P}_{ex_1}/\bar{p}_{b_1}$, $\bar{P}_{ex_2}/\bar{p}_{b_2}$ etc. and flow tables where $\bar{P}_{ex_1}$, $\bar{p}_{b_1}$ etc. are arithmetic mean values. Thus finally

$$C_Q = \left\{ \frac{1}{3} \left[\sum_{1-3} \left(\frac{A^*_{ex}}{A_{ex}} \right)_n \cdot \frac{\bar{P}_{ex_n}}{P_\infty} \right] \frac{A'_{ex}}{S_{cone}} \cdot \frac{A_\infty}{A^*_\infty} \right\}. \tag{24}$$

6. *Discussion of Results*

6.1. 0° *Boattail Angle—General*

Results are quoted in detail for the basic model. A number of tests for the 0° boattail angle were done with the parallel section extended 0·5 inch (Fig. 4) so that the reflected shock impinges on the model just upstream of the base. This does not appear to have any systematic effect on the values for C_{D_f} (plain cone) or $C_{D_f} + C_{D_{int}}$ (vented cone) but does have a sizeable effect on $C_{D_{total}}$ due to corresponding changes of base pressure. Values of C_{D_f} or $C_{D_f} + C_{D_{int}}$ are quoted for both with and without extension because this leads to better definition of the variation of this quantity with Reynolds number.

6.2. *Plain and Unvented Slotted Cones* (0° *Boattail Angle*)

Measured values for $C_{D_{total}}$, C_{D_f}, base pressure and transition point position (on the top generator of the cone) are shown plotted *versus* Reynolds number (based on total length) in Fig. 10. The unvented slotted cone results were obtained using exit plug 1 with a plasticine plug placed at a suitable section around the central body and support struts so that no flow could pass through the model. There appears to be a tendency for this configuration to give slightly higher values for C_{D_f} than the plain cone. The schlieren evidence indicates that transition is in a similar position, so that the difference is probably due to a small increase in cone wave drag caused by the presence of the open slots.

The variation of transition Reynolds number (based on local cone flow conditions) with free stream Reynolds number per foot is shown compared to some other cone results in Fig. 11. Nose radius was kept as small as possible (0·002 inch) so that transition would occur on the cone at the lower end of the Reynolds number range so that the effect of suction could be adequately demonstrated. However the transition pattern is rather uneven around the circumference (as shown by the photographs of Fig. 12, taken using acenaphthene as an indicator) probably due to either the presence of a small disturbance from a window joint or to small angle variation of the incident airflow.

The uneven transition pattern shown in Fig. 13 should be borne in mind when assessing the schlieren results for determining transition 'point' location. As can be seen from Fig. 14 the schlieren result can be optimistic particularly at the higher Reynolds numbers.

The variation of C_{D_f} with Reynolds number is compared with other experimental measurements in Fig. 15 and effectively illustrates the same point. The boundary layer is probably not fully laminar even at the lowest Reynolds number due to premature transition over part of the circumference. This has the effect of spreading out the transitional part of the C_{D_f} *versus* Reynolds number curve when compared to other experimental results.

This uneven pattern of boundary-layer condition around the periphery is also well illustrated by the results from the fixed rake traverses shown in Fig. 16: the distribution of skin friction now being the inverse

of the transition pattern (as shown typically at $Re_L = 6{\cdot}5 \times 10^6$). As can be seen good agreement between rake traverse and force measurements has been obtained for the variation of C_{D_f} with Reynolds number.

6.3. *Vented Slotted Cones* (0° *Boattail Angle*)

Detail results (i.e. $C_{D_{total}}$, $C_{D_f} + C_{D_{internal}}$, transition location, mass flow, base pressure and flow conditions at the model exit) are presented for plugs 1, 1B, 2, 4 and 6 in Figs. 17 to 21.

It is immediately apparent that base bleed achieves laminar flow over the whole of the model up to a Reynolds number of about 8×10^6 and over the slotted cone up to a Reynolds number of about 9×10^6 irrespective of exit area at the base. In fact there is little systematic change with exist area (Fig. 22) except apparently in mass flow and exit velocity. Discussion of changes of total drag, skin friction plus internal drag, mass flow and base pressure will be made under appropriate section headings.

As can be seen there is some scatter on repeat tests leading to fairly large variations of skin friction plus internal drag. This is mainly because this quantity is of course the difference between two large measured quantities $C_{D_{total}}$ and $C_{D_{base}}$ (*see* Section 5.2). An inconsistency in results for plug 2 will be noted (Fig. 19) where there is evidently a difference in transition Reynolds number between results with and without the 0·5 inch parallel extension to the model. Other repeat results (not quoted) with other exit areas showed even larger discrepancies in transition Reynolds number the cause of which was found to be a very slightly bent tip to the model. This caused premature transition so that no laminarisation was achieved. It will be recalled that the tip radius was deliberately made as small as practically possible to ensure that natural transition Reynolds numbers were not too high, so that the model was particularly prone to distortion of this kind.

It is interesting to compare these results (as regard amount of laminar flow) with results obtained in Refs. 5 and 6 (Figs. 23 and 24). These latter tests have all been on the same shape of model (an ogive cylinder model) which has been developed in three series of experiments to give finally (in the latest series) transition Reynolds numbers of 51×10^6 at M = 3 (Fig. 24). The main difference in the two configurations apart from the obvious ones of body profile and suction-slot shape (continuous circumferential slots in Refs. 5 and 6 as opposed to the discrete slots of the present model) was the ratio of slot area to total surface area which was slotted as indicated on Fig. 23.

The failure of the present tests to extend laminarisation beyond about a Reynolds number of 9×10^6 could be due to:

(1) influence of window disturbance,
(2) influence of reflected nose shock,
(3) 'end effects' of slots,
(4) incorrect spacing and/or sizing of slots.

The first two reasons could be checked by testing the model in a different, preferably larger, tunnel. The third, by testing the continuous slot cone referred to in Section 2.1. This has slots which vary in width form 0·002 inch to 0·003 inch and has a value of $\frac{\text{Slot area}}{\text{Total surface area which is slotted}}$ of 0·00525.

Comparison of total drag, skin friction plus internal drag and base pressure for slotted and plain cones is shown in Fig. 25. As can be seen the maximum reduction in skin-friction drag due to laminarisation has been obtained when the difference in total drag is a minimum. This anomalous result is of course due to the corresponding base pressure changes. When the Reynolds number is 7 to 8×10^6 the boundary layer for the slotted cone is all laminar over the whole model but obviously transition takes place just downstream of the base and before the closure of the base flow region. Hence the re-attachment and trailing shock regions are associated with a very thin turbulent layer which leads to the low base pressure recorded. For the plain cone on the other hand a similar condition in the base flow occurs at a much lower Reynolds number (around $2{\cdot}5 \times 10^6$); at a Reynolds number of 7 to 8×10^6 the boundary-layer transition is about $\frac{1}{4}$ to $\frac{1}{3}$ of the cone length from the tip so that the turbulent layer is considerably thicker in the base region and hence the base pressure is higher. Eventually at higher Reynolds numbers the boundary layer is all turbulent over the cone surface and base pressure will fall gradually in the normal way as the turbulent boundary layer progressively get thinner.

6.3.1. *Mass flow.* As noted in Section 5 mass flow has been evaluated from an arithmetic mean of each set of total pressure and base pressure data. Radial and circumferential variations of exit Mach number based on these measured pressure data are shown in Figs. 26 and 27. As can be seen, the variations both radially and circumferentially are small for small plug exit area but both distributions (circumferential in particular) get considerably worse as exit area increases and mean Mach number decreases. Even on this basis it would be possible to throw considerable doubt on the true mass flow. For instance a lower bound to the value could be obtained by assuming that the low value of M_{ex} measured on one rake was applicable to $\frac{2}{3}$ of the circumference (Fig. 28).

However if the rake and base pressure distributions are studied (Fig. 29) it will be seen that there are further possibilities of uncertainty, particularly for the larger exit sizes due to the uneven distribution of base pressure. Comparisons of the distribution of C_Q around the circumference based on taking the mean base pressure or the base pressure nearest to the issuing flow are shown in Fig. 30 and lead to the variations of mean C_Q with exit area for the two assumptions shown in Fig. 31. Thus the sum total of this evidence would suggest that the large increase in mass flow through the model with increasing exit area noted in Fig. 22 is probably much less in actual fact or put another way, the mass flow measurements are probably only reasonably reliable at small exit areas and high exit velocities where the distributions are fairly uniform.

This conclusion is supported by the balance and external boundary-layer traverse results (considered in the next Section) which indicate that internal drag is practically invariant with exit area.

6.3.2. *Skin friction and internal drag.* Results from traverse and force tests for plugs 2, 4 and 6 are shown in Figs. 32a to c. The slotted cone gives a roughly constant difference between force and traverse results, which (as was seen in Section 5) is defined as the internal drag. For plug 2 this roughly coincides with calculated values for internal drag using measured values for C_Q and exit Mach number. However this agreement gets progressively worse as exit area is increased (plugs 4 and 6). As has been seen most of this discrepancy is probably due to progressively large errors in measurement of C_Q. Indeed on this evidence it would suggest that C_Q is 0·0003 to 0·0005 irrespective of exit area.

When the flow is laminar over the whole model the traverse values should compare with calculated values which lie somewhere between the two curves shown. The top curve is the laminar skin-friction drag for the complete model which is approximately (from Ref. 3)

$$C_{D_{f\,\text{cone-cylinder}}} = \frac{1{\cdot}24 \times 2}{\sqrt{3\,\mathrm{Re}_L}} \frac{\sqrt{(l_c + l_p)(l_c + 3l_p)}}{l_c + 2l_p}^{*}$$

and the bottom is the laminar skin-friction drag for the cylindrical portion taken in isolation:

$$C_{D_{f\,\text{cyl. portion}}} = \frac{1{\cdot}24}{\sqrt{\mathrm{Re}_{l_p}}} \times \frac{2l_p}{l_c + 2l_p} \cdot \frac{q_l}{q_\infty}$$

which corresponds to the case of the laminar boundary layer on the cone being sucked away completely.

6.3.3. *Base pressure.* A general qualitative explanation of the reasons for the variation of base pressure with Reynolds number has already been given. Variation of base pressure with boundary-layer momentum thickness is shown in Fig. 33 and illustrates the favourable effect of the base flow on the turbulent boundary-layer base pressure.

As can be seen from Fig. 34 base pressure in this experiment appears to be consistently higher than would be inferred from other experimental results. The only explanation for this would appear to be the presence of the reflected nose shock in the region of the base.

6.4. *Boattail Angles of* 3°, 6° *and* 9°

6.4.1. *General.* These variations of boattail angle were undertaken primarily to see if, having reduced the total drag of a high drag body (i.e. cone plus cylinder) by laminarisation, it was possible to

*Kinetic pressure changes have been ignored.

do the same for a lower drag body obtained by replacing some of the base area by boattail area. The combination of boattail and base area would also increase the base pressure so that it was interesting to see if the laminarisation would still operate with the reduced pressure difference.

6.4.2. *Plain cone.* Variation of total drag with Reynolds number and with boattail angle for constant Reynolds number is shown in Figs. 35 and 36. As can be seen the reduction in total drag with increasing boattail angle is in general small. This is primarily due to the unrepresentatively low base drag that was obtained for the 0° boattail. To breakdown the drag into its components it is necessary to assume that the skin-friction drag for the 3°, 6°, and 9° configurations is the same (with a small correction for change of wetted area) as for the 0° configuration. Boattail and base drags are shown separately in Fig. 37 and their sum in Fig. 38a. As can be seen the boattail drag does not agree well with estimates above a boattail angle of about 4°. The estimates have been made using the methods suggested in Ref. 9. In this, boattail pressure coefficient is considered to be:

$$C_{p_A} = C_{p_{A_1}} + C_{p_{A_2}} + \Delta C_{p_{BL}}$$

where $C_{p_{A_1}}$ is the pressure coefficient on the boattail alone (i.e. when it is situated behind an infinitely long parallel portion)

$C_{p_{A_2}}$ is the pressure coefficient which would exist at the axial station in question on a parallel portion extended into the region of the boattail

$\Delta C_{p_{BL}}$ is an empirical correction which gives some indication of the magnitude of the boundary-layer effects.

In this calculation $C_{p_{A_1}}$ is based on quasi-cylinder linear theory and three characteristic solutions (as given in Ref. 9). $C_{p_{A_2}}$ is taken from characteristic solutions (interpolated for Mach number) from Ref. 10. $\Delta C_{p_{BL}}$ is also given in Ref. 9.

Variation of base pressure with boattail angle (Fig. 38b) appears to agree quite well with estimates made using the simple method of Ref. 11.

6.4.3. *Vented slotted cone.* In order to extract skin friction plus internal drag from the force and pressure measurements, boattail drag has to be estimated. As was seen from the plain cone results the boattail drag is (as expected) smaller for laminar boundary layers than for turbulent boundary layers (Fig. 37). Using the amount of laminarisation obtained with no boattail as a guide, curves of boattail drag variation with Reynolds number (Fig. 39) have been produced. These have been used to obtain the detailed breakdown of the total drag into its component parts given in Figs. 40 to 48. Similar amounts of laminarisation for these boattailed versions are indicated but the results are less consistent than for the 0° boattail. For instance no consistent trend with exit area is observable. Summary plots comparing vented and plain cones for arbitrarily chosen exit areas are shown in Figs. 49 to 51.

No boundary layer traverses were made with the boattailed models.

In summary, it has been shown that similar amounts of laminarisation with boattailed versions of the model have been obtained even with base pressures that approach free stream static pressure but under these conditions values for $C_{D_f} + C_{D_{\text{int}}}$ are consistently higher than for 0° boattail. However this latter result may be only a reflection of inaccuracies in obtaining component drags (notably boattail drag).

7. *Conclusions*

It has been demonstrated experimentally at M = 2·58 that:

(1) by taking air from the surface of a cone *via* a number of fine slots and exhausting it into the base area, boundary layer transition over the total length of the cone has been delayed from a unit Reynolds number of about 2×10^6 (plain cone) to $6{\cdot}5 \times 10^6$,

(2) over the whole test Reynolds number range (2·5 to 14×10^6) the total drag of the complete body (slotted cone plus afterbody) has been reduced by using the process referred to in (1). This reduction is a combination of reduced external skin friction, the addition of an internal drag and changes caused to base drag. These latter changes can be dominant and are a result of the external boundary-layer changes

(laminar or turbulent boundary layers and variation of transition location) and the effect of the air discharging into the base region (base bleed).

Further experimental work is required to determine the reason for the failure of this simple method of laminarisation to continue above a Reynolds number of $6{\cdot}5 \times 10^6$/foot. More study of the interaction of laminarisation and base bleed is required before the best combination of these two effects can be achieved to give the maximum reduction in total drag of a complete body.

Small distortions at the tip of the cone cause an almost complete breakdown of the laminarisation and hence it is conjectured that incidence could well have a similar effect. Thus it is recommended that further work of this nature might best be done on the undersurface of a shape such as a caret wing.

Acknowledgement

The authors wish to acknowledge helpful discussions with Mr. B. Edwards of Handley-Page Ltd. during design of the model and analysis of results.

LIST OF SYMBOLS

A	Cross-sectional area (square inches)
C_D	Drag coefficient
C_Q	Mass flow coefficient
D	Drag
L	Total length of body (15·86 inches)
l_p	Length of parallel section afterbody, i.e. $L - l_c$
M	Mach number
l_a	Afterbody length on boattailed models
P	Total pressure
p	Static pressure
q	Kinetic pressure
r	Radius
Re	Reynolds number (based on free stream conditions)
S_{total}	Total surface area (excluding base area)
T_t	Total temperature
V	Velocity
x	Axial length (from nose)
ε	Boattail angle
β	Cone angle
ρ	Density
ϕ	Circumferential position
θ	Momentum thickness

$()_b$	Base
$()_\infty$	Free stream
$()_f$	Friction
$()_t$	Transition
$()_{int}$	Internal
$()_{ex}$	Exit
$()_{bt}$	Boattail
$()_c$	Cone
$()_s$	Slot
$()_l$	Local

REFERENCES

No.	*Author(s)*	*Title, etc.*
1	R. H. Rogers	The effect of tip bluntness on boundary-layer transition on a 15° included angle cone at M = 3·12 and 3·81. A.R.C. C.P. 598 (1959).
2	E. R. Van Driest and C. B. Blumer	Effect of roughness on transition in supersonic flow. AGARD Report 255.
3	J. L. Potter	New experimental investigations of friction drag and boundary layer transition on bodies of revolution at supersonic speeds. NAVORD Report 2371, P. 50199 (1952).
4	M. W. Rubesin, R. C. Maydew and S. A. Varga	An analytical and experimental investigation of the skin friction of the turbulent boundary layer on a flat plate at supersonic speeds. NACA Technical Note 2305.
5	W. T. Strike and S. Pate ..	Investigation of boundary layer suction on a 20-calibre ogive-cylinder at Mach numbers 2·5, 3·0, 3·5 and 4·0. AEDC-TN-61-66, P. 95568.
6	—	Recent developments in boundary layer research Part IV. AGARDograph 97
7	J. Reid and R. C. Hastings ..	Experiments on the axi-symmetric flow over afterbodies and bases at M = 2·0. R.A.E. Report Aero 2628, (A.R.C. 21707) (1959).
8	J. O. Reller, Jr. and F. M. Hamaker	An experimental investigation of the base pressure characteristics of non lifting bodies of revolution at Mach numbers from 2·73 to 4·98. NACA/TIL/3378.
9	L. E. Fraenkel	A note on the estimation of the base pressure on bodies of revolution at supersonic speeds. R.A.E. Technical Note Aero 2203, (A.R.C. 15913) (1952).
10	R. F. Clippinger, J. H. Giese and W. C. Carter ..	Tables of supersonic flows about cone cylinders. Part II Complete flows. U.S.A. BRL Report 730 (1950).
11	E. M. Cortright and A. H. Schroeder	Investigation at Mach number of 1·91 of side and base pressure distributions over conical boattails without and with jet flow issuing from base. NACA/TIB/2863 (1951).

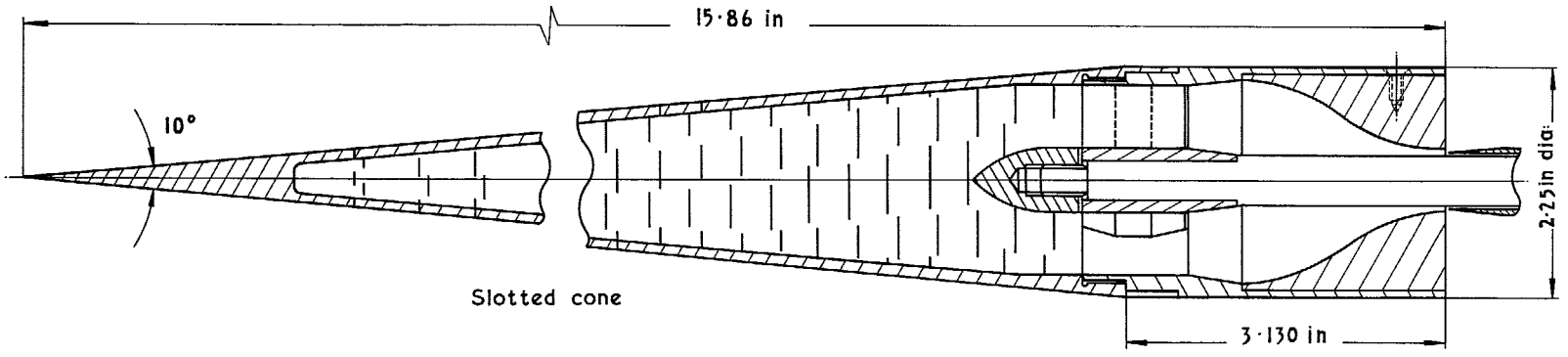

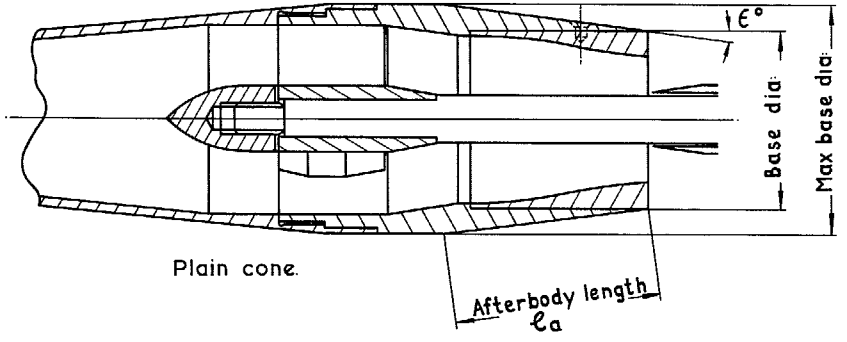

ϵ	Base dia in ins.	A base / A max	A max / A wet tot.	ℓ_a in
0	2·25	1·000	0·0593	2·370
3	2·00	0·790	0·0598	2·391
6	1·75	0·605	0·0608	2·378
9	1·50	0·444	0·0616	2·385

FIG. 1. Assembly details of plain and slotted cones showing parallel and angled afterbodies.

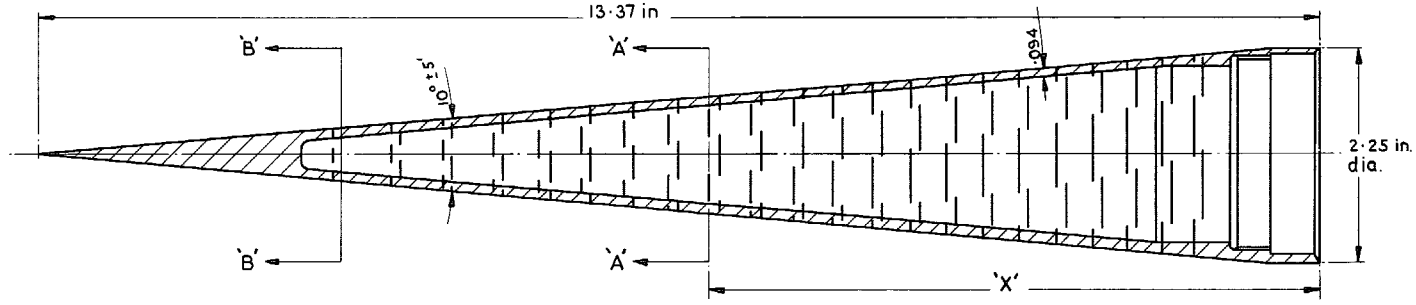

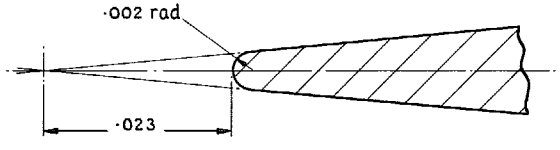

ENLARGED VIEW OF TIP

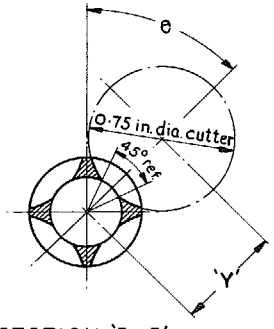

SECTION 'B-B'
Used on stations 1 & 2 only
Scale 2/1

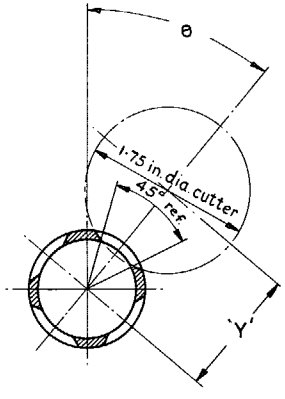

SECTION 'A-A'

STN	'X'	'Y'	θ°	STN	'X'	'Y'	θ°	STN	'X'	'Y'	θ°
1	10·262	·534	0	16	6·615	1·314	80	31	3·488	1·536	75
2	10·162	·541	45	17	6·297	1·337	40	32	3·388	1·543	120
3	9·614	1·092	5	18	6·197	1·344	85	33	3·109	1·562	80
4	9·514	1·100	50	19	5·879	1·367	45	34	3·009	1·569	125
5	9·066	1·129	10	20	5·779	1·374	90	35	2·711	1·589	85
6	8·966	1·137	55	21	5·460	1·398	50	36	2·611	1·596	130
7	8·538	1·170	15	22	5·360	1·404	95	37	2·332	1·615	90
8	8·438	1·177	60	23	5·042	1·427	55	38	2·232	1·621	135
9	8·060	1·206	20	24	4·942	1·434	100	39	1·954	1·640	95
10	7·960	1·214	65	25	4·653	1·455	60	40	1·854	1·646	140
11	7·612	1·240	25	26	4·553	1·462	105	41	1·595	1·652	100
12	7·512	1·247	70	27	4·245	1·484	65	42	1·495	1·652	145
13	7·164	1·274	30	28	4·145	1·490	110	43	1·266	1·652	105
14	7·064	1·280	75	29	3·876	1·509	70	44	1·166	1·652	150
15	6·715	1·306	35	30	3·776	1·515	115				

FIG. 2. Details of slots in hollow cone.

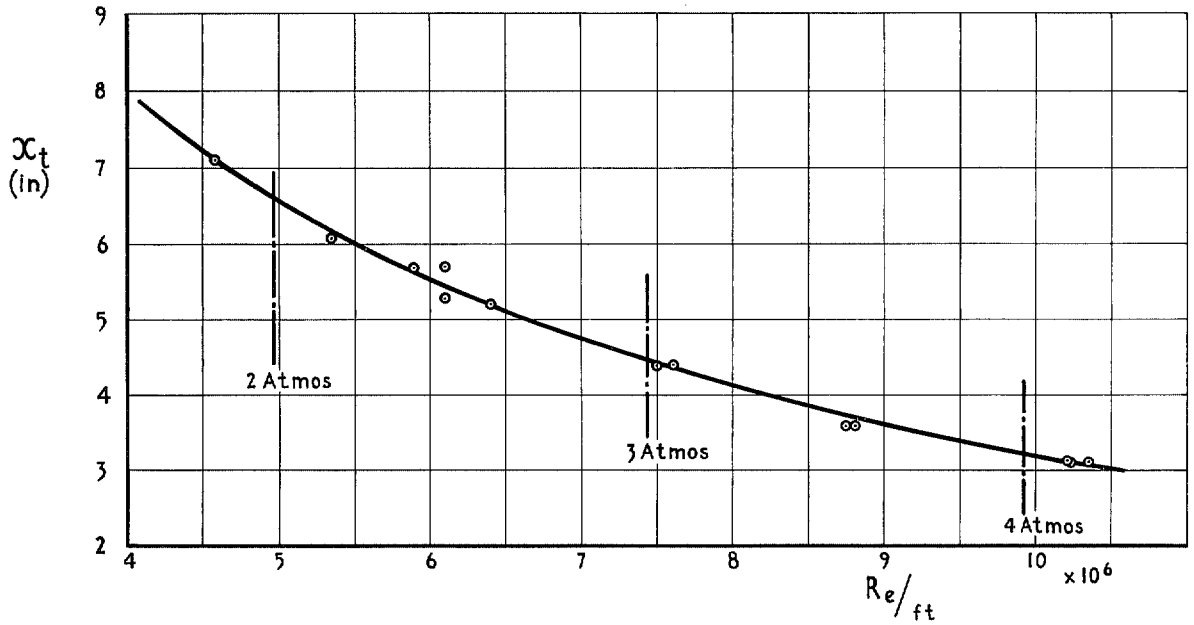

FIG. 3. Variation of transition position for $\beta = 7{\cdot}5°$ cone at M = 3·00 (Ref. 1).

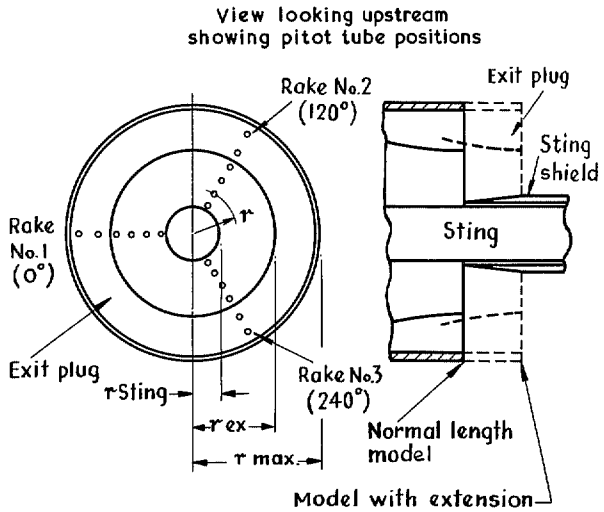

Location of individual pitot tubes		
Rake No1. r in.	Rake No.2 r in.	Rake No.3 r in.
0·319	0·348	0·366
0·437	0·447	0·481
0·625	0·647	0·650
0·791	0·833	0·794
0·914	0·949	0·925
1·040	1·075	1·020

Boat-tail Number	Angle $\epsilon°$	Plug No.	Plug exit radius r ex in	A_{ex}/A_{max} no extension	A_{ex}/A_{max} with extension
1	0°	1	0·350	0·0370	0·0123
		1B	0·430	0·0863	0·0616
		2	0·470	0·1148	0·0901
		3	0·589	0·2143	0·1896
		4	0·667	0·2917	0·2670
		5	0·761	0·3977	0·3731
		6	0·837	0·4937	0·4691
		7	0·937	0·6339	0·6092
2	3°	1	0·285	0·0044	
		2	0·421	0·0802	
		3	0·523	0·1563	
		4	0·608	0·2323	
		5	0·682	0·3077	
		6	0·750	0·3846	
3	6°	1	0·285	0·0044	
		2	0·421	0·0802	
		3	0·523	0·1563	
		4	0·608	0·2323	
		5	0·682	0·3077	
		6	0·750	0·3846	
4	9°	1	0·285	0·0044	
		2	0·429	0·0857	
		3	0·536	0·1672	
		4	0·625	0·2488	

r Sting = 0·25 in
r max = 1·125 in.

FIG. 4. Base and afterbody details for various model configurations.

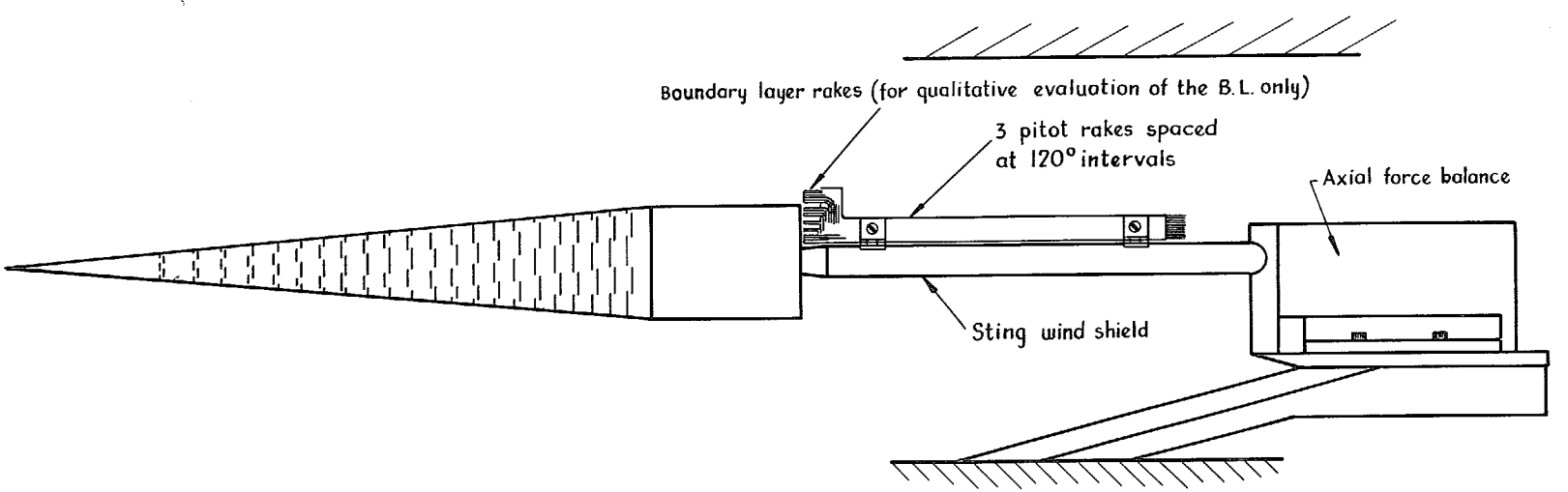

FIG. 5. General assembly of model on axial force balance.

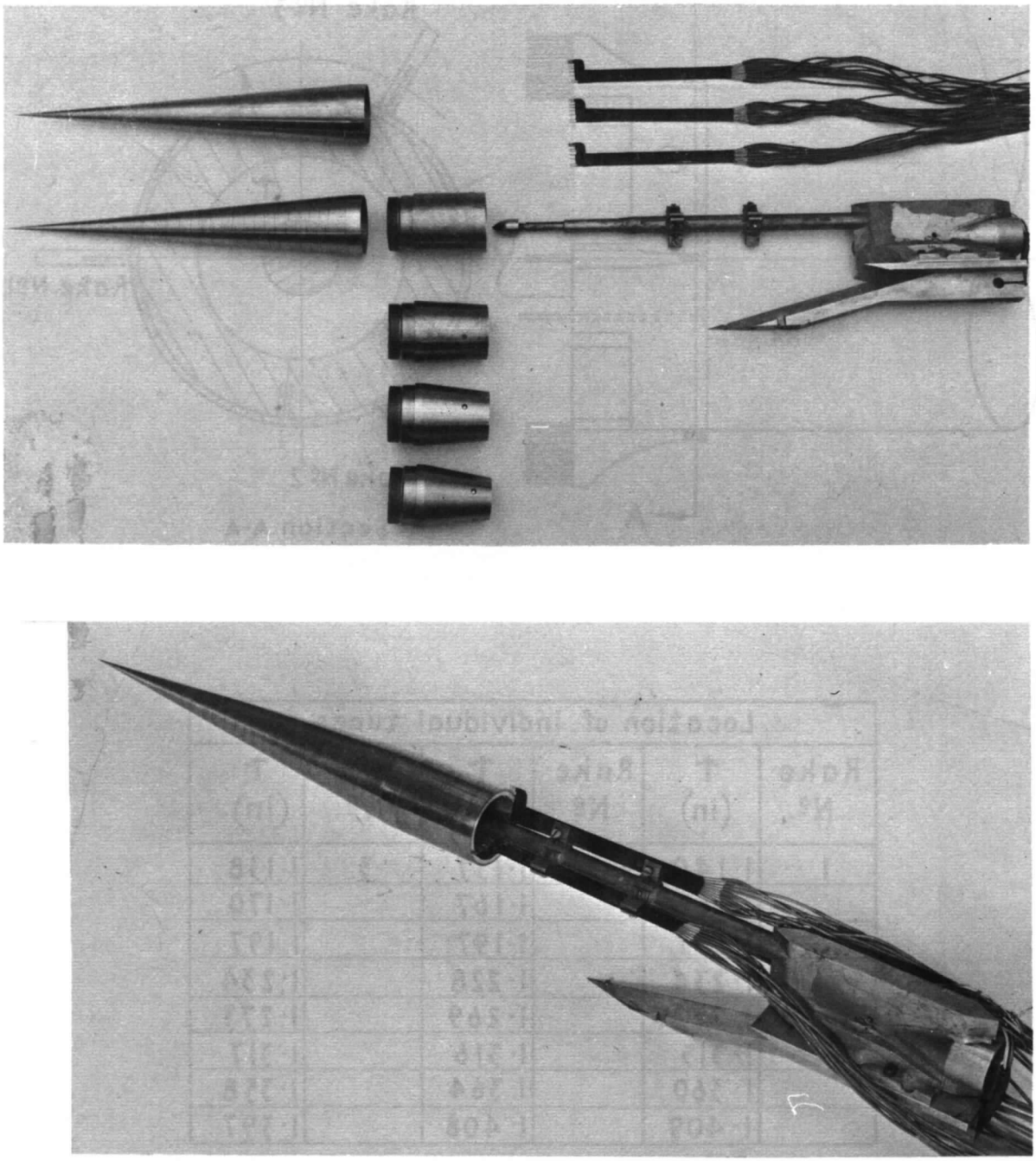

FIG. 6. Model assembly and support details.

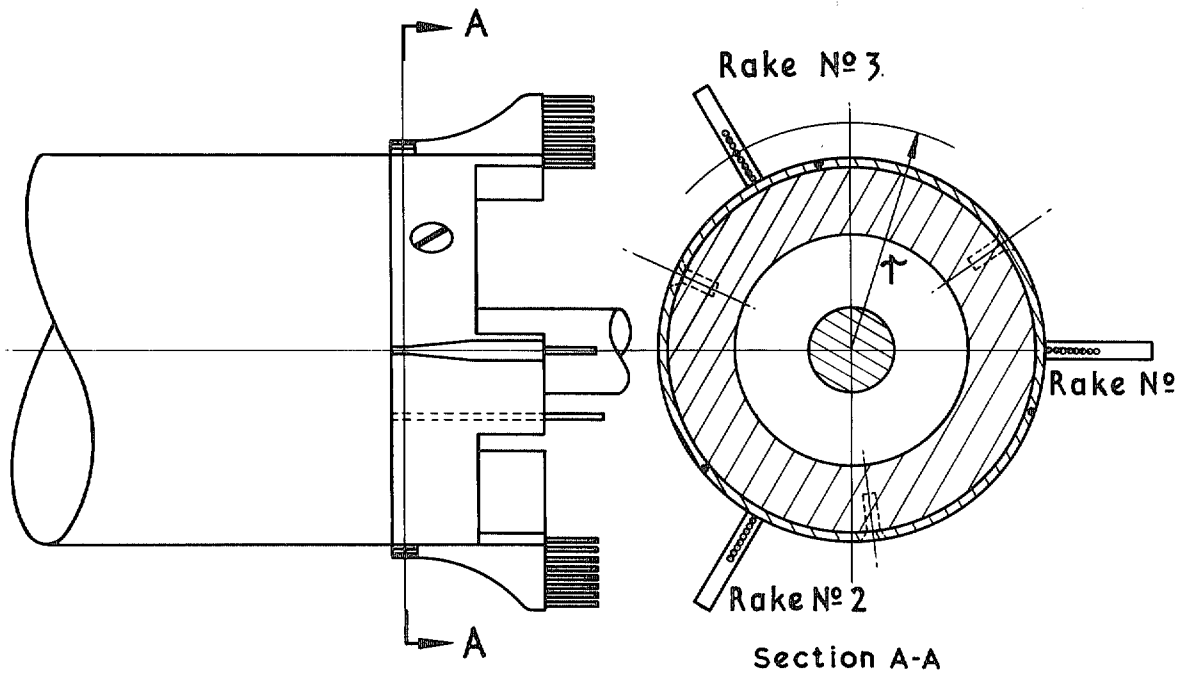

Location of individual tubes					
Rake Nº	↑ (in)	Rake Nº	↑ (in)	Rake Nº	↑ (in)
1	1·140	2	1·137	3	1·138
	1·168		1·167		1·170
	1·197		1·197		1·197
	1·234		1·228		1·234
	1·272		1·269		1·273
	1·315		1·316		1·317
	1·360		1·364		1·358
	1·409		1·408		1·397

FIG. 7. Boundary layer traverse rakes.

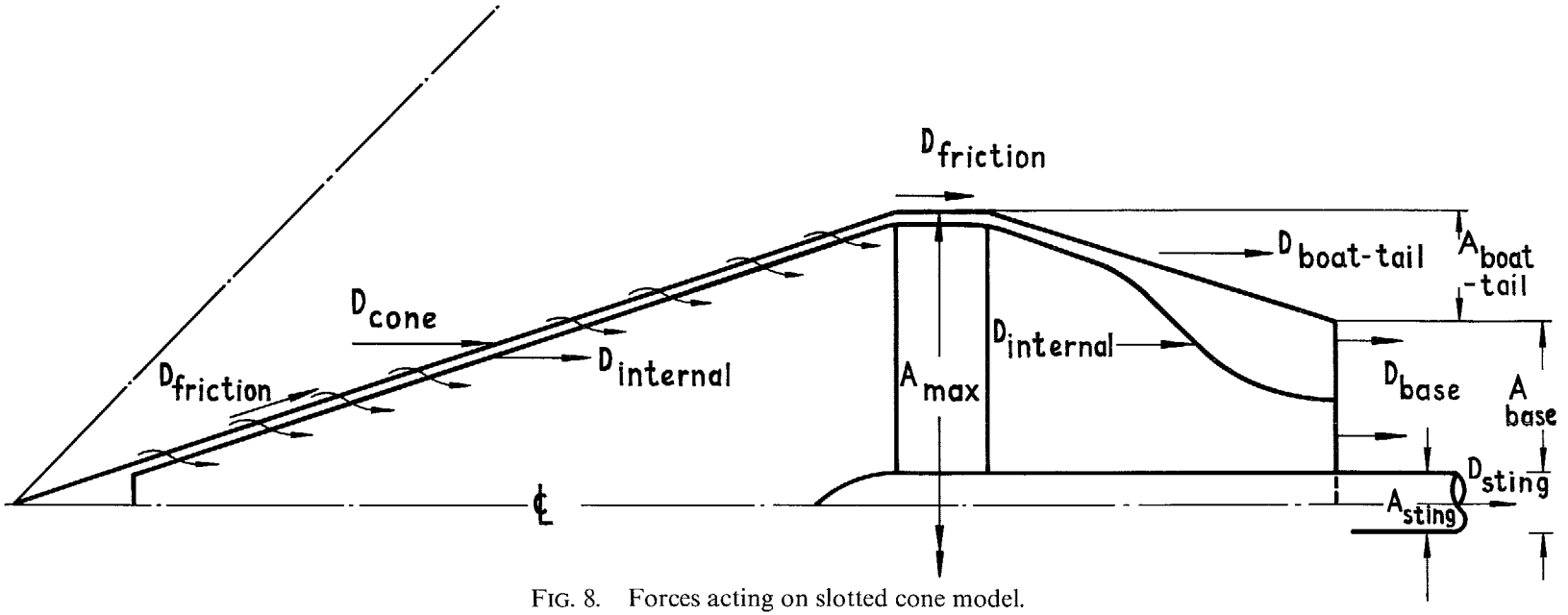

FIG. 8. Forces acting on slotted cone model.

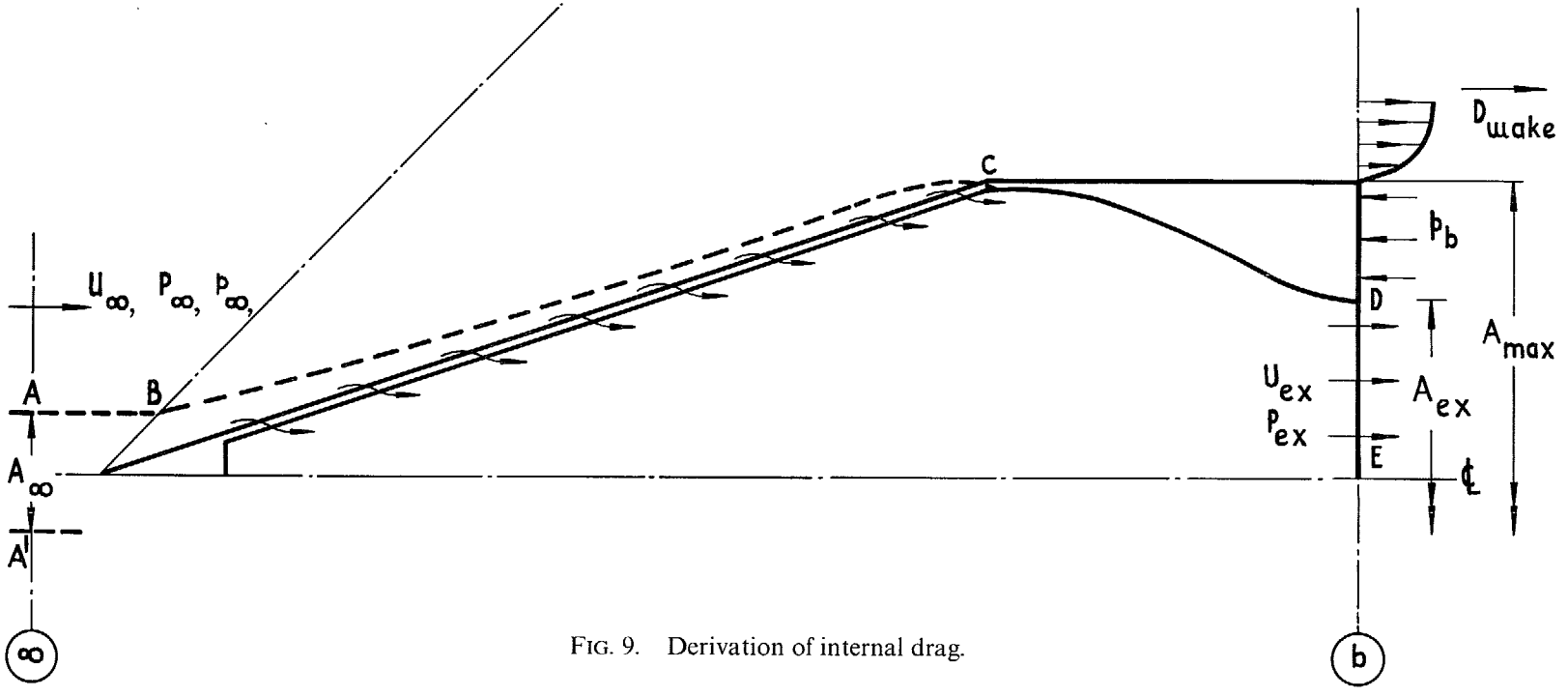

FIG. 9. Derivation of internal drag.

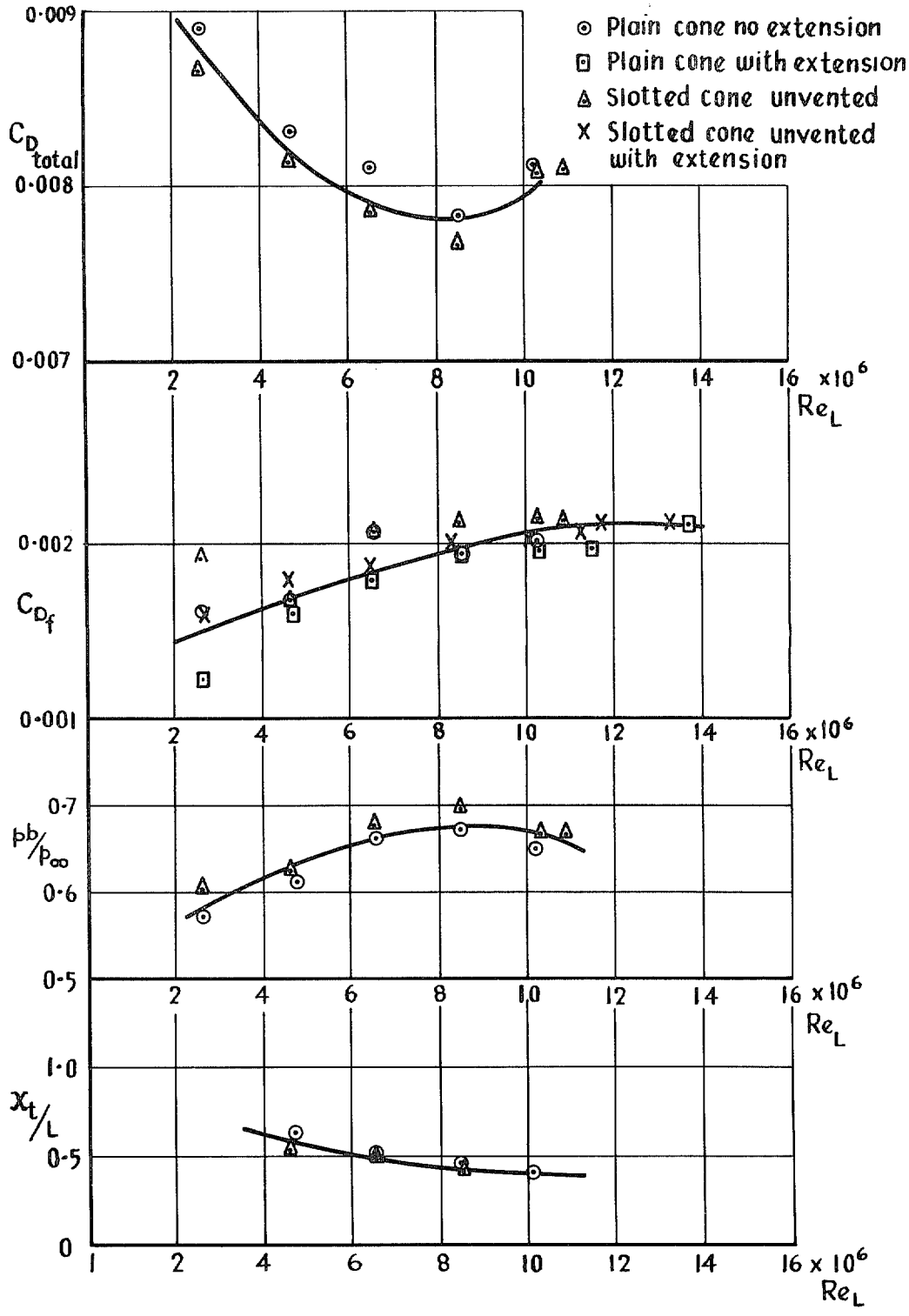

FIG. 10. Variation of $C_{D_{total}}$, C_{D_f} base pressure and transition location with Reynolds no. for plain and unvented slotted cones.

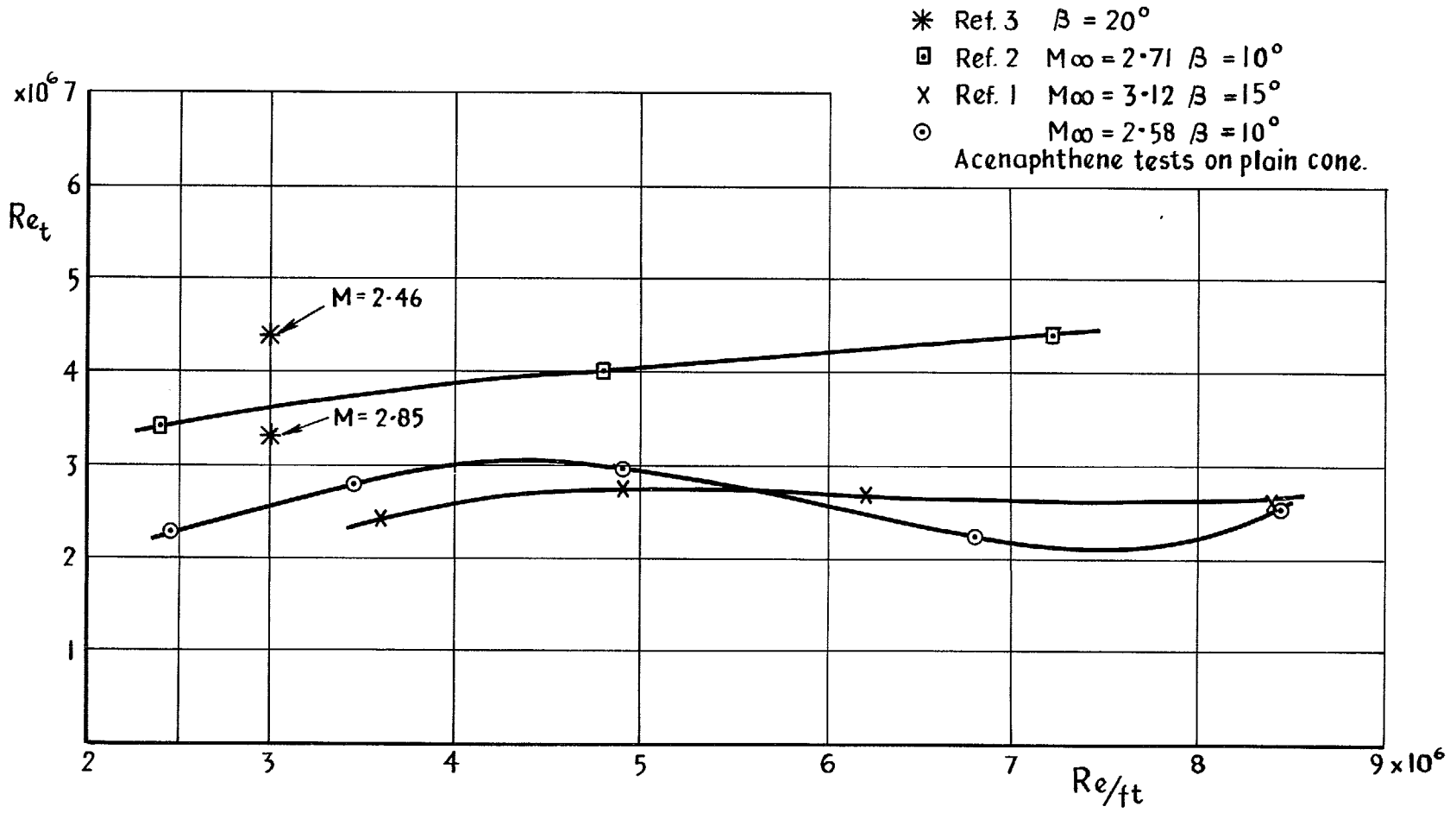

FIG. 11. Variation of transition Reynolds no. with Reynolds no. per ft: comparison of data.

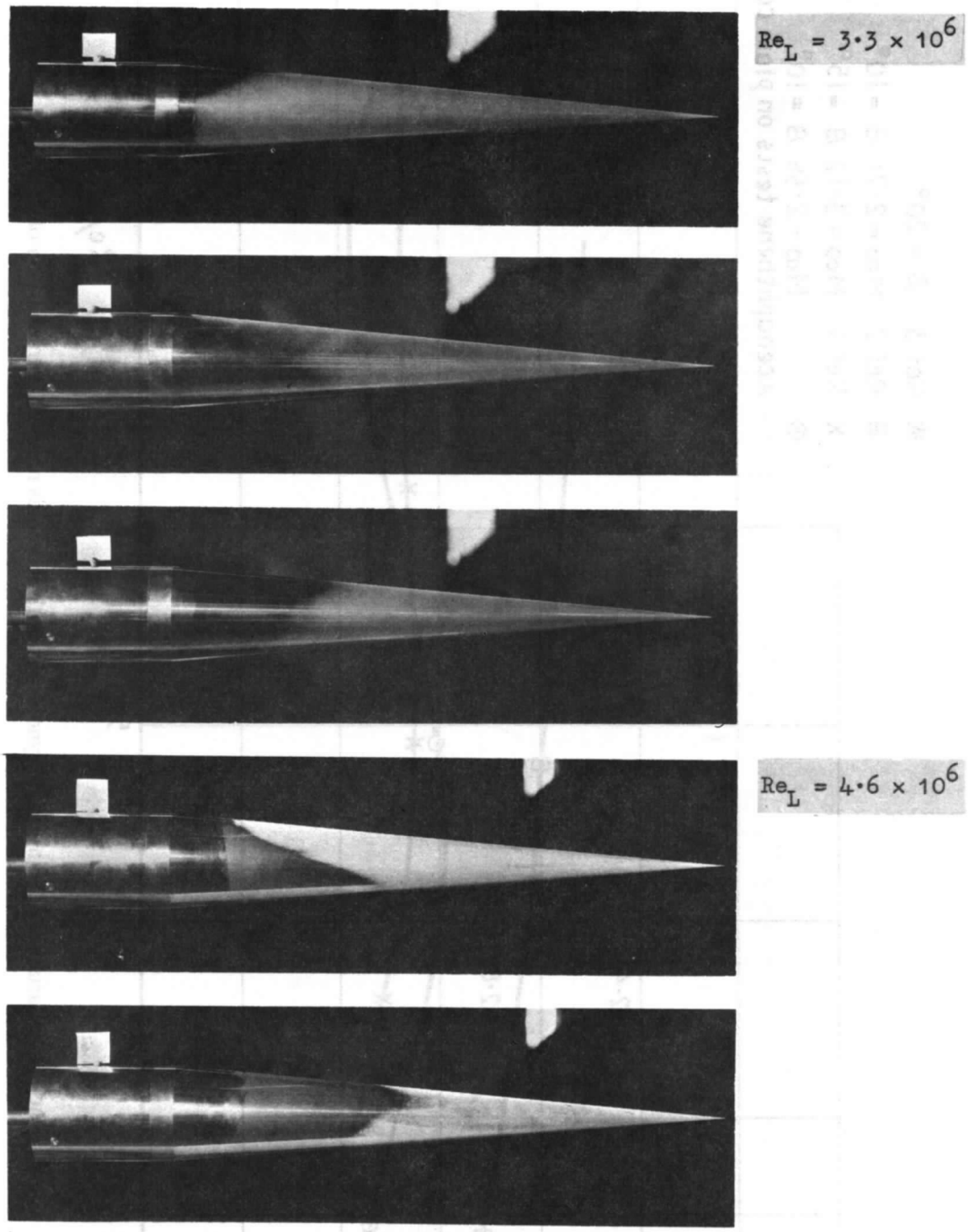

FIG. 12a. Plain cone: Transition position obtained using acenaphthene. ($Re_L = 3{\cdot}3$ and $4{\cdot}6 \times 10^6$).

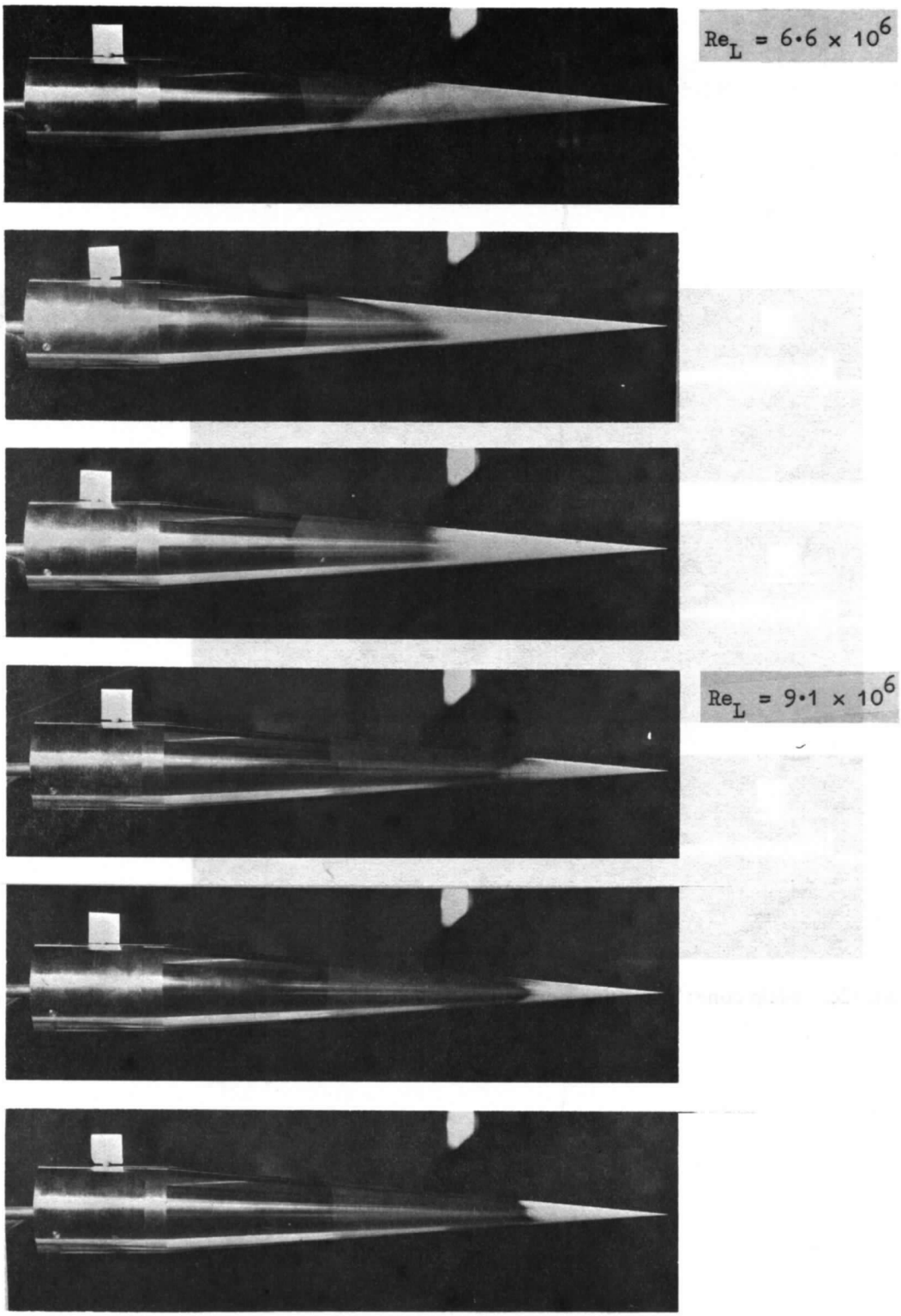

FIG. 12b. Plain cone: Transition position obtained using acenaphthene. ($Re_L = 6{\cdot}6$ and $9{\cdot}1 \times 10^6$).

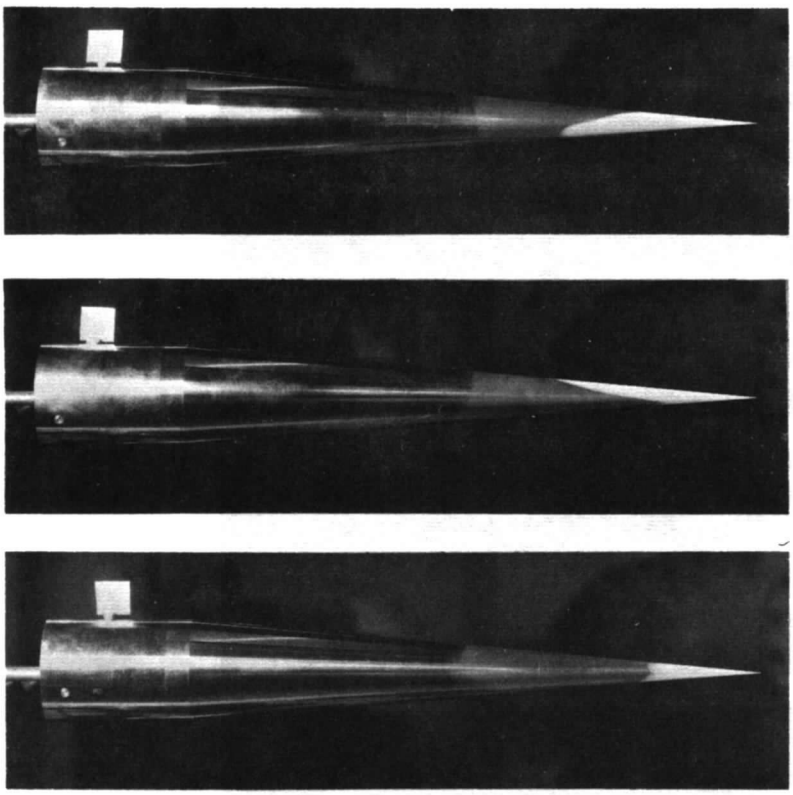

FIG. 12c. Plain cone: Transition position obtained using acenaphthene. ($Re_L = 11{\cdot}4 \times 10^6$).

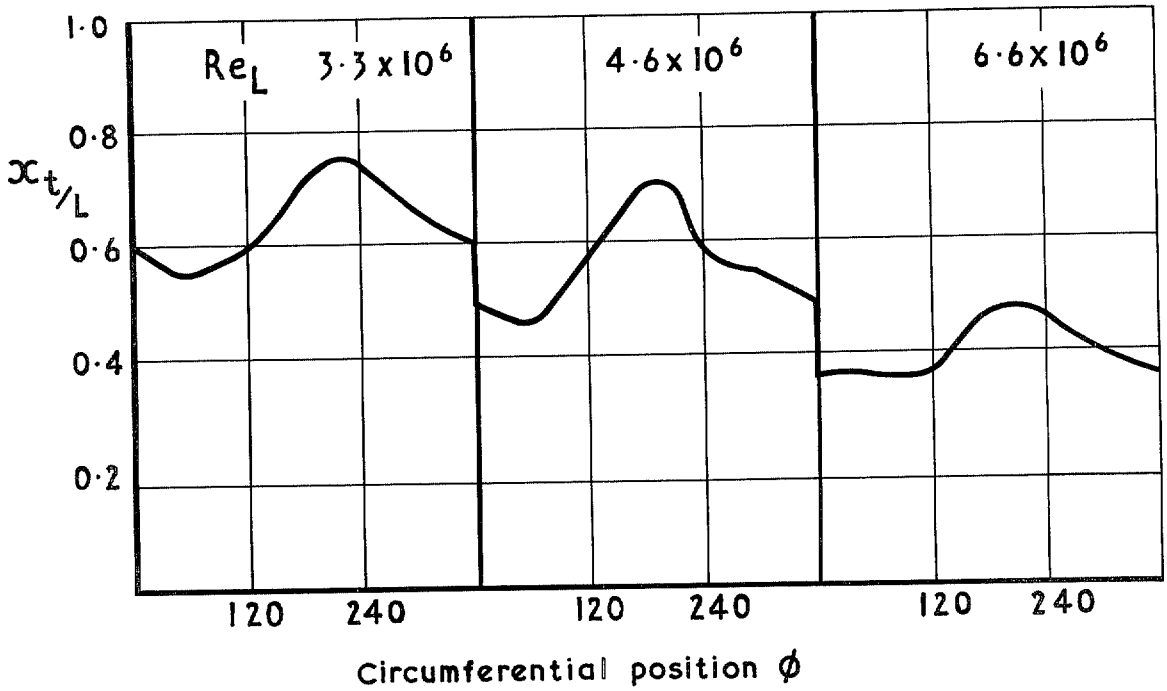

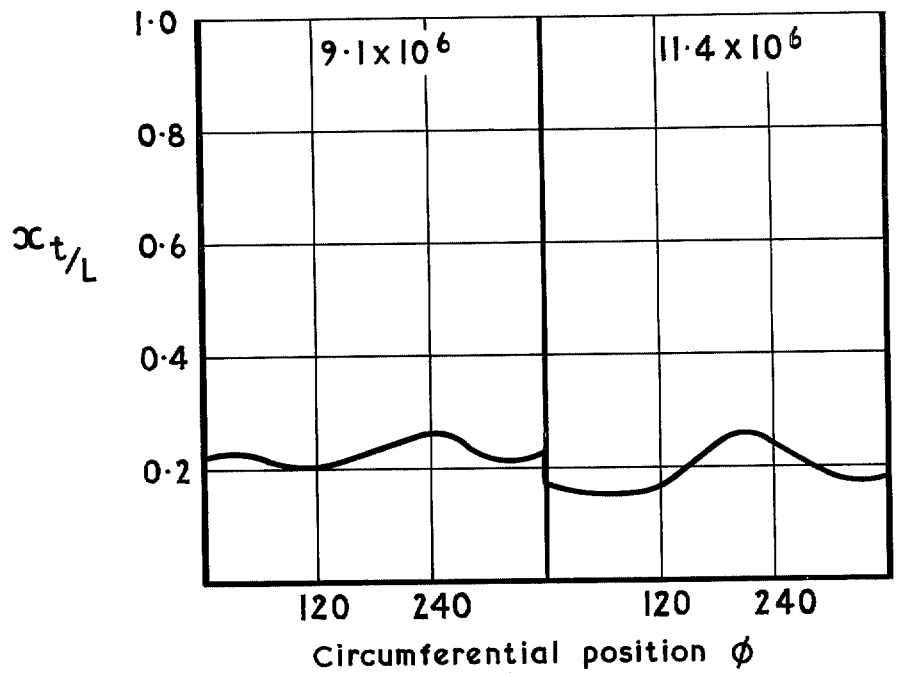

FIG. 13. Circumferential variation of transition front on the plain cone using acenaphthene indicator.

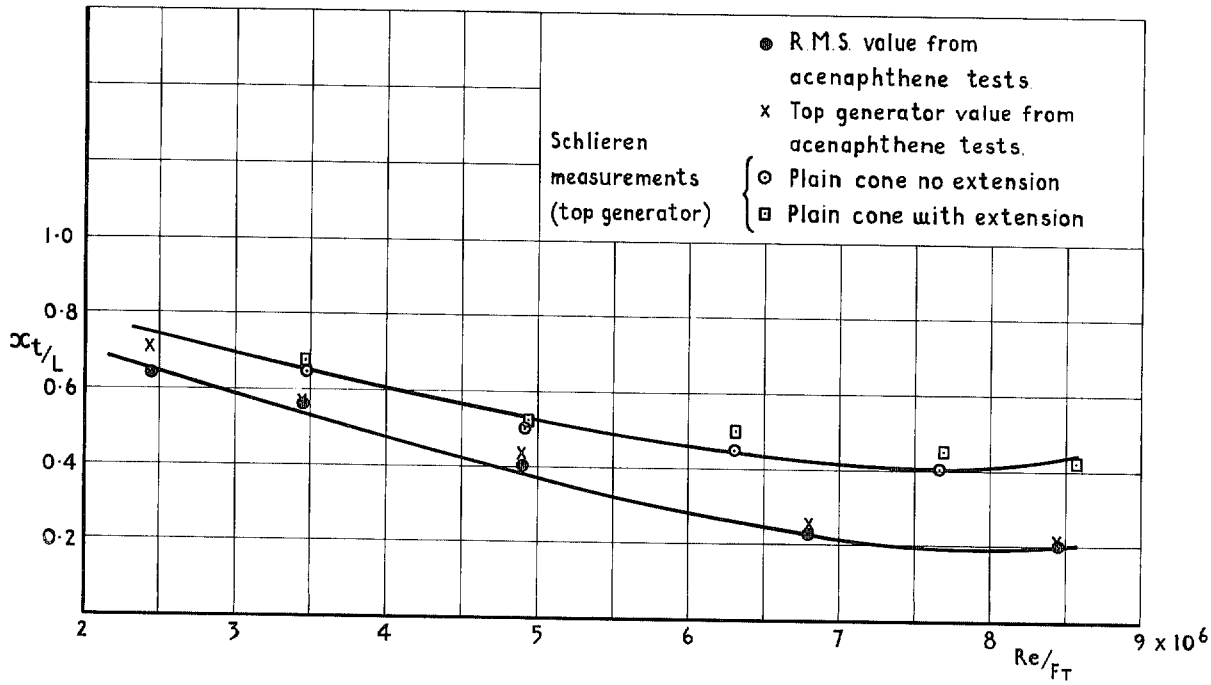

FIG. 14. Comparison of schlieren and acenaphthene determination of transition location.

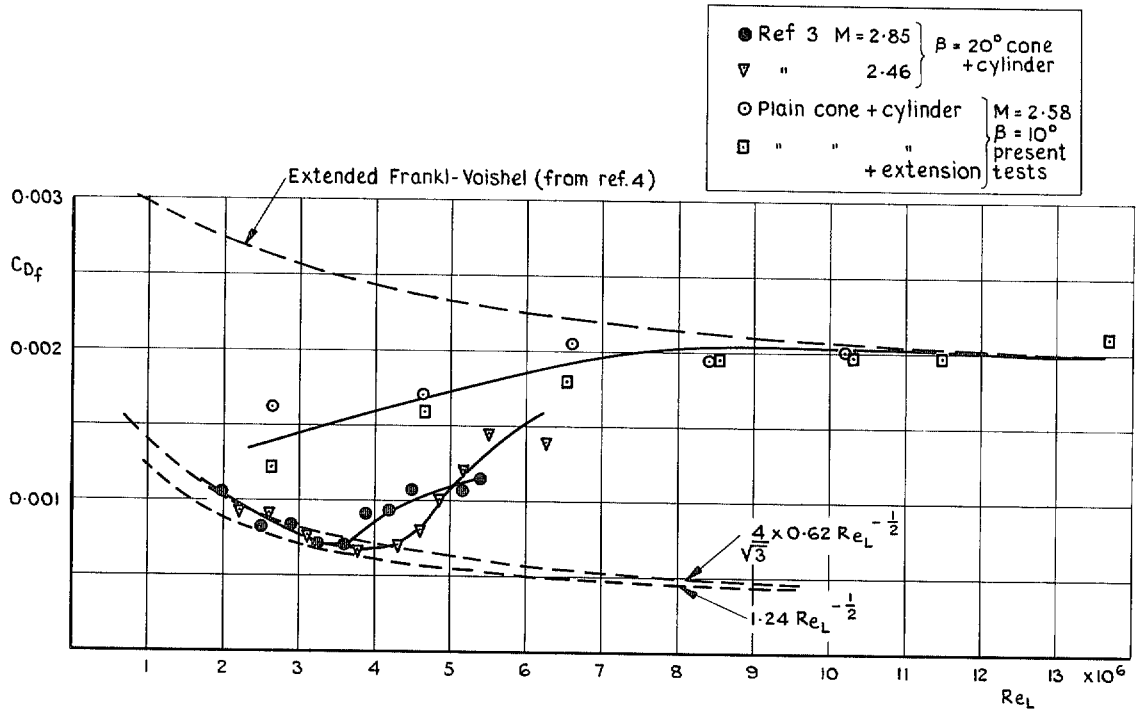

FIG. 15. Comparison of theoretical and measured skin-friction drag.

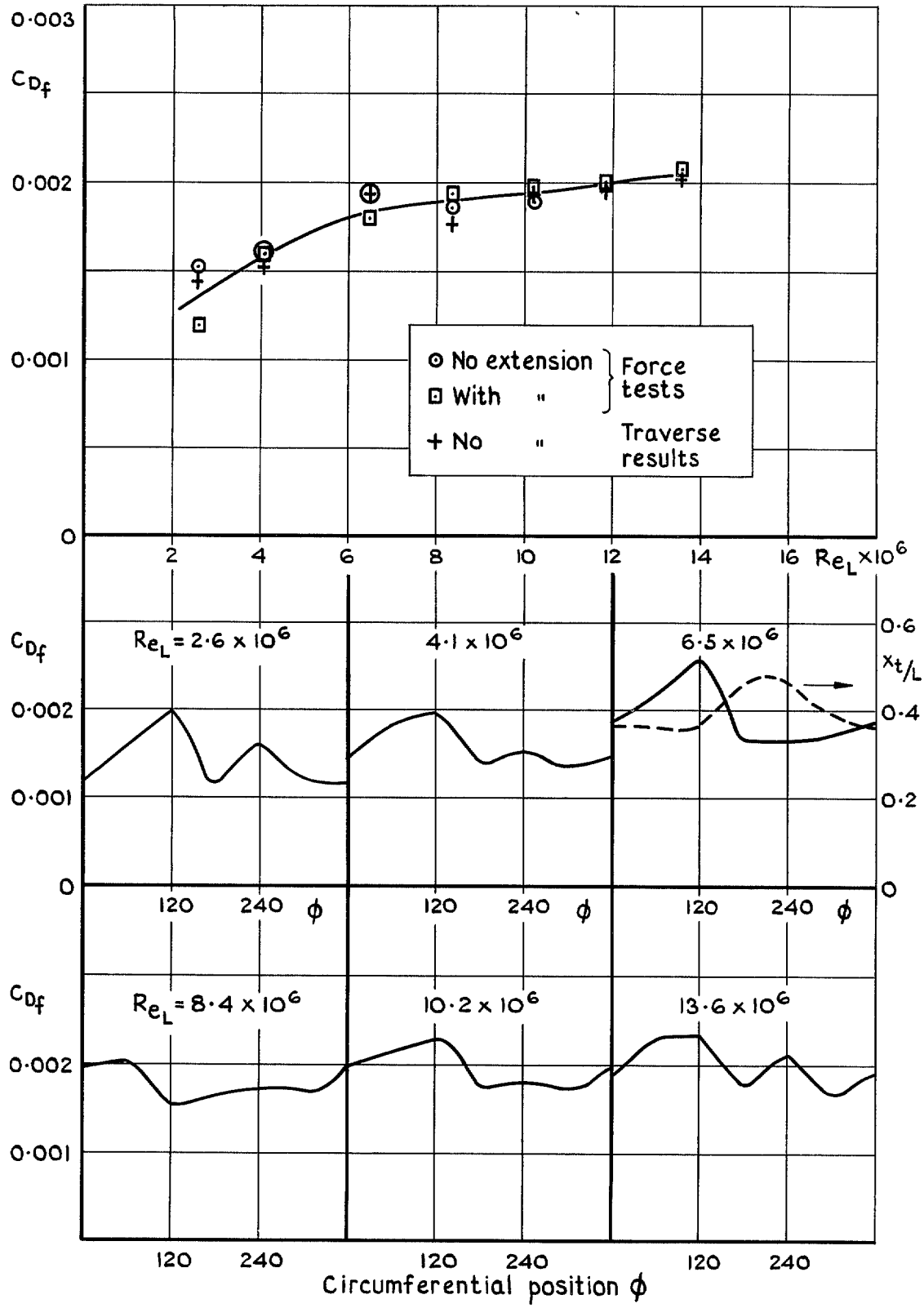

FIG. 16. Comparison of force and traverse results for plain cone and distribution of C_{D_f} around circumference.

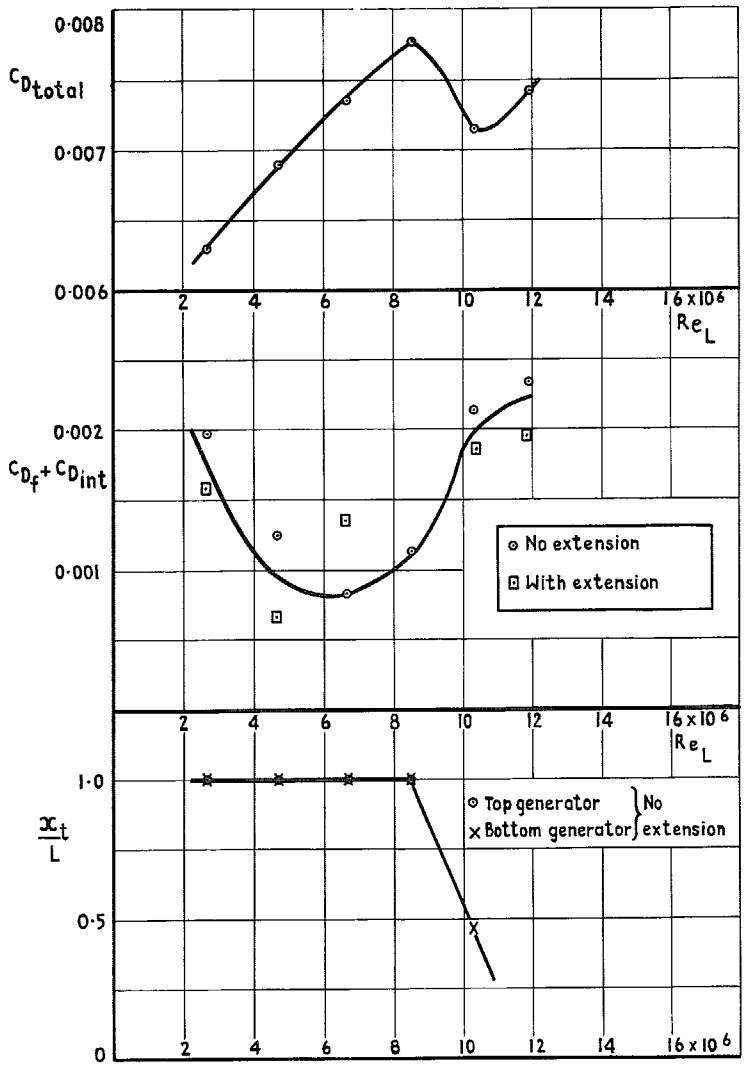

FIG. 17a. Variation of $C_{D_{\text{total}}}$, $C_{D_f} + C_{D_{\text{int}}}$ and $X_{t/L}$ with Reynolds no. ($\varepsilon = 0°$, Plug 1, $A_{ex}/A_{max} = 0{\cdot}0370$).

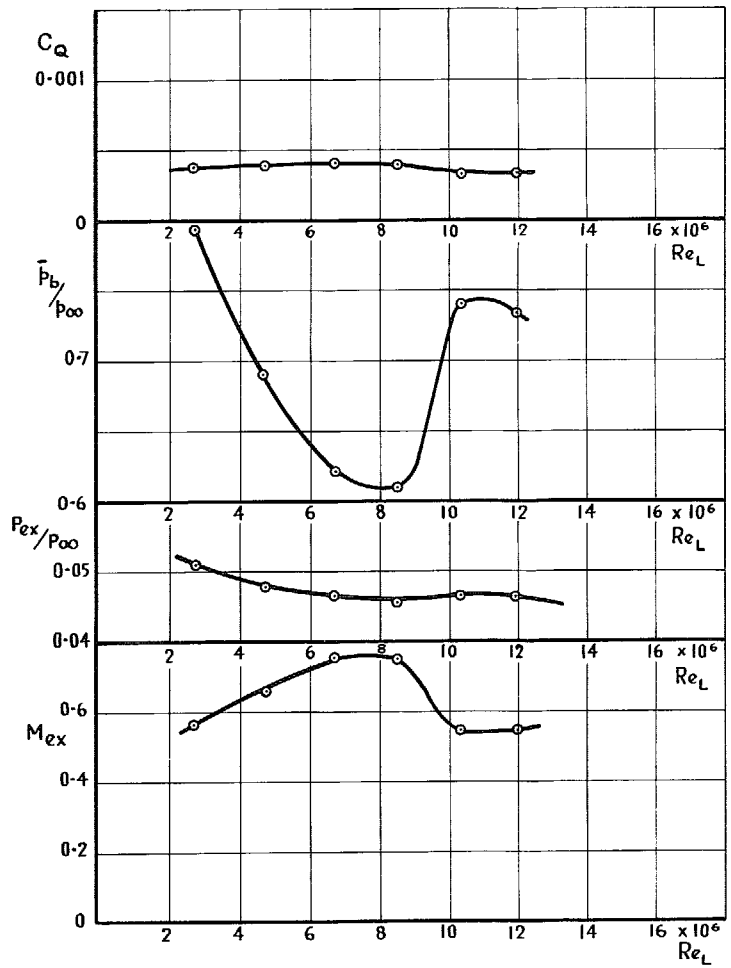

FIG. 17b. Variation of C_Q, p_b/p_∞, P_{ex}/p_∞ and M_{ex} with Reynolds no.
($\varepsilon = 0°$, Plug 1, $A_{ex}/A_{max} = 0{\cdot}037$.)

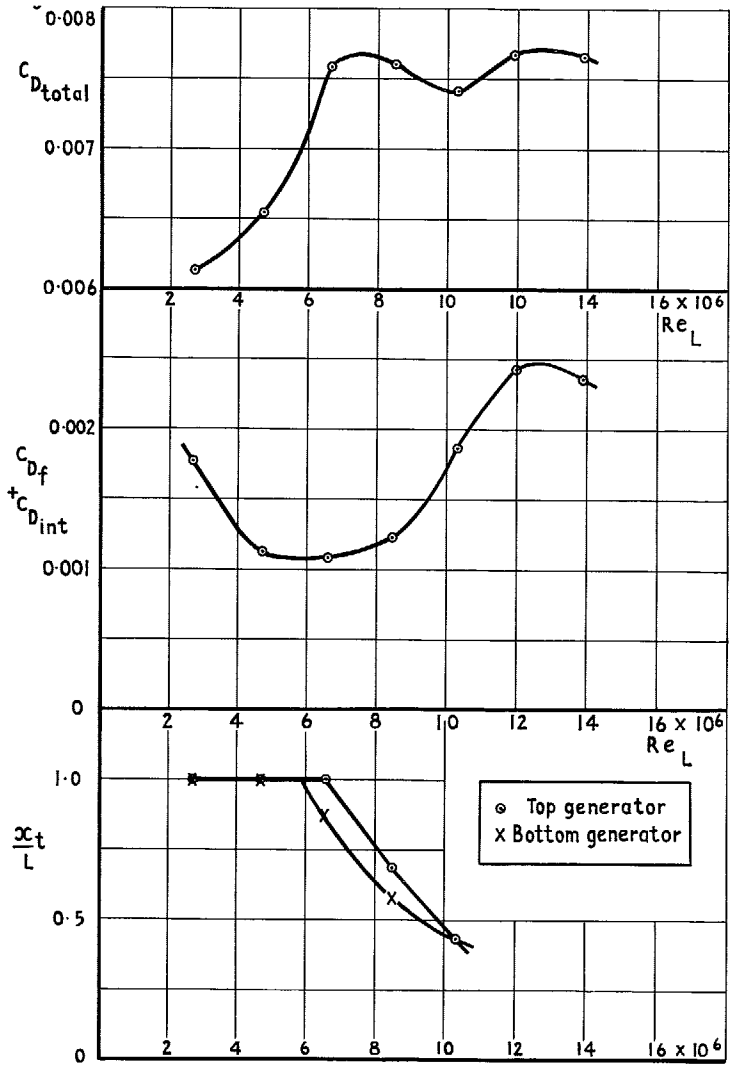

FIG. 18a. Variation of $C_{D_{total}}$, $C_{D_f} + C_{D_{int}}$ and $X_{t/L}$ with Reynolds no.
($\varepsilon = 0°$, Plug 1B, $A_{ex}/A_{max} = 0{\cdot}0863$.)

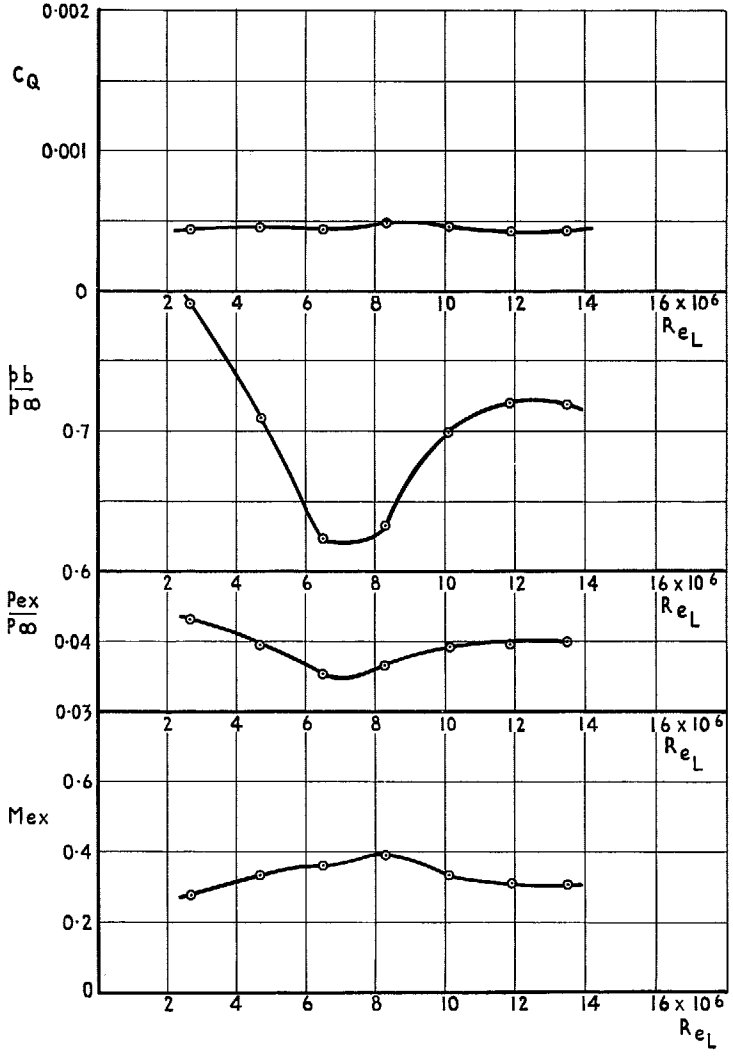

FIG. 18b.

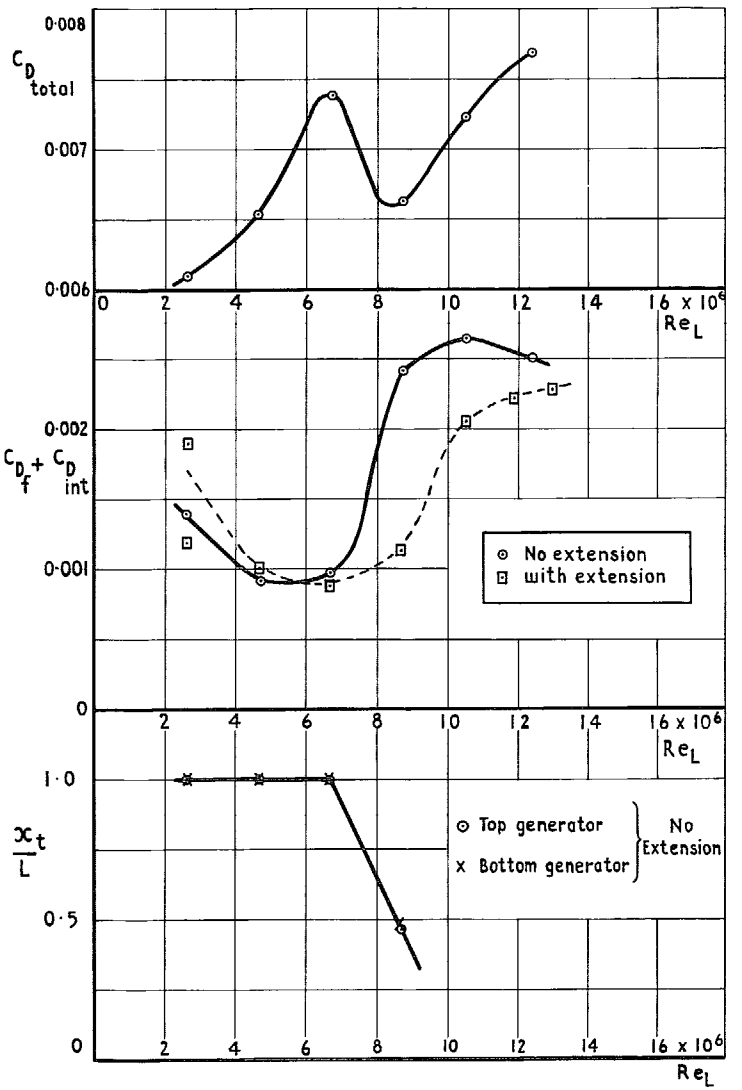

FIG. 19a. Variation of $C_{D_{\text{total}}}$, $C_{D_f} + C_{D_{\text{int}}}$ and $X_{t/L}$ with Reynolds no.
($\varepsilon = 0°$, Plug 2, $A_{ex}/A_{max} = 0{\cdot}115$.)

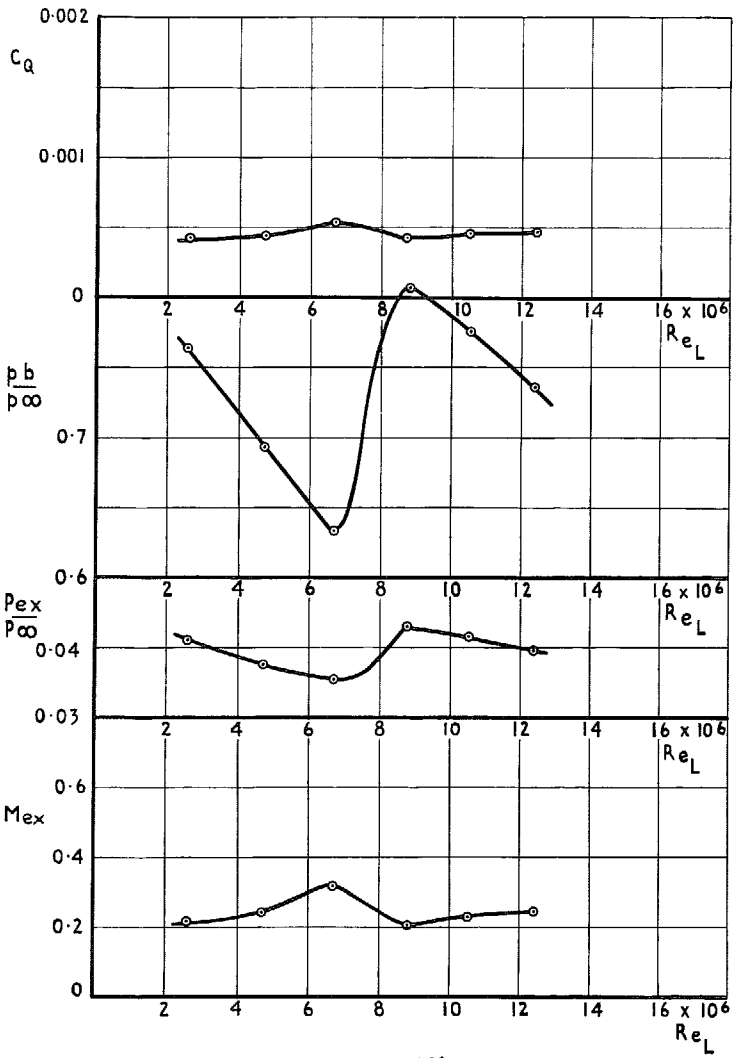

FIG. 19b.

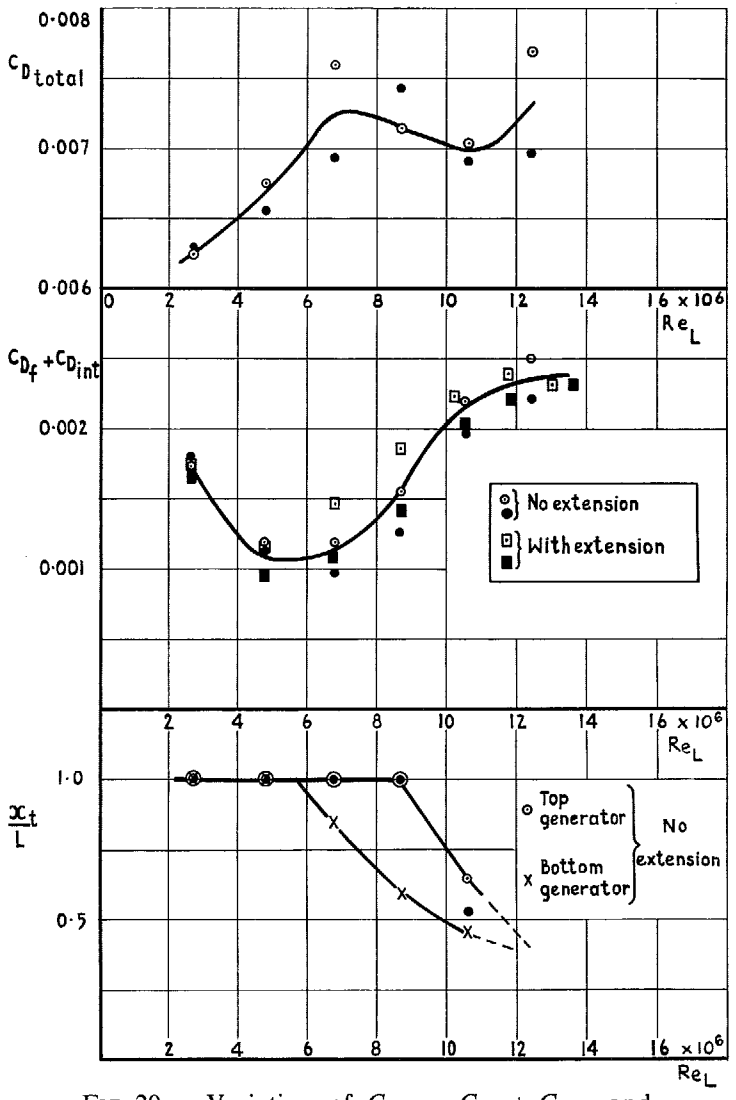

FIG. 20a. Variation of $C_{D_{\text{total}}}$, $C_{D_f} + C_{D_{\text{int}}}$ and $X_{t/L}$ with Reynolds no.
($\varepsilon = 0°$, Plug 4, $A_{ex}/A_{max} = 0{\cdot}292$.)

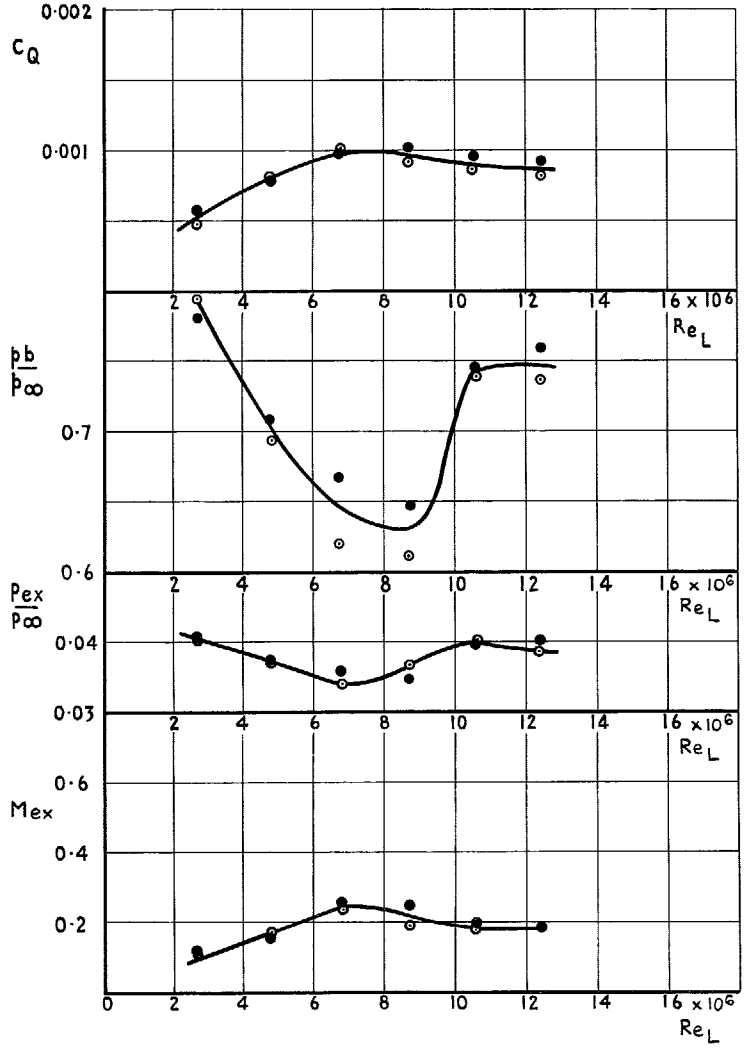

FIG. 20b.

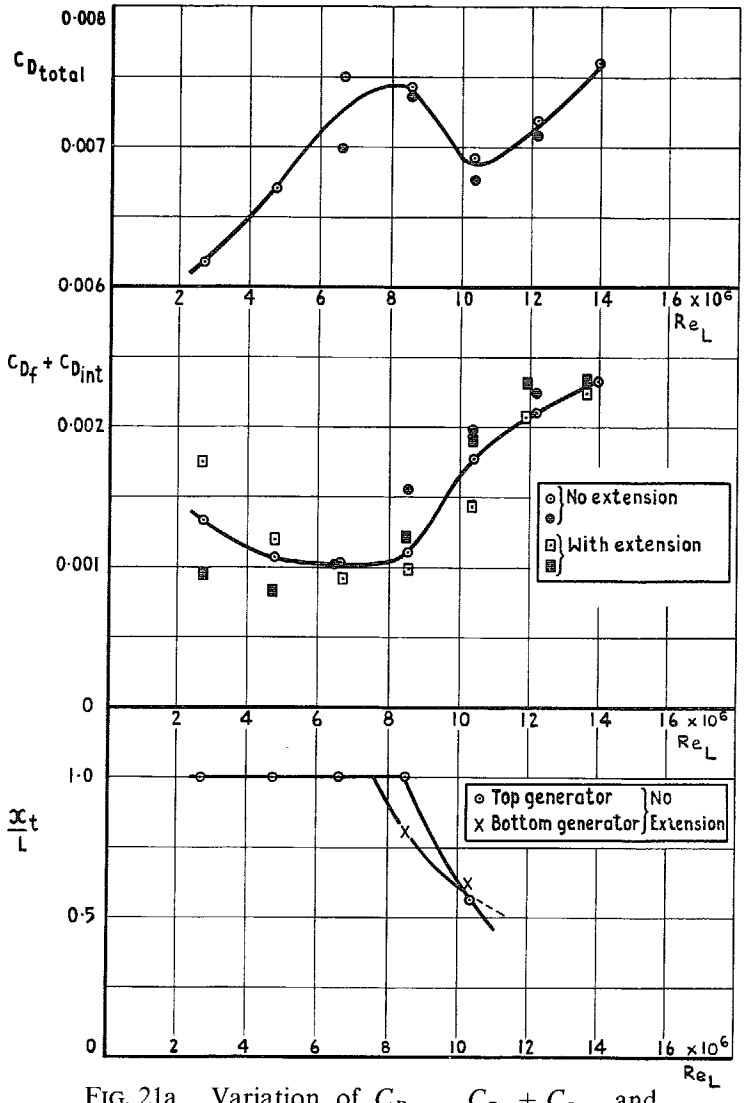

FIG. 21a. Variation of $C_{D_{\text{total}}}$, $C_{D_f} + C_{D_{\text{int}}}$ and $X_{t/L}$ with Reynolds no.
($\varepsilon = 0°$, Plug 6, $A_{ex}/A_{max} = 0{\cdot}494$.)

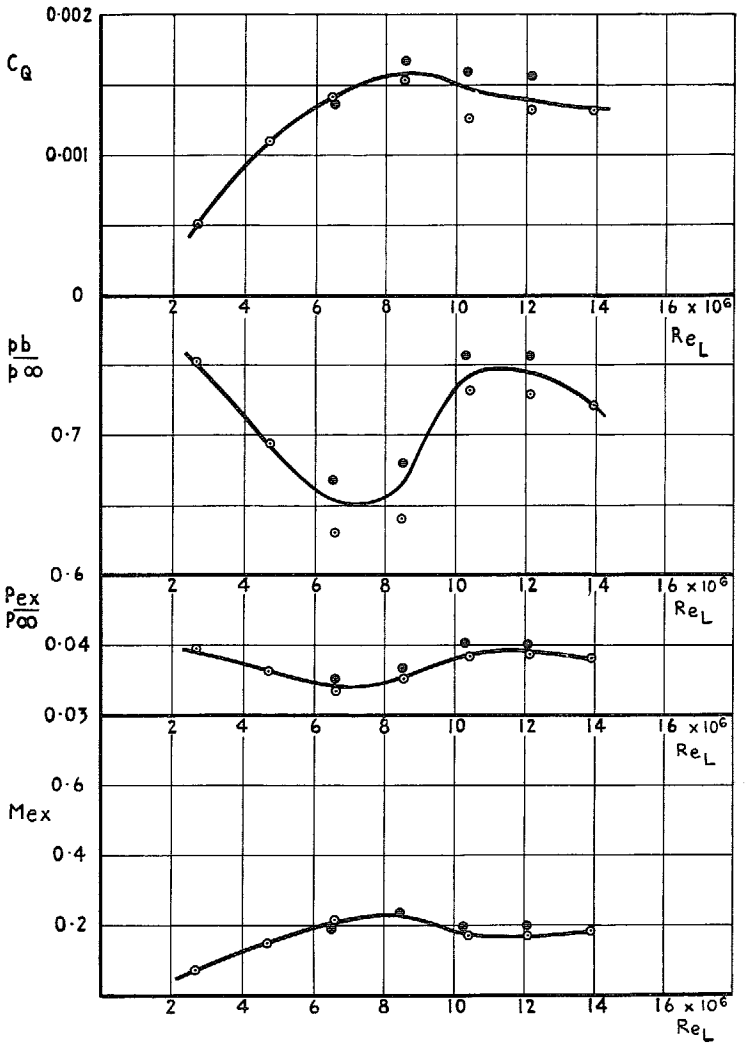

FIG. 21b.

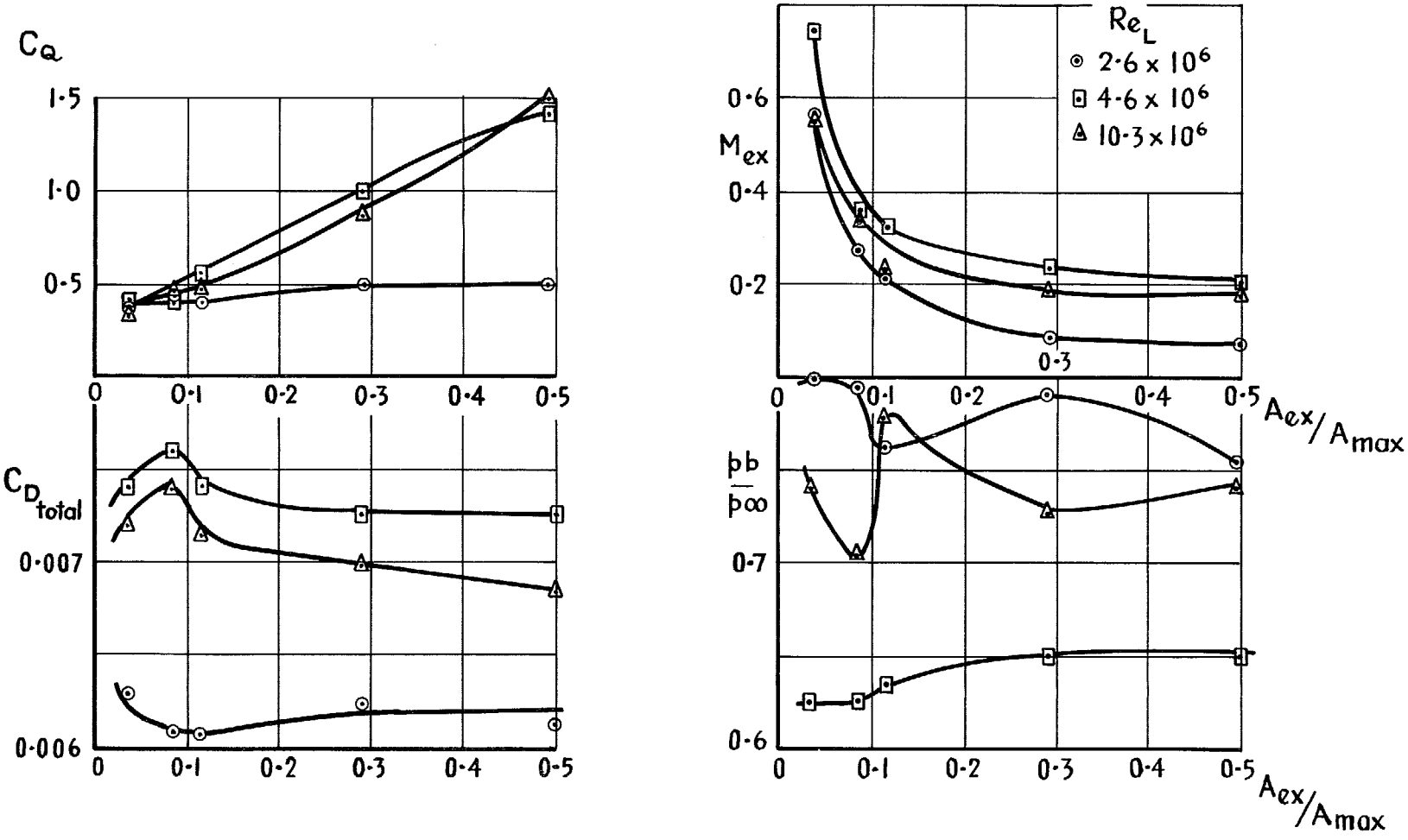

FIG. 22. Variation of C_Q, M_{ex}, $C_{D_{total}}$ and p_b/p_∞ with plug exit area.

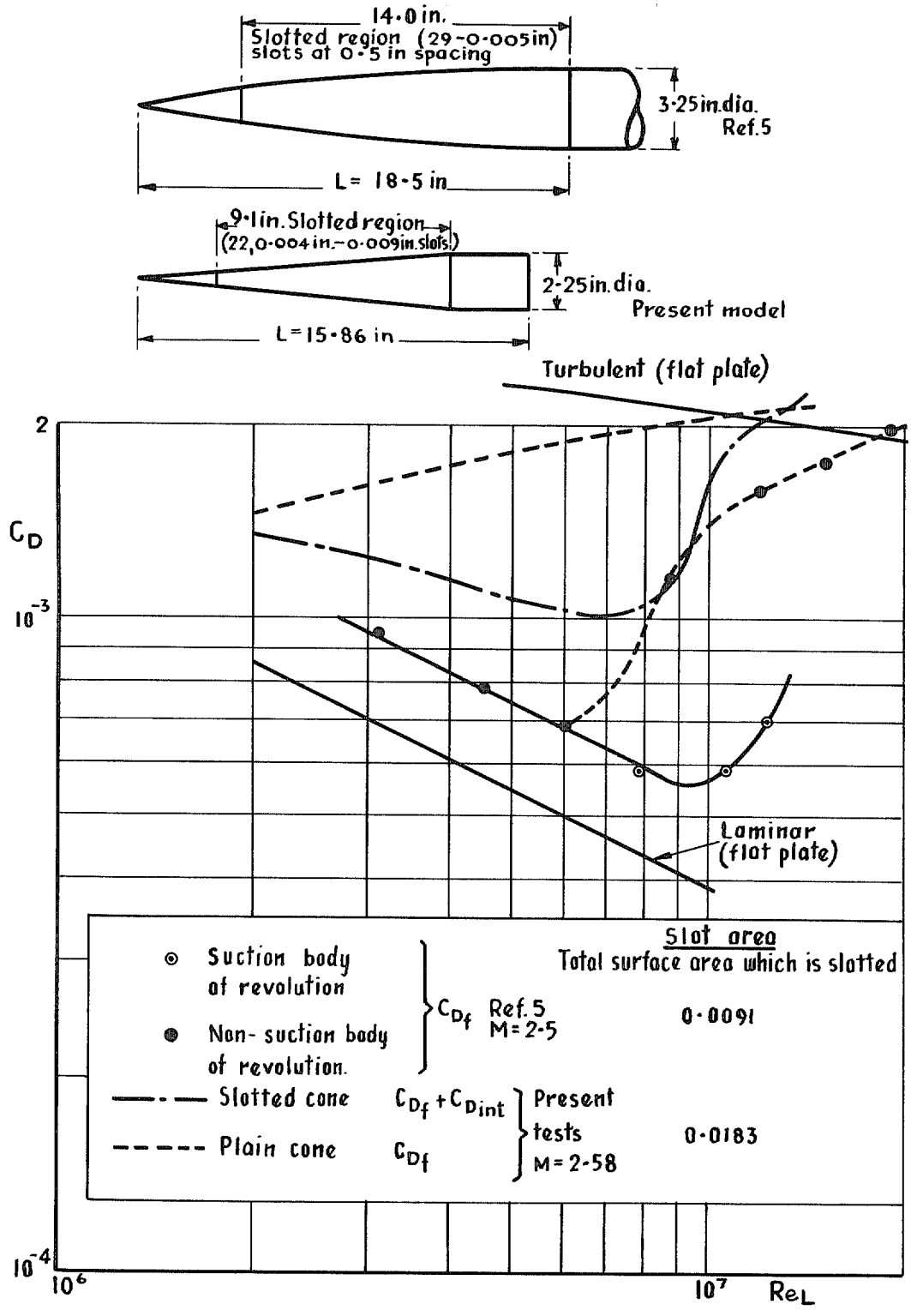

FIG. 23. Effect of laminarisation: comparison between early A.E.D.C. and present RAE tests at $M \simeq 2{\cdot}5$.

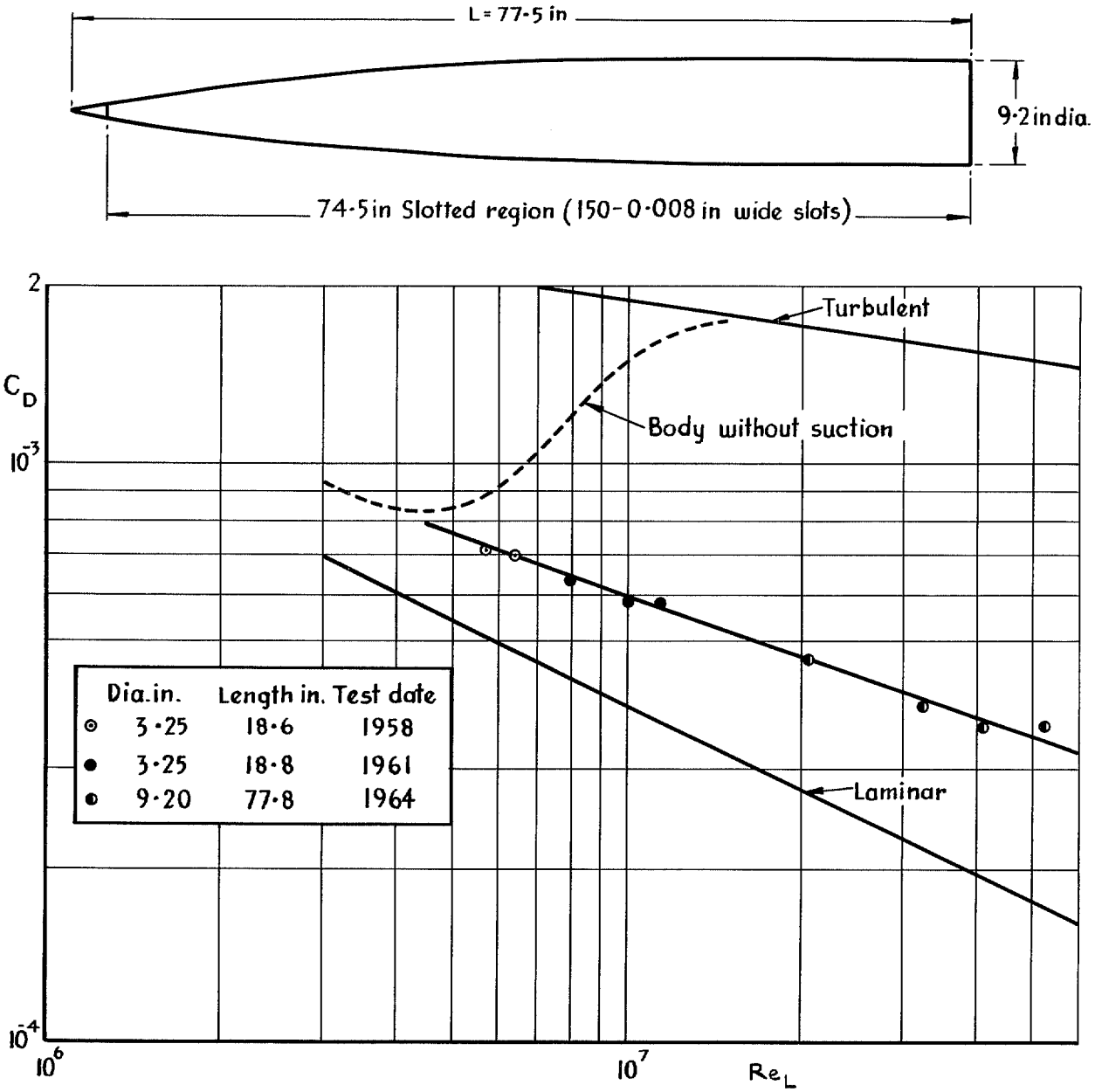

FIG. 24. Effect of laminarisation : extension of Reynolds no. range in later AEDC tests at M = 3·0 (Ref. 6).

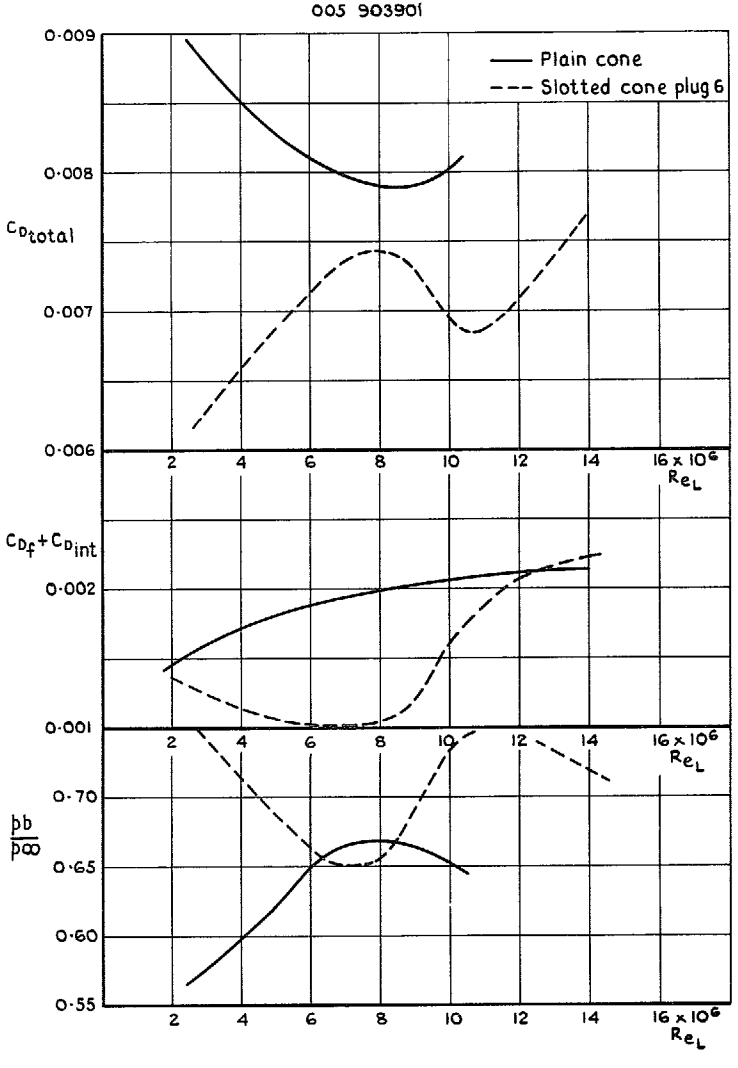

FIG. 25. Comparison between plain cone and vented slotted cone of $C_{D_{\text{total}}}$, $C_{D_f} + C_{D_{\text{int}}}$ and p_b/p_∞ against Re_L.

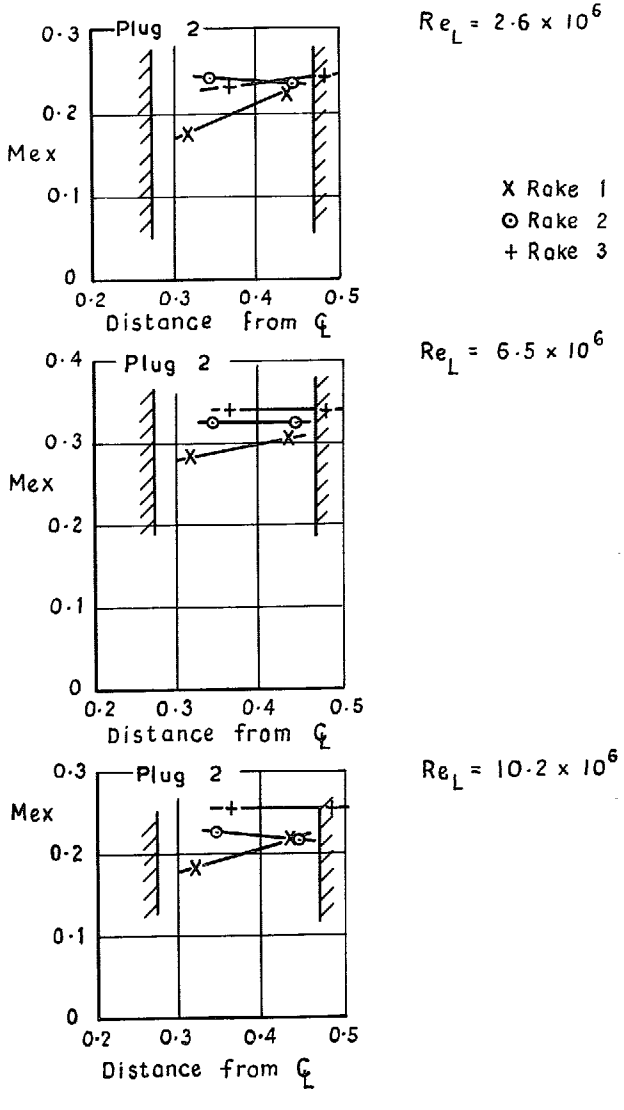

FIG. 26a. Distribution of exit Mach no. (Plug 2).

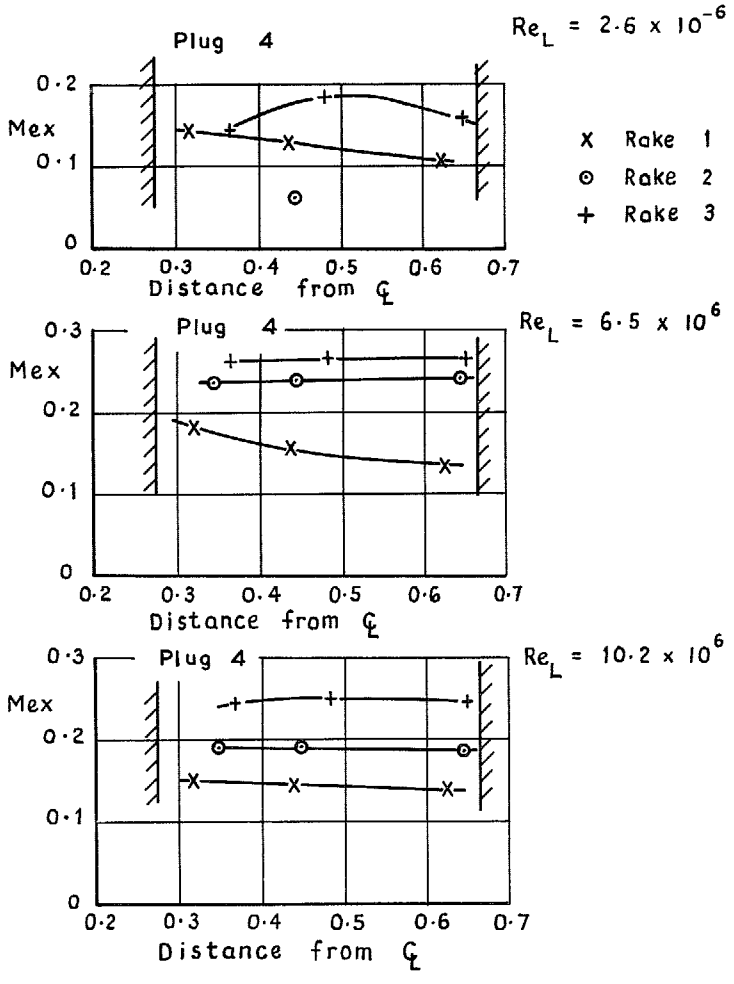

FIG. 26b. Distribution of exit Mach no. (Plug 4).

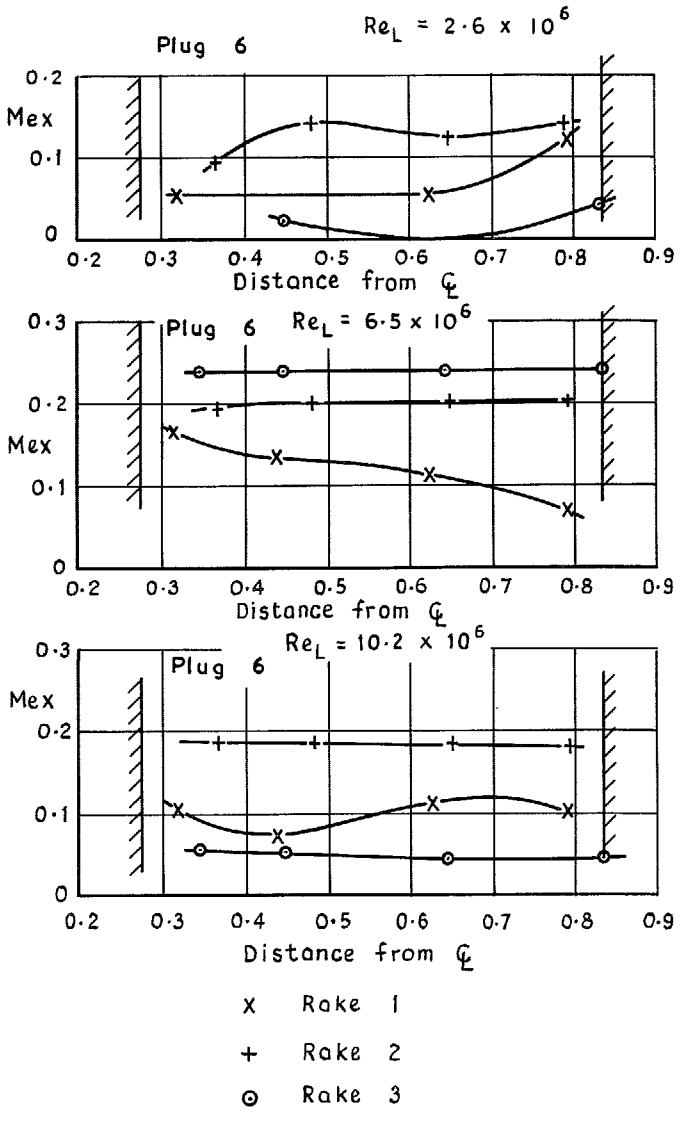

FIG. 26c. Distribution of exit Mach no. (Plug 6).

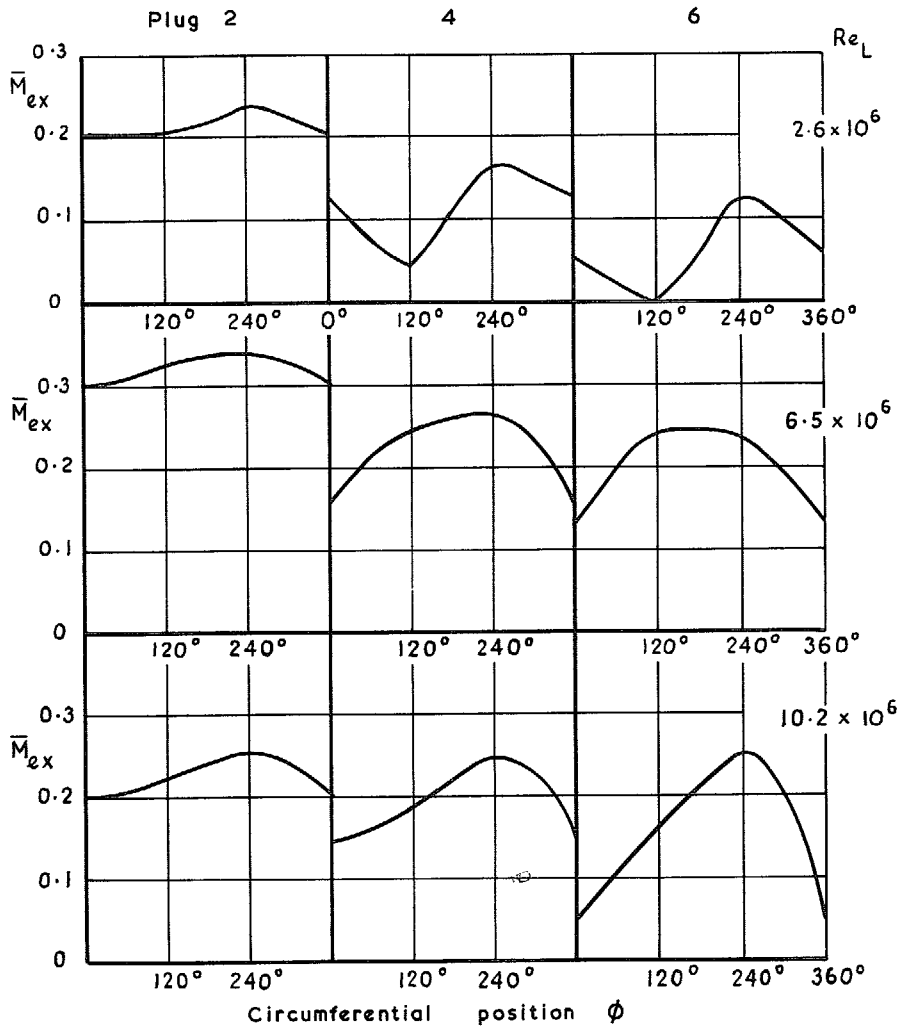

FIG. 27. Circumferential distribution of exit Mach no. (Plugs 2, 4 and 6).

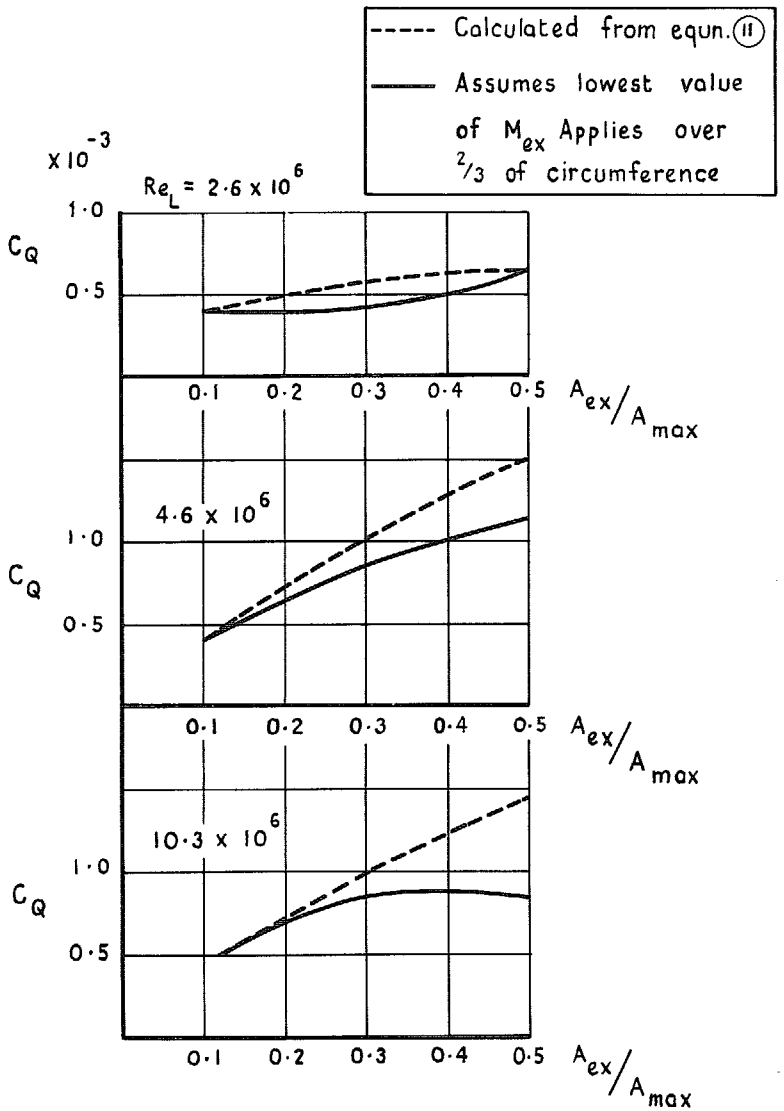

FIG. 28. Dependence of C_Q on calculation assumptions.

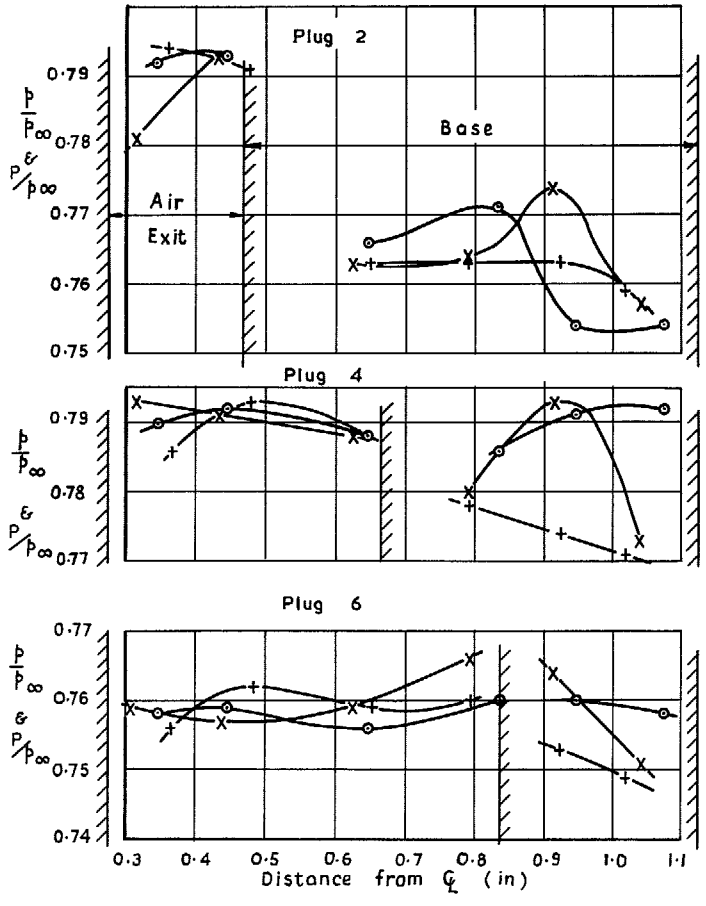

FIG. 29a. Distribution of exit total pressure and base static pressure at $Re_L = 2{\cdot}6 \times 10^6$.

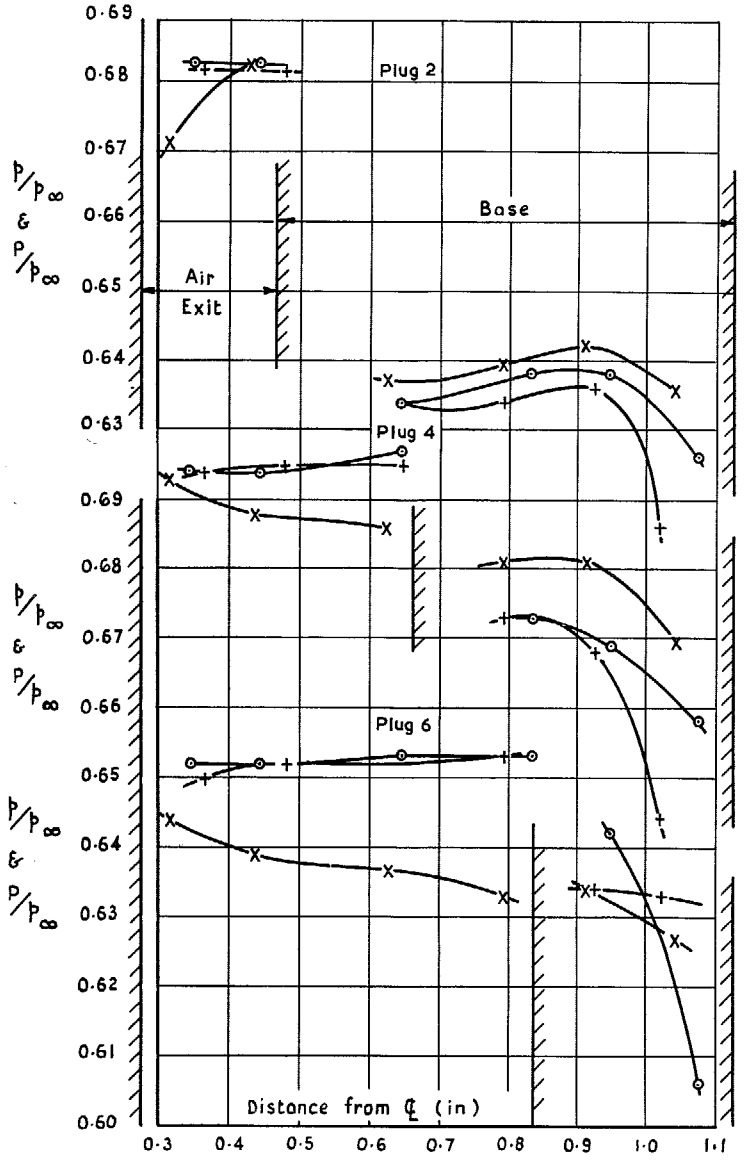

FIG. 29b. Distribution of exit total pressure and base static pressure at $Re_L = 6{\cdot}5 \times 10^6$.

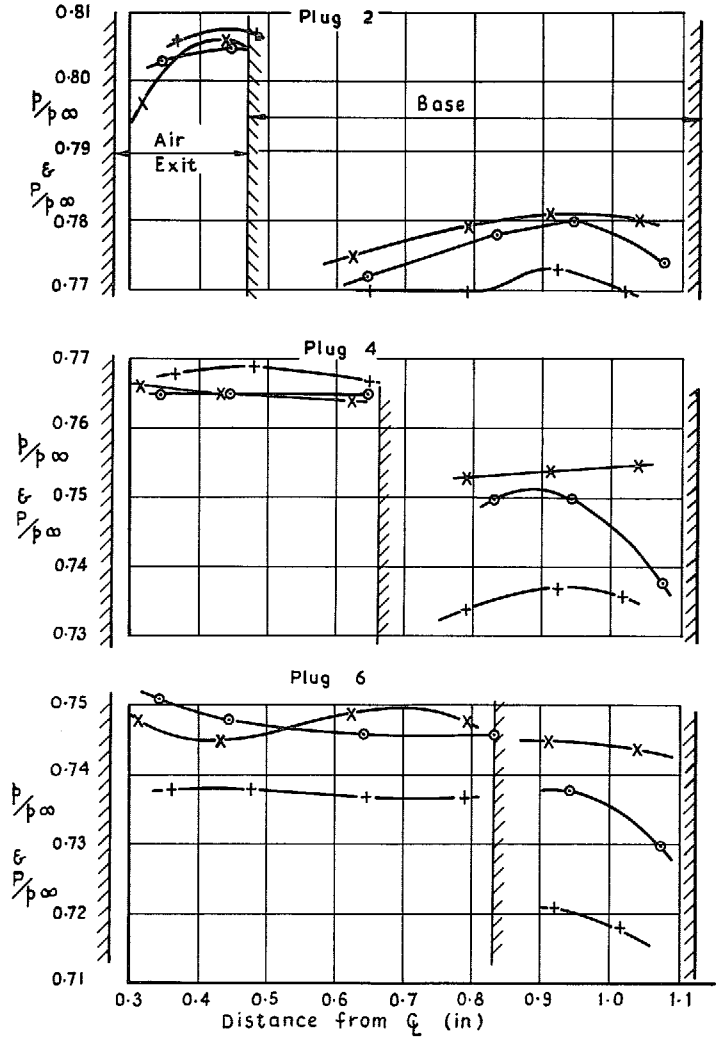

FIG. 29c. Distribution of exit total pressure and base static pressure at $Re_L = 10{\cdot}2 \times 10^{-6}$.

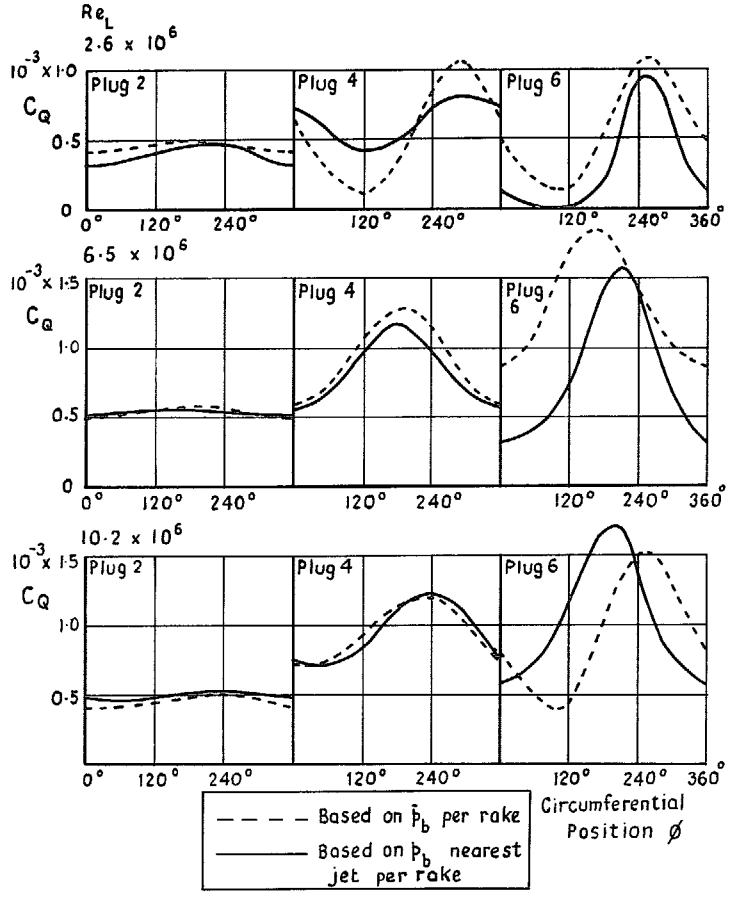

FIG. 30. Circumferential distribution of C_Q based on $\bar{p}_b$ per rake and on p_b nearest jet per rake.

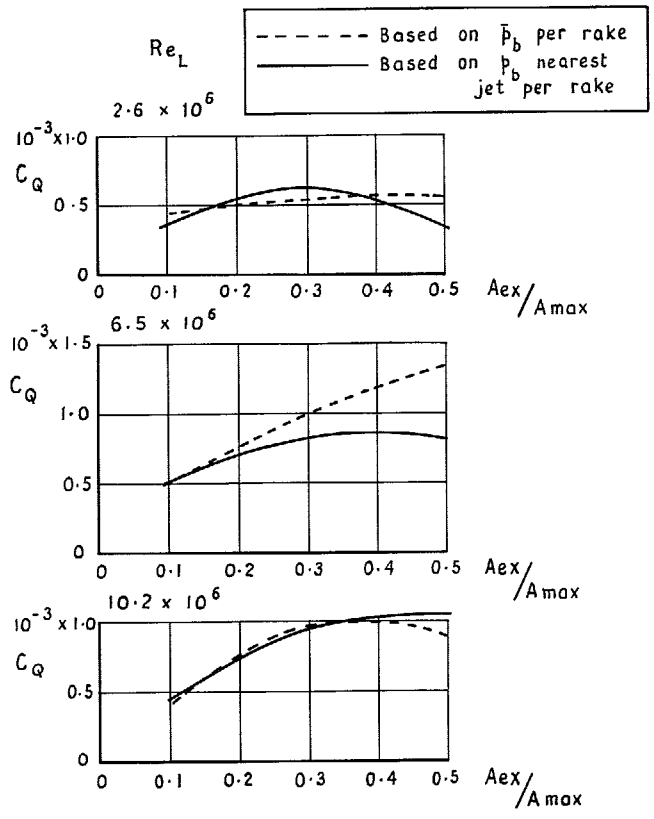

FIG. 31. Variation of mean C_Q with exit area.

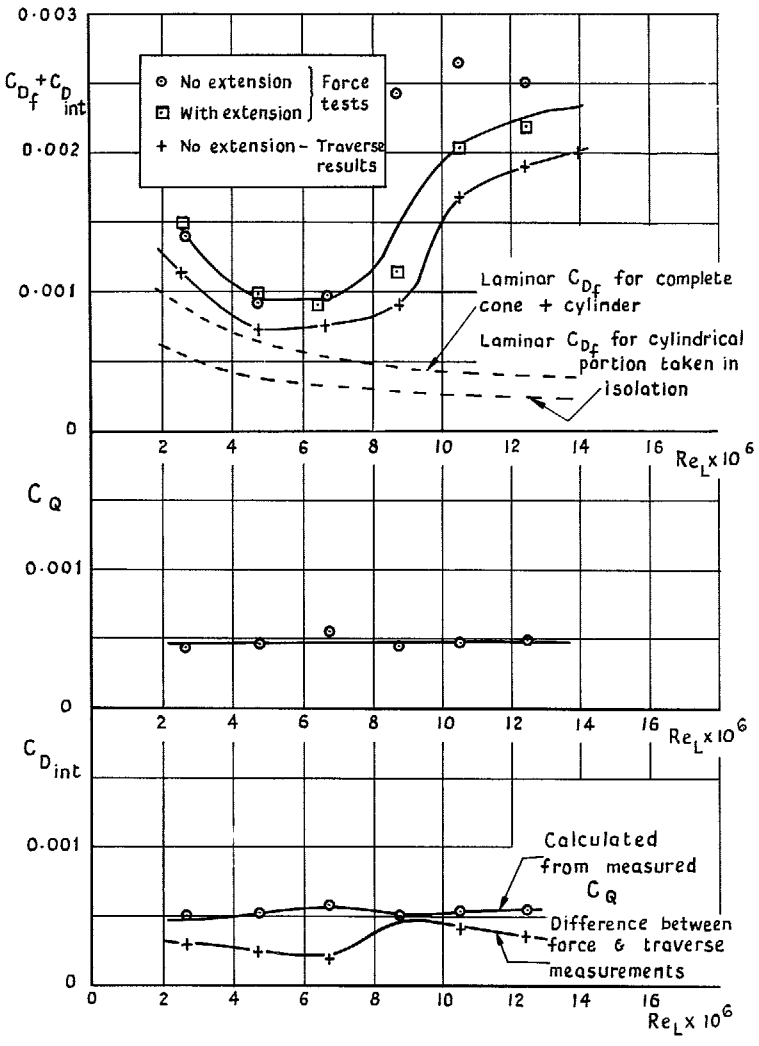

FIG. 32a. Comparison of force and traverse results (Plug 2).

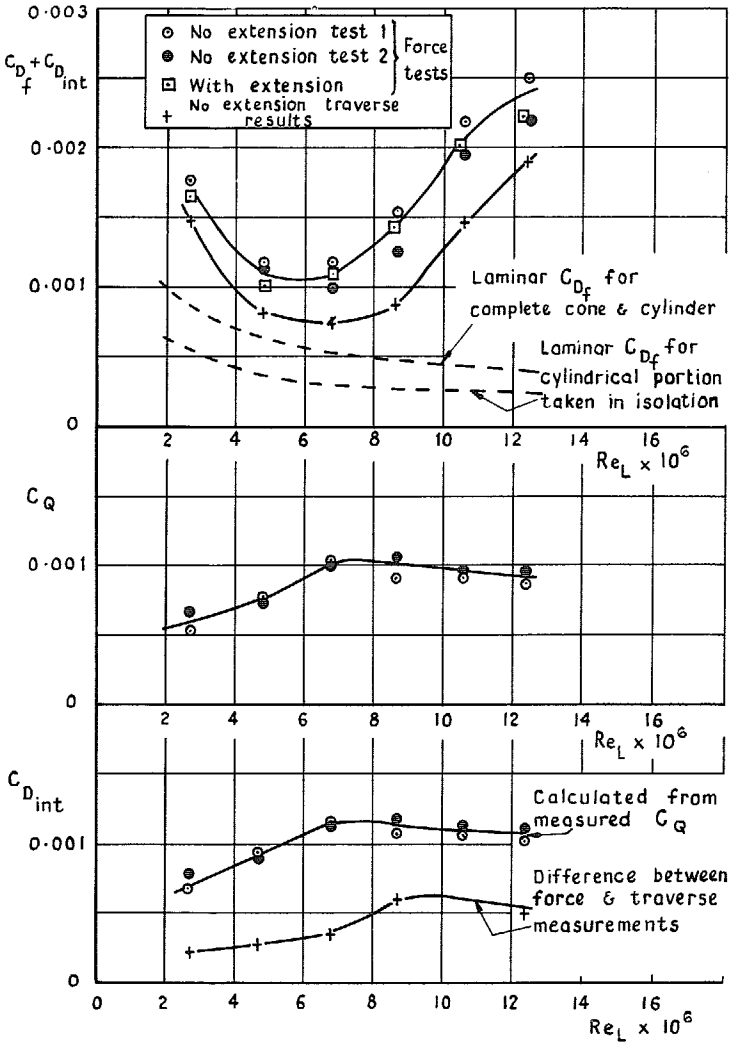

FIG. 32b. Comparison of force and traverse results (Plug 4).

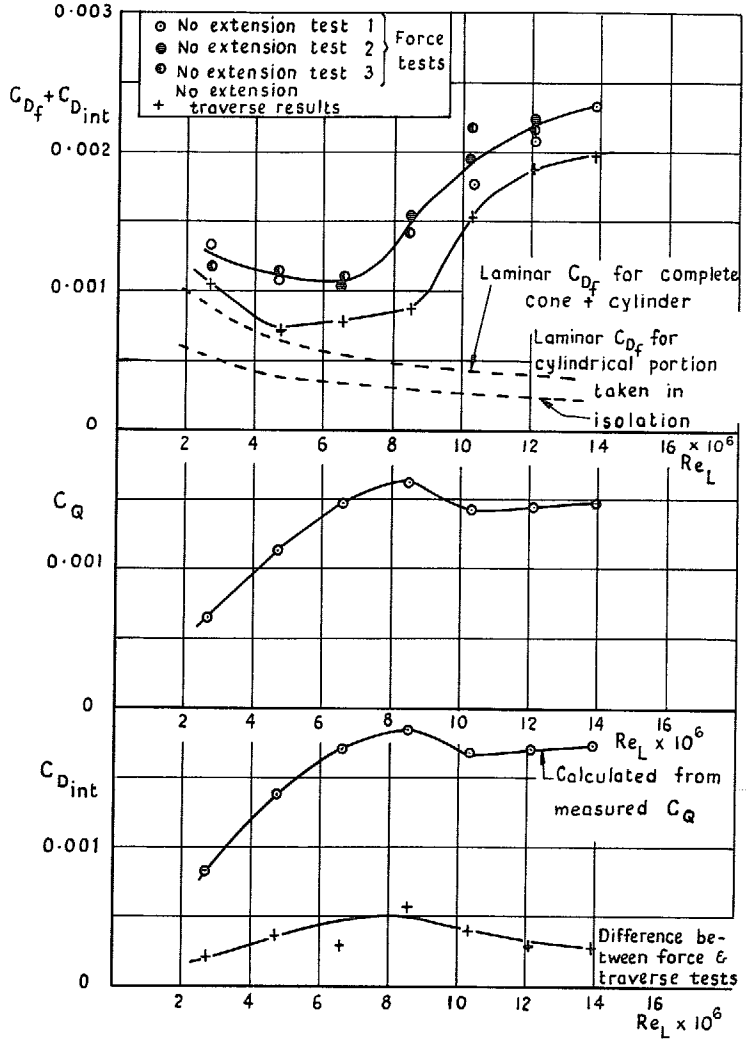

FIG. 32c. Comparison of force and traverse results (Plug 6).

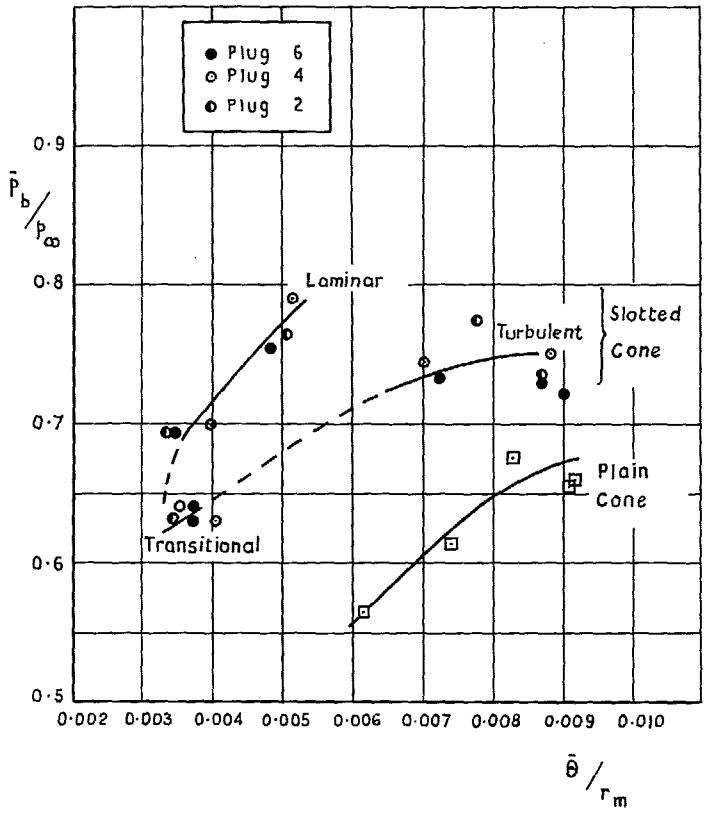

FIG. 33. Correlation of base pressure with boundary-layer momentum thickness.

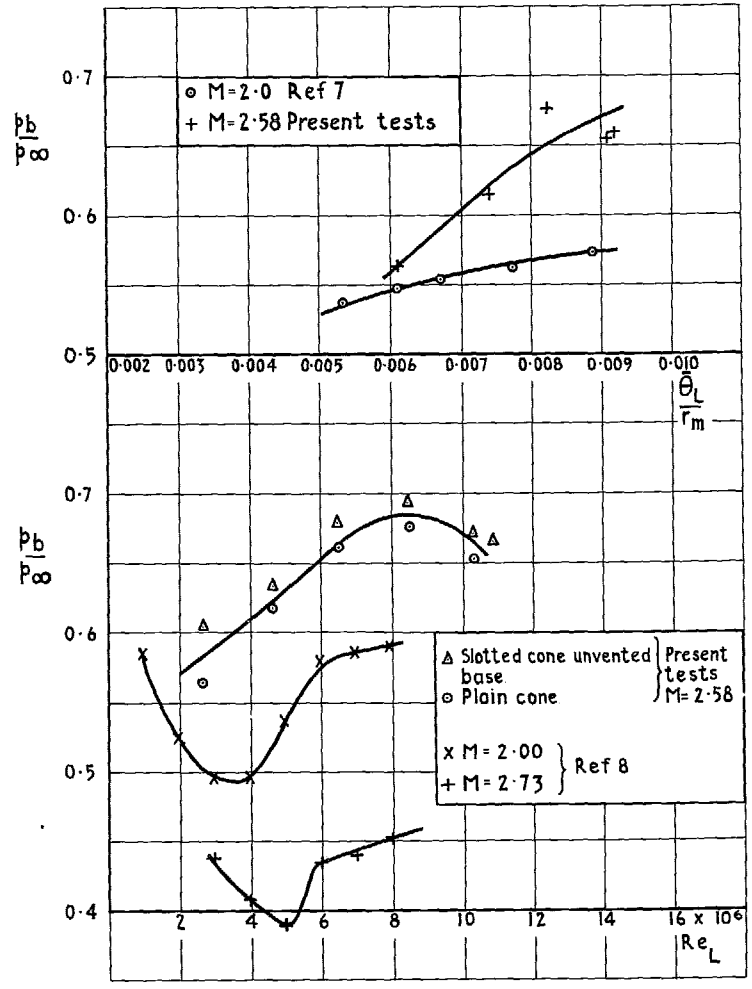

FIG. 34. Variation of base pressure with momentum thickness and with Reynolds no.: comparison of data.

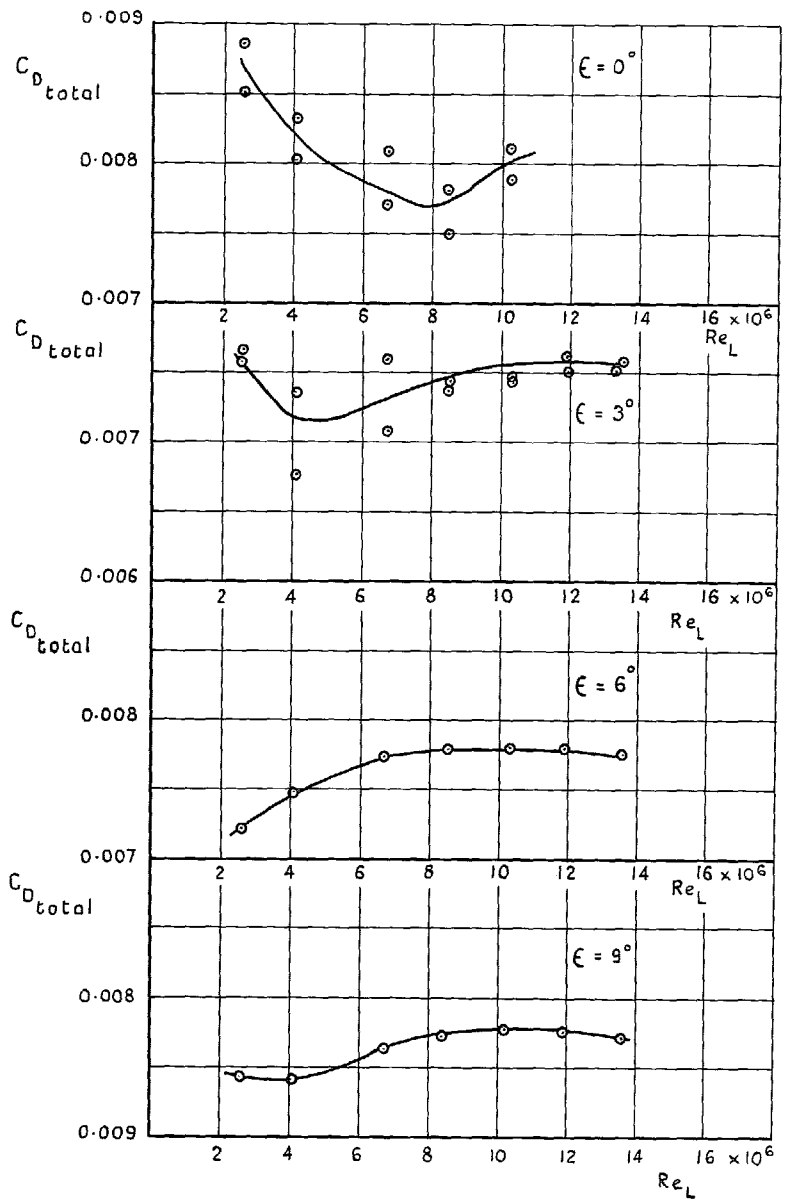

FIG. 35. Variation of $C_{D_{total}}$ with Reynolds no. for boattail angles of 0°, 3°, 6° and 9°.

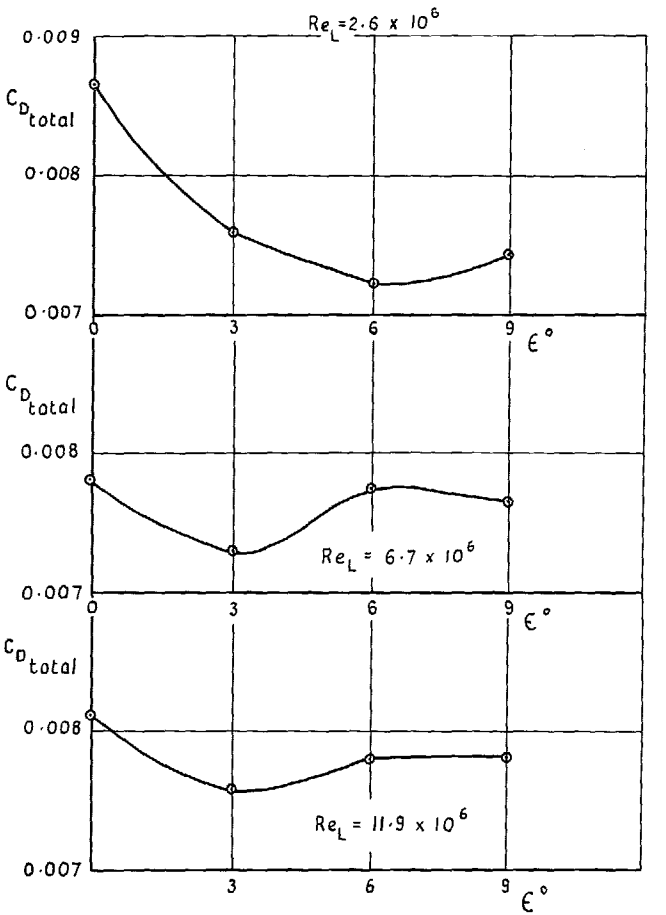

FIG. 36. Variation of total drag with boattail angle.

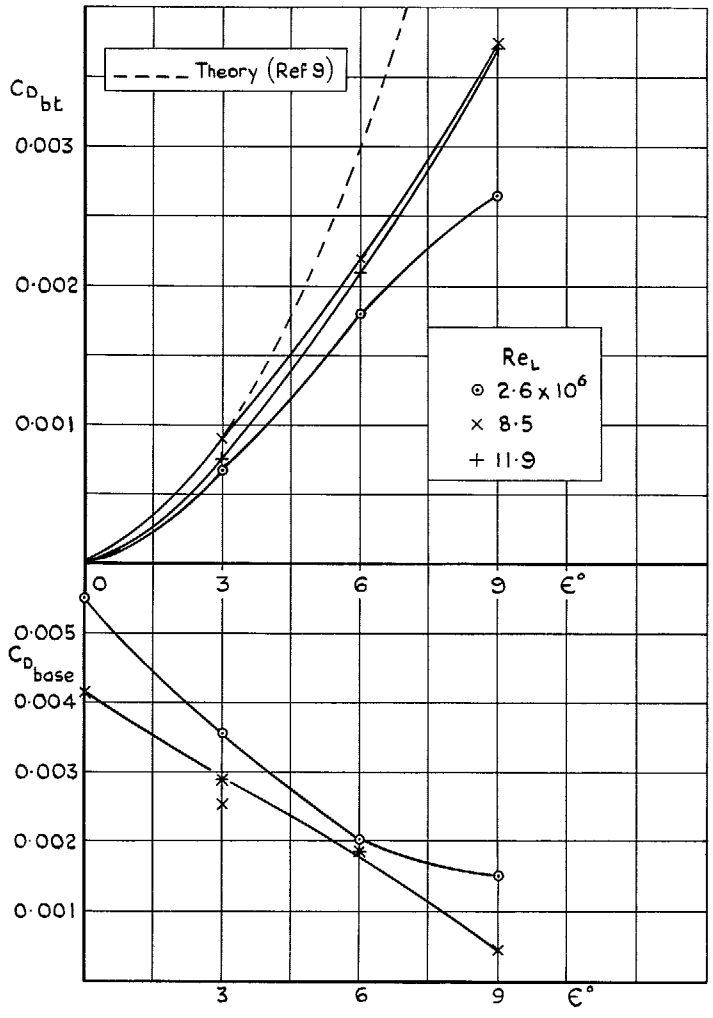

FIG. 37. Variation of base and boattail drag with boattail angle.

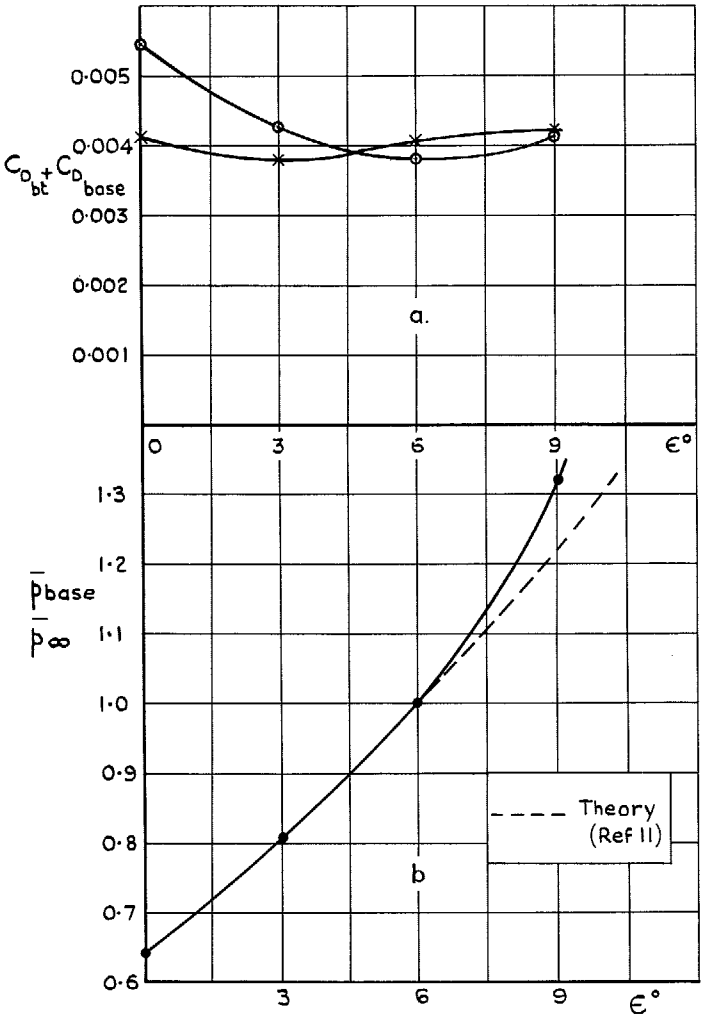

FIG. 38. Variation of base plus boattail drag and of base pressure with boattail angle.

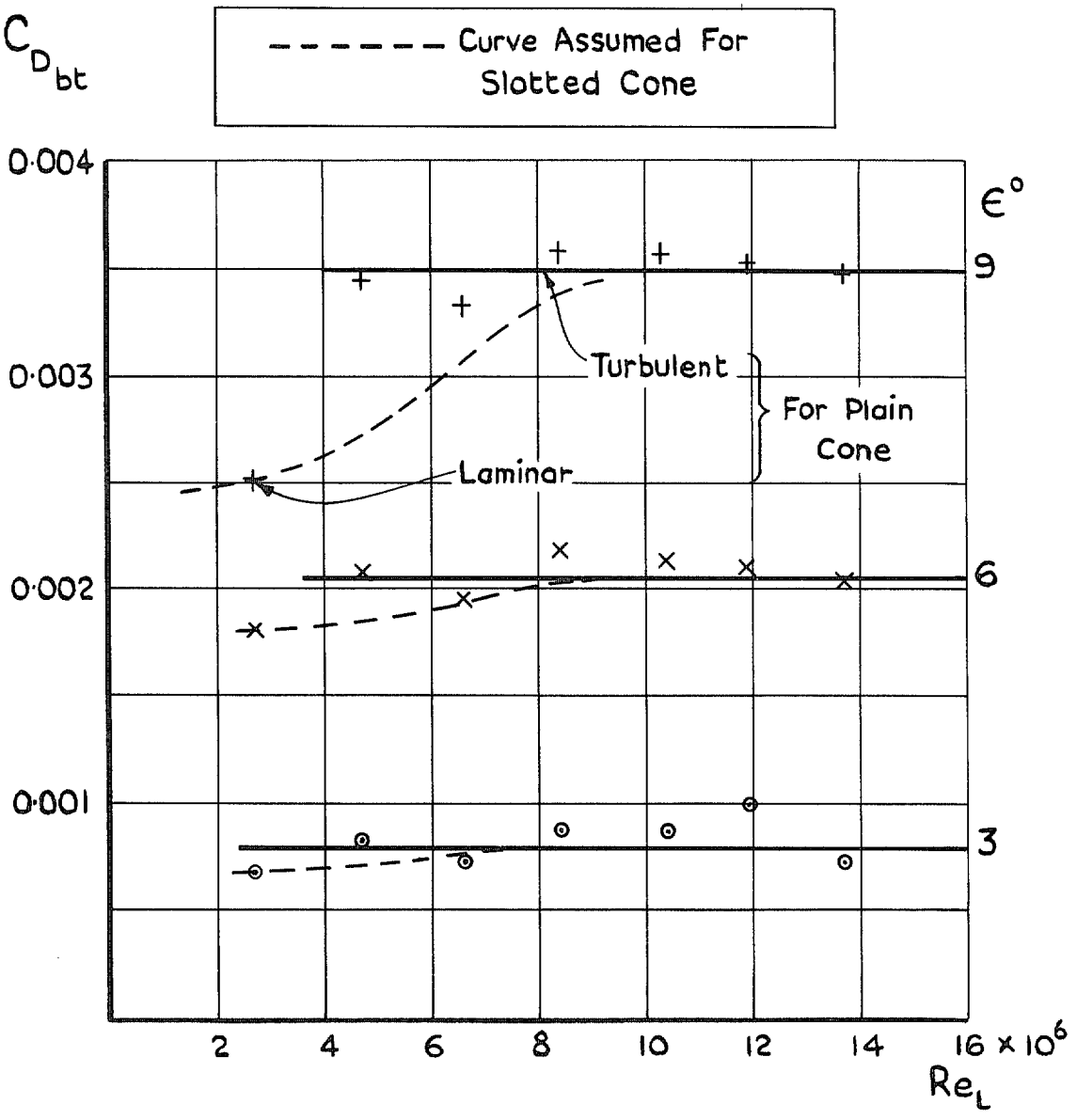

FIG. 39. Assumed variation of boattail drag with Reynolds no. for slotted cone.

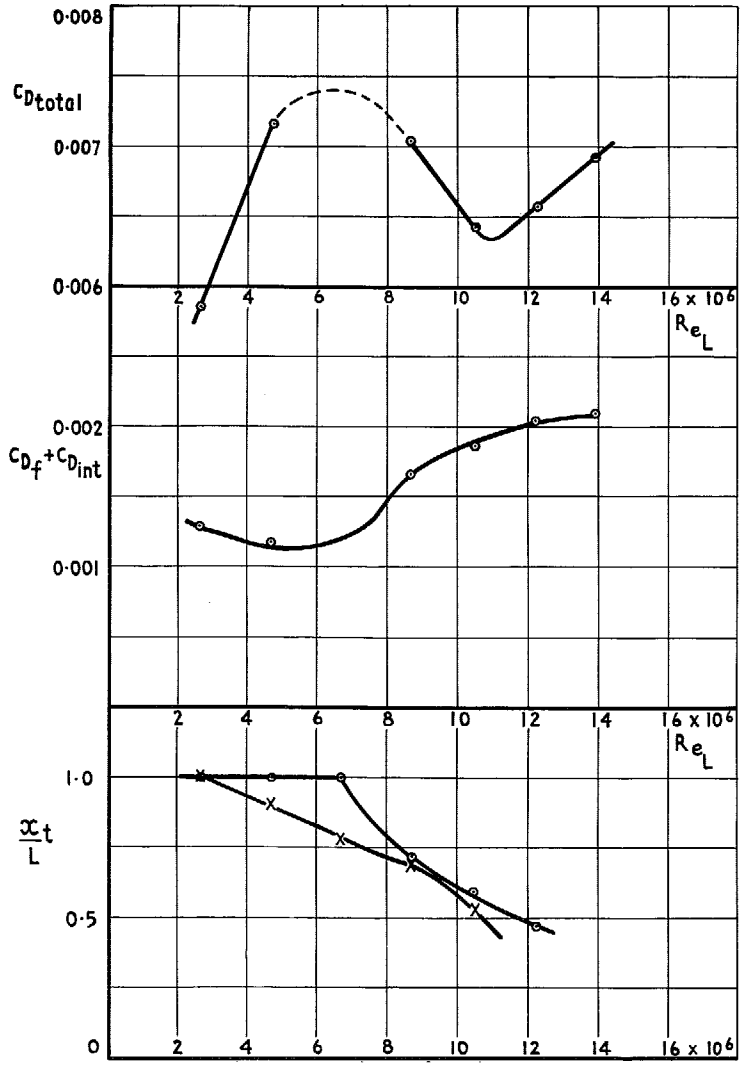

FIG. 40a. Variation of $C_{D_{\text{total}}}$, $C_{D_f} + C_{D_{\text{int}}}$ and $X_{t/L}$ with Reynolds no.
($\varepsilon = 3°$, Plug 2, $A_{ex}/A_{max} = 0{\cdot}0802$.)

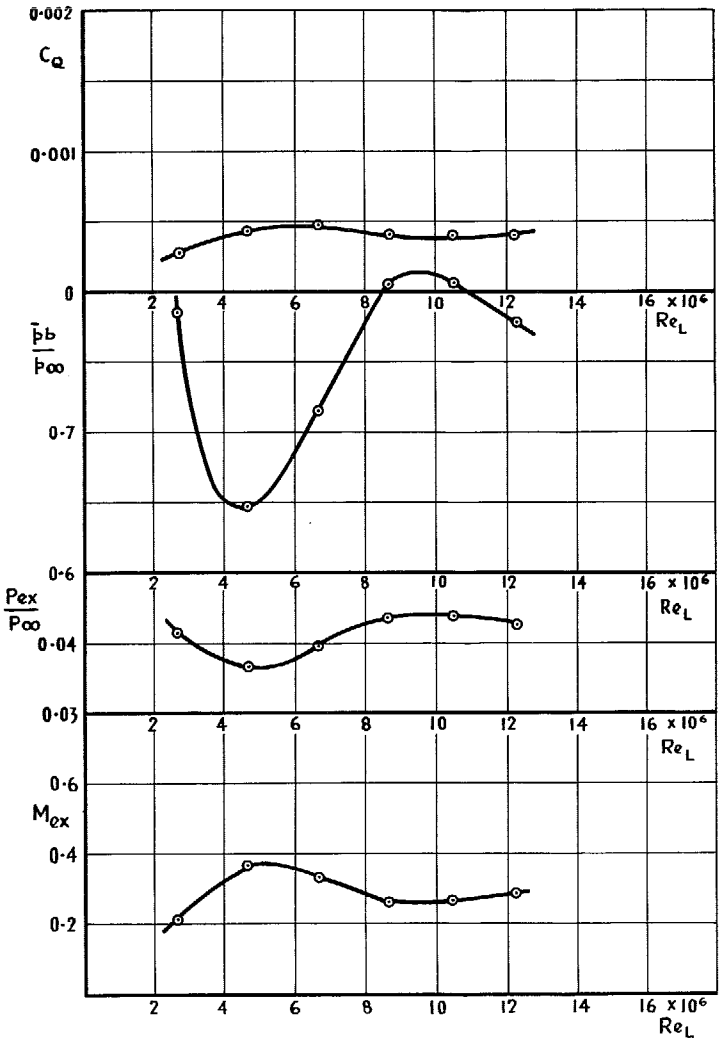

FIG. 40b. Variation of C_Q, $\bar{p}_b/p_\infty$, P_{ex}/P_∞ and M_{ex} with Reynolds no.
($\varepsilon = 3°$, Plug 2, $A_{ex}/A_{max} = 0{\cdot}0802$.)

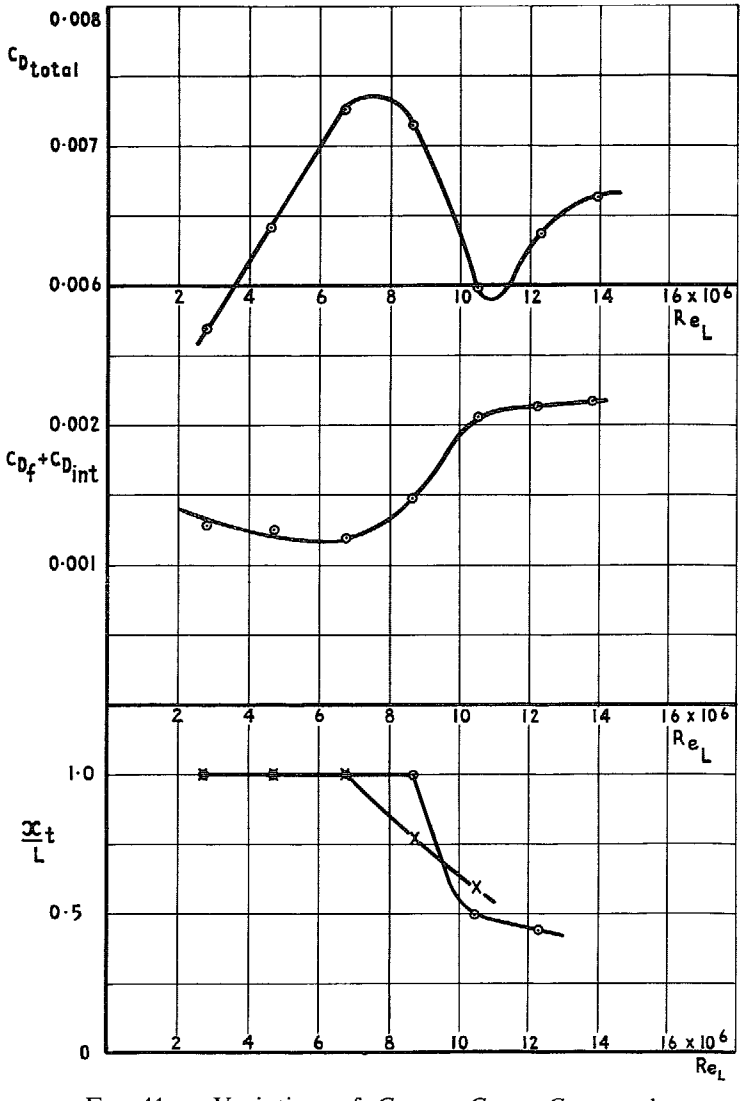

FIG. 41a. Variation of $C_{D_{total}}$, $C_{D_f} + C_{D_{int}}$ and $X_{t/L}$ with Reynolds no.
($\varepsilon = 3°$, Plug 3, $A_{ex}/A_{max} = 0{\cdot}156$.)

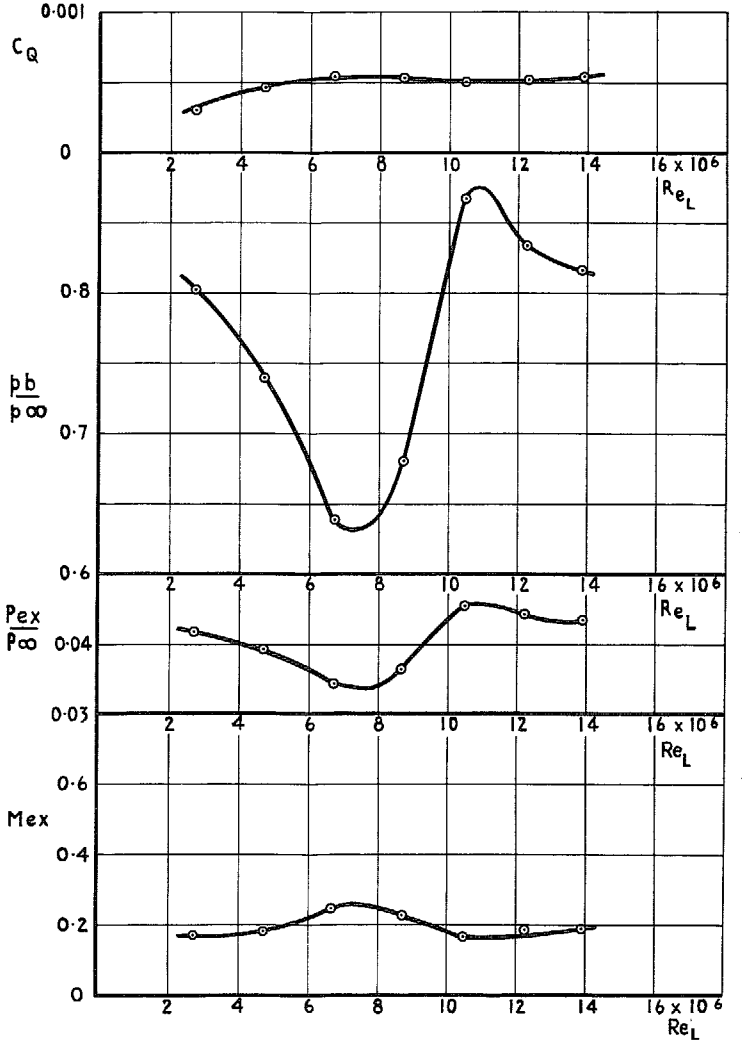

FIG. 41b.

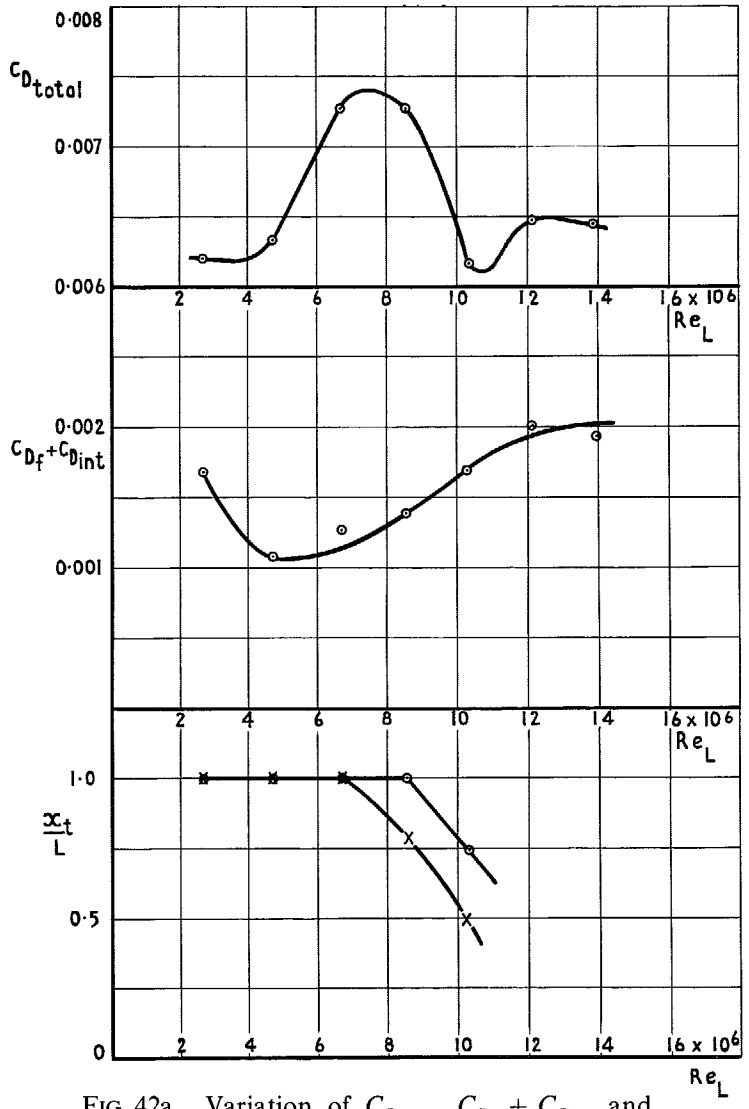

FIG. 42a. Variation of $C_{D_{\text{total}}}$, $C_{D_f} + C_{D_{\text{int}}}$ and $X_{t/L}$ with Reynolds no.
($\varepsilon = 3°$, Plug 5, $A_{ex}/A_{max} = 0{\cdot}308$.)

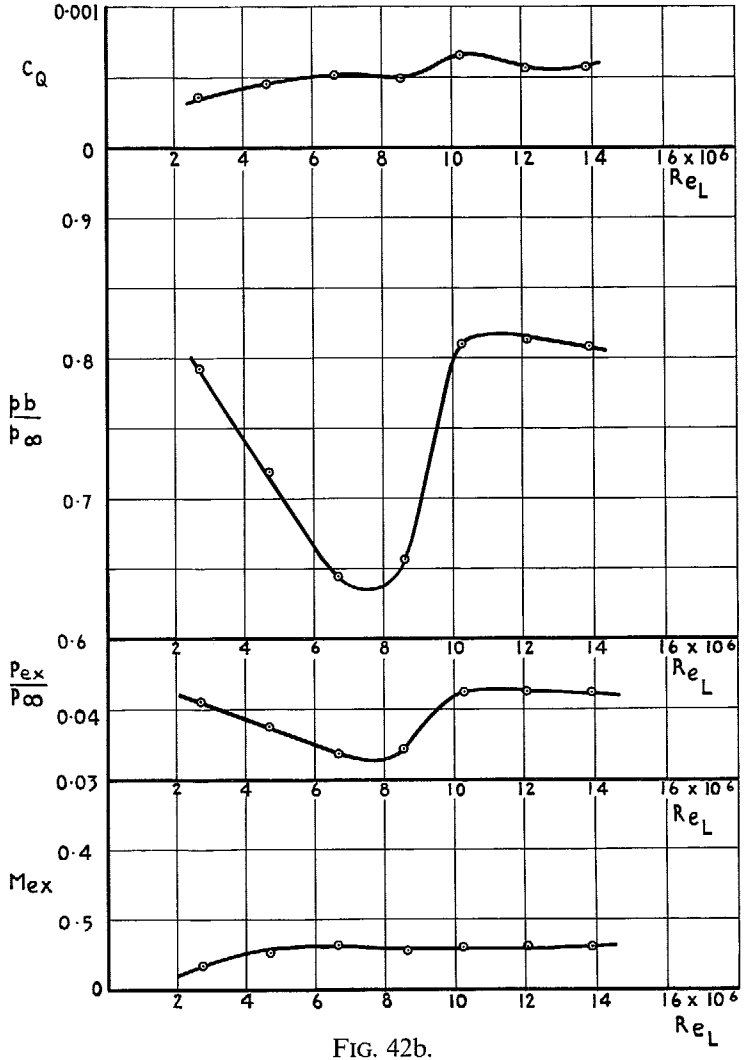

FIG. 42b.

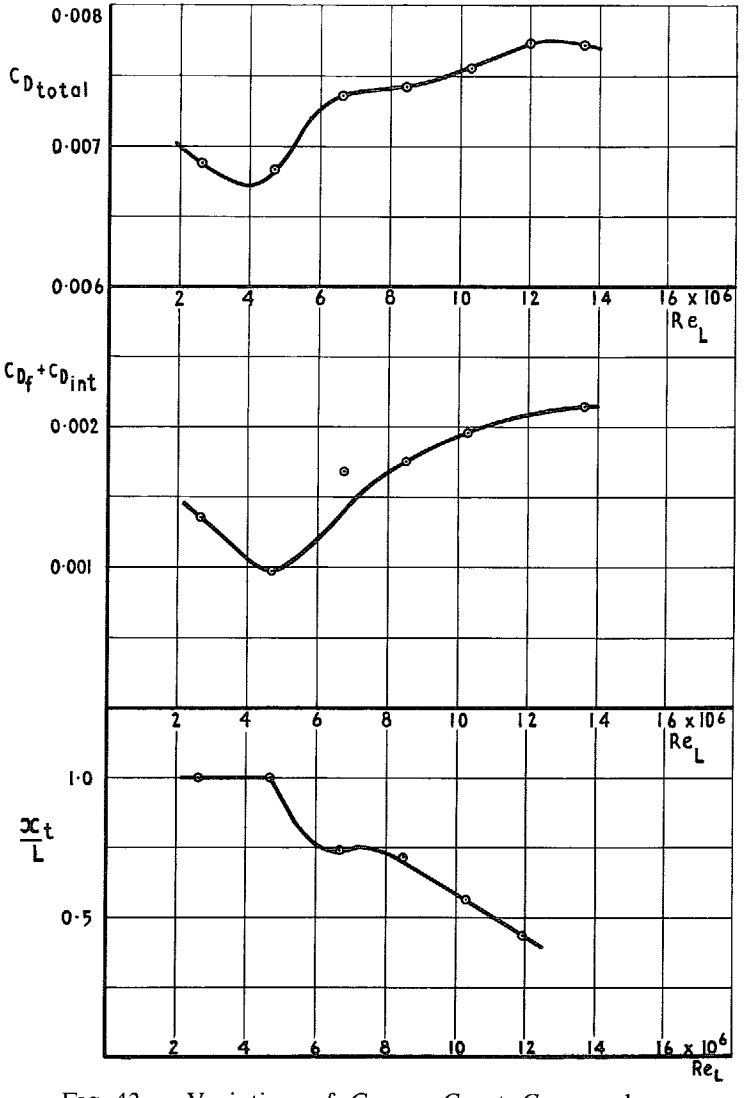

FIG. 43a. Variation of $C_{D_{\text{total}}}$, $C_{D_f} + C_{D_{\text{int}}}$ and $X_{t/L}$ with Reynolds no.
($\varepsilon = 6°$, Plug 2, $A_{ex}/A_{max} = 0{\cdot}0802$.)

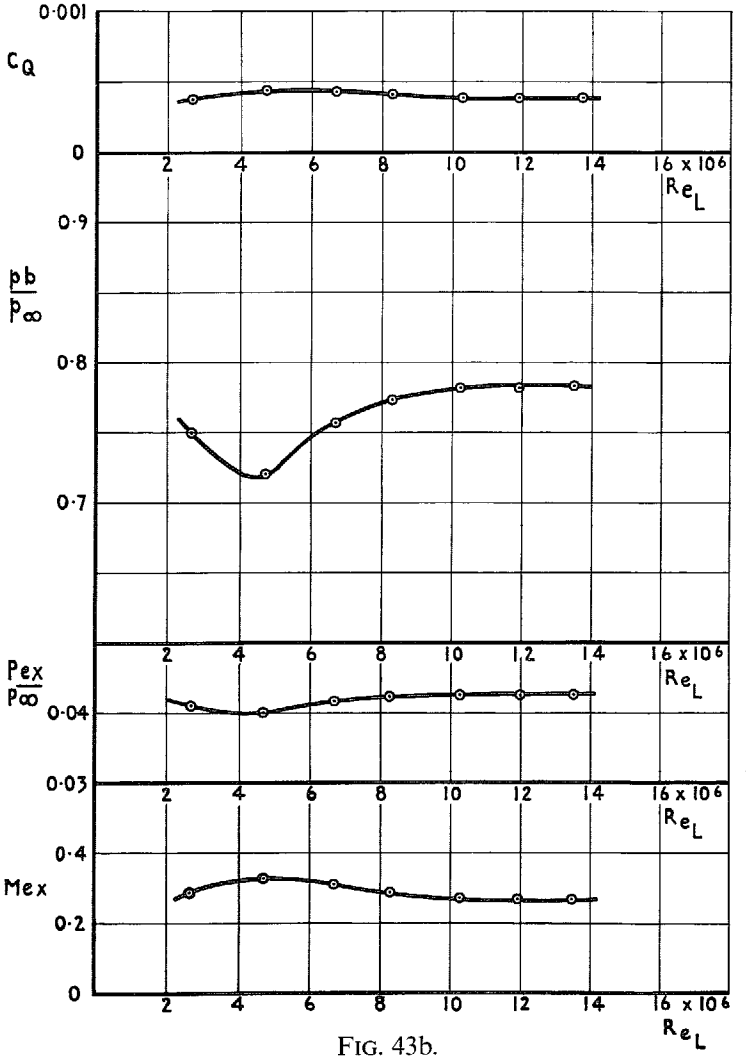

FIG. 43b.

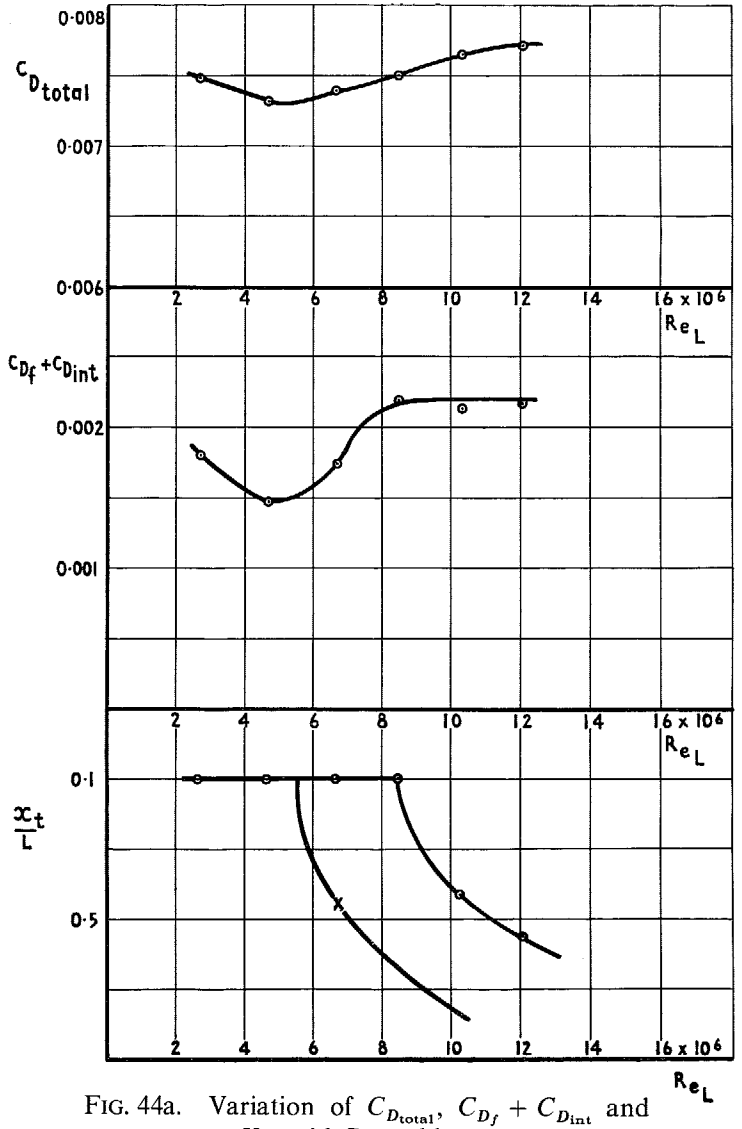

FIG. 44a. Variation of $C_{D_{\text{total}}}$, $C_{D_f} + C_{D_{\text{int}}}$ and $X_{t/L}$ with Reynolds no.
($\varepsilon = 6°$, Plug 3, $A_{ex}/A_{max} = 0{\cdot}156$.)

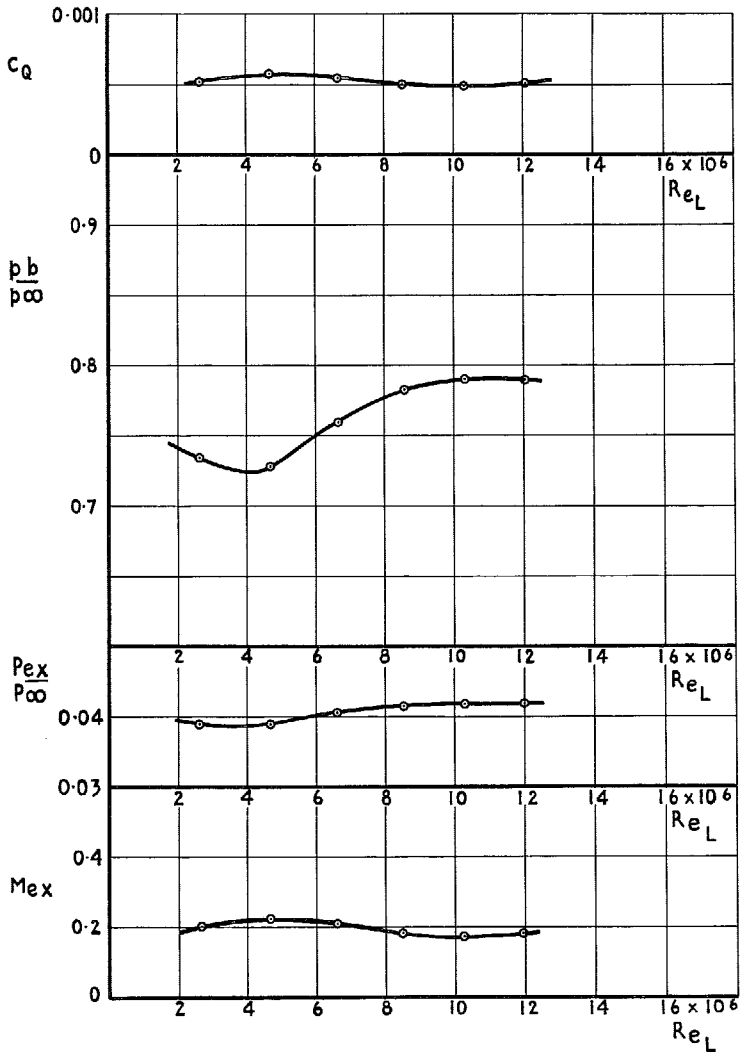

FIG. 44b.

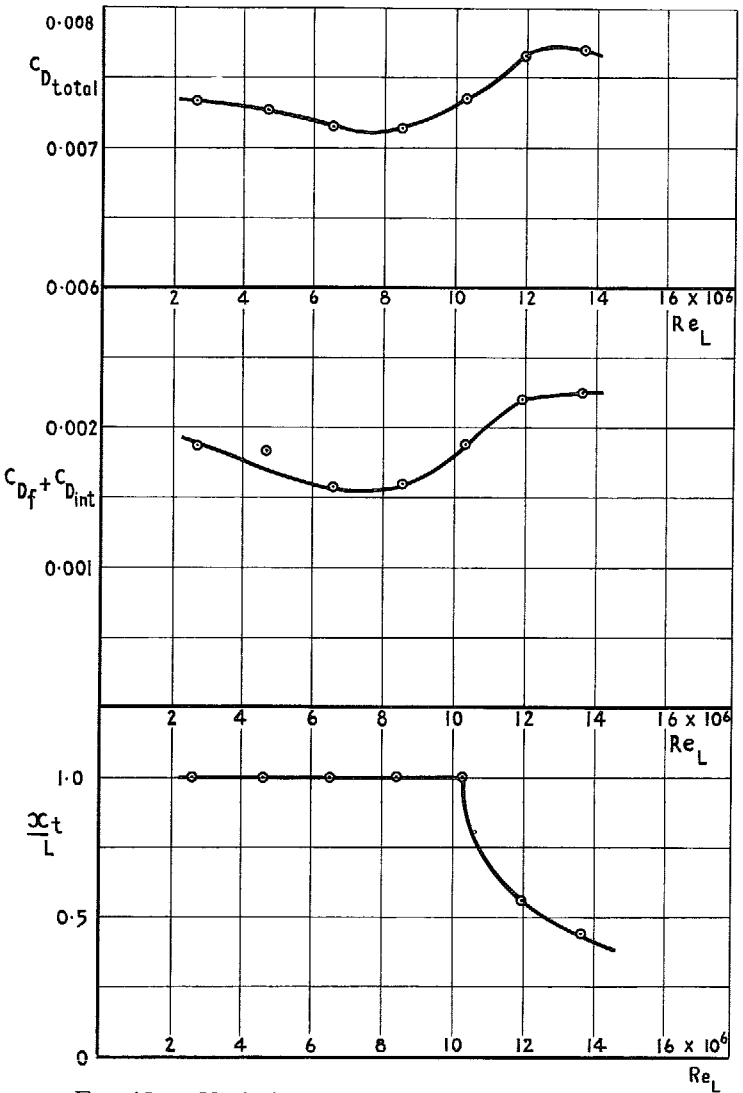

FIG. 45a. Variation of $C_{D_{\text{total}}}$, $C_{D_f} + C_{D_{\text{int}}}$ and $X_{t/L}$ with Reynolds no.
($\varepsilon = 6°$, Plug 5, $A_{ex}/A_{max} = 0{\cdot}308$.)

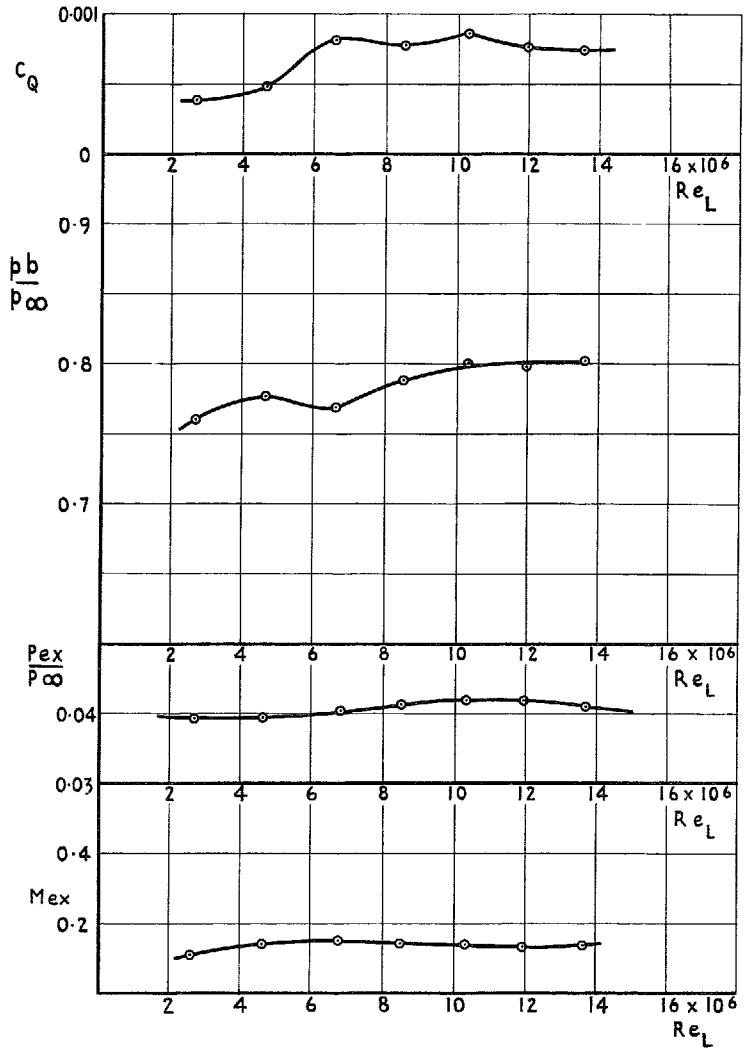

FIG. 45b.

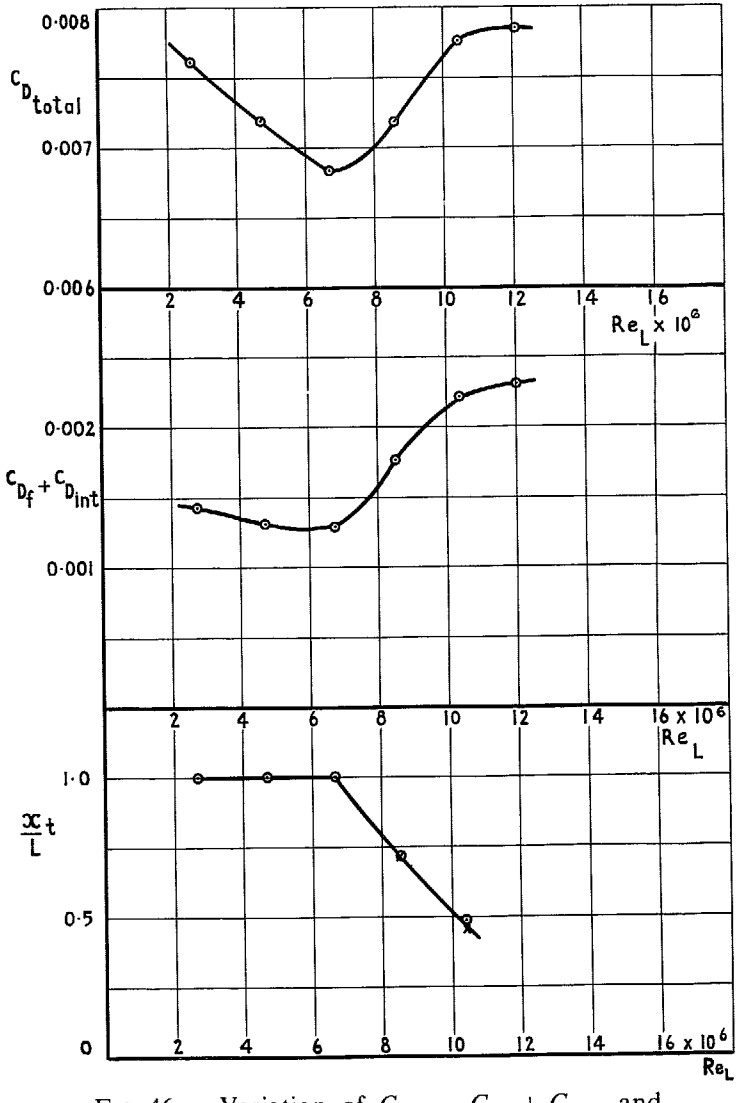

FIG. 46a. Variation of $C_{D_{total}}$, $C_{D_f} + C_{D_{int}}$ and $X_{t/L}$ with Reynolds no.
($\varepsilon = 9°$, Plug 2, $A_{ex}/A_{max} = 0{\cdot}0857$.)

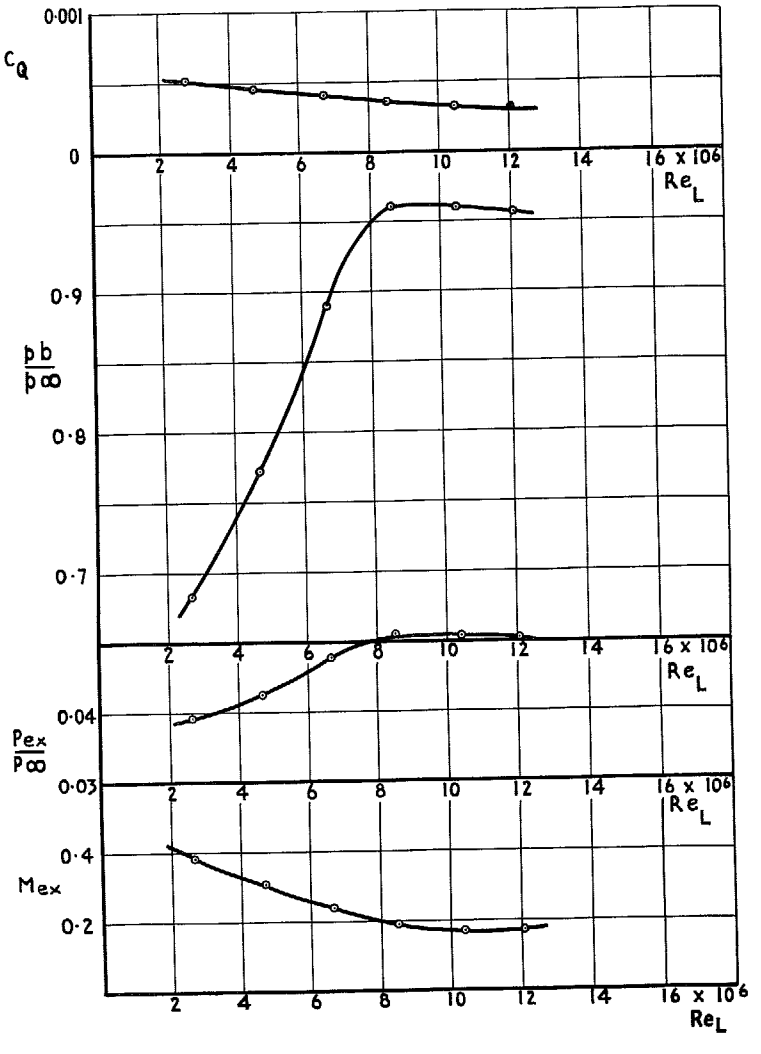

FIG. 46b.

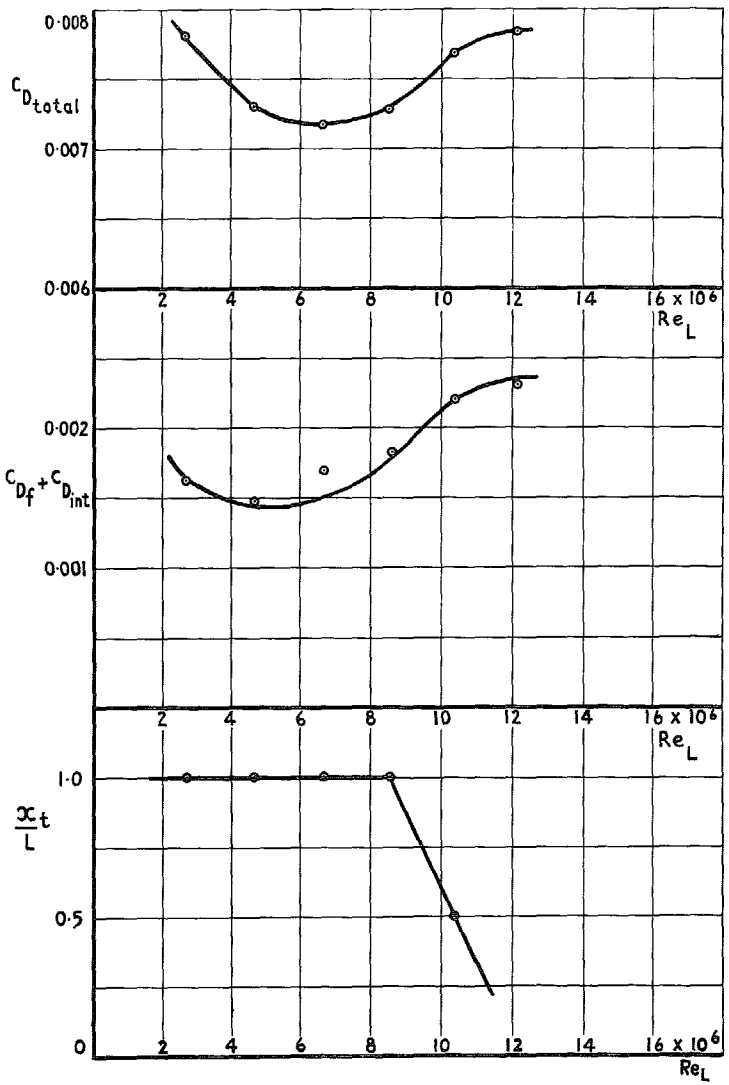

FIG. 47a. Variation of $C_{D_{\text{total}}}$, $C_{D_f} + C_{D_{\text{int}}}$ and $X_{t/L}$ with Reynolds no.
($\varepsilon = 9°$, Plug 3, $A_{ex}/A_{max} = 0{\cdot}167$.)

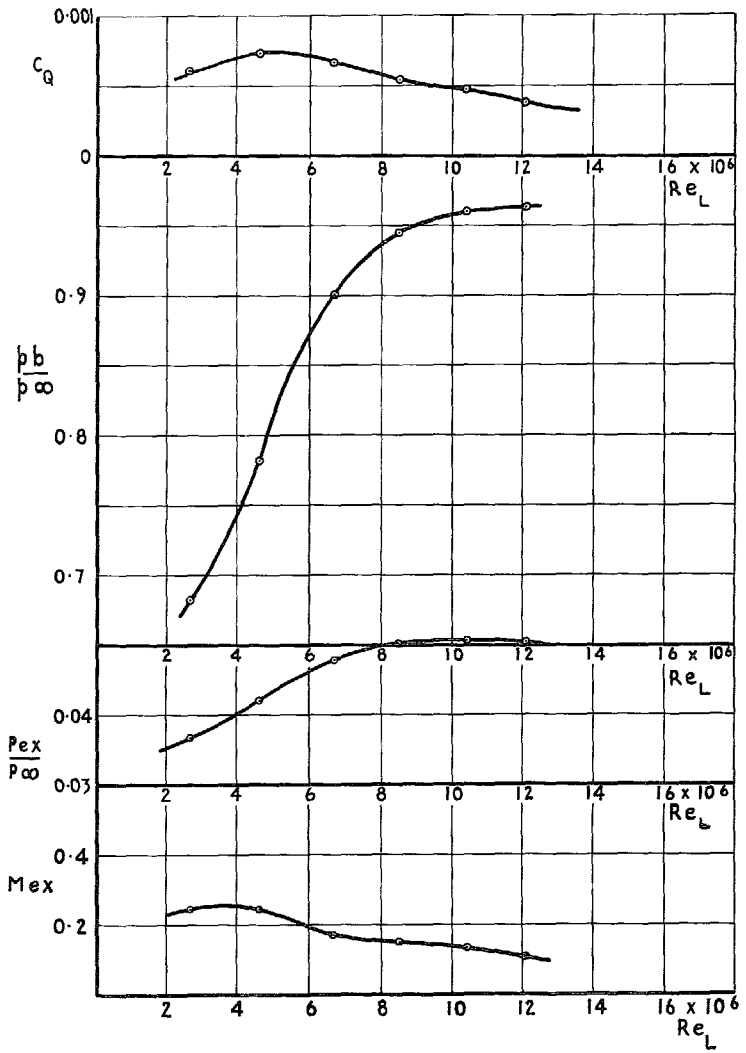

FIG. 47b.

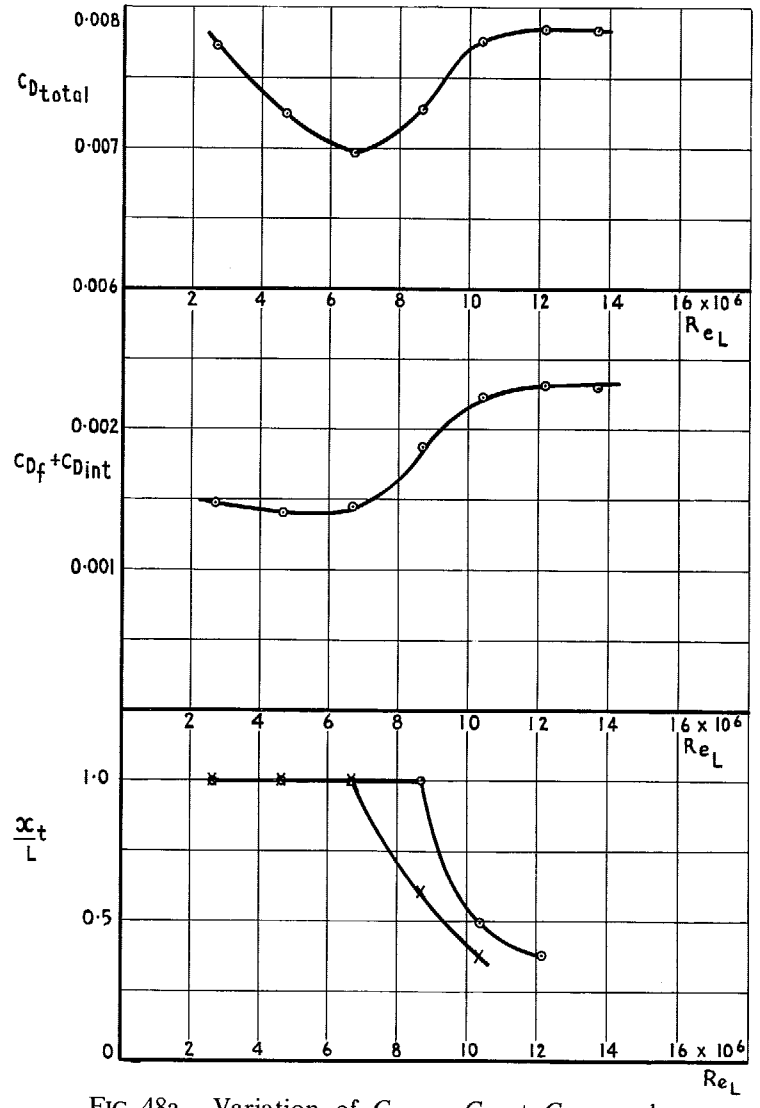

FIG. 48a. Variation of $C_{D_{total}}$, $C_{D_f} + C_{D_{int}}$ and $X_{t/L}$ with Reynolds no.
($\varepsilon = 9°$, Plug 4, $A_{ex}/A_{max} = 0{\cdot}249$.)

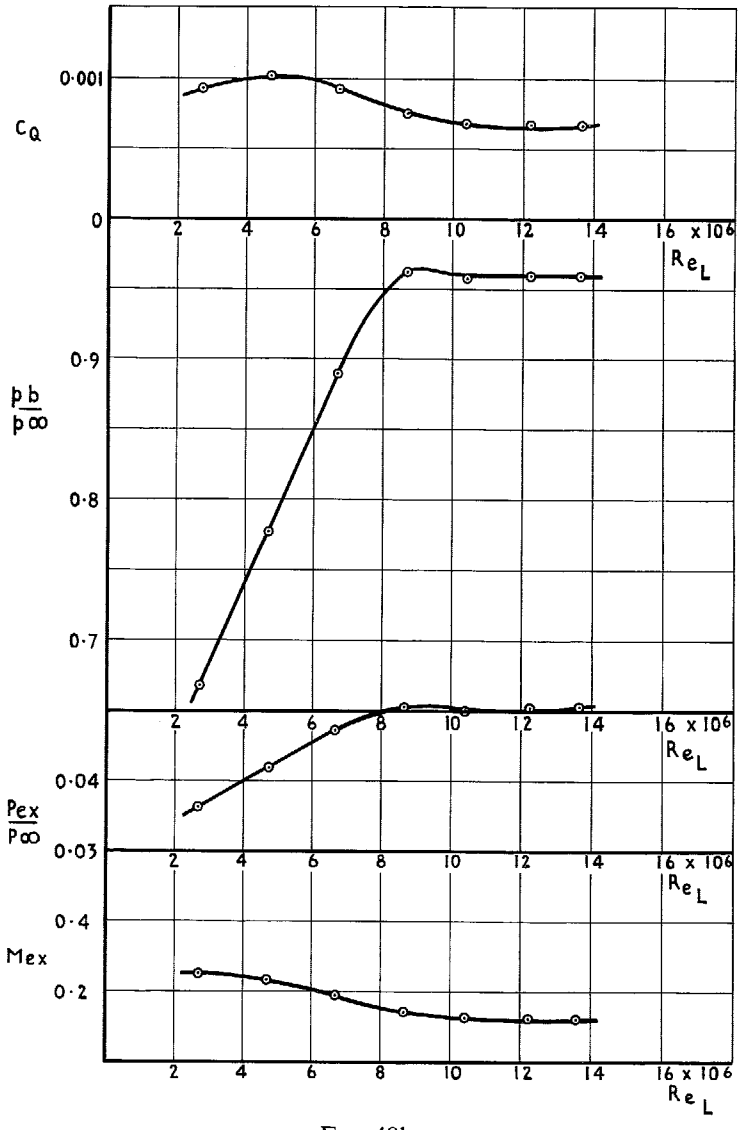

FIG. 48b.

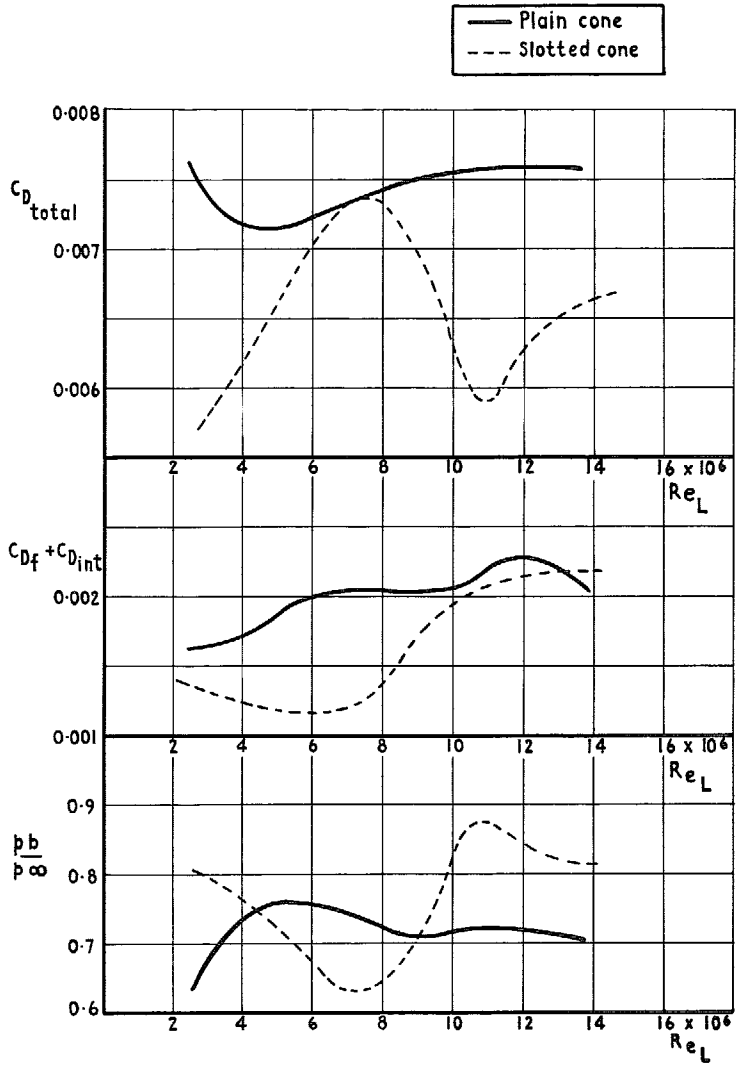

FIG. 49. Comparison of plain and slotted cones with 3° boattail (Plug 3).

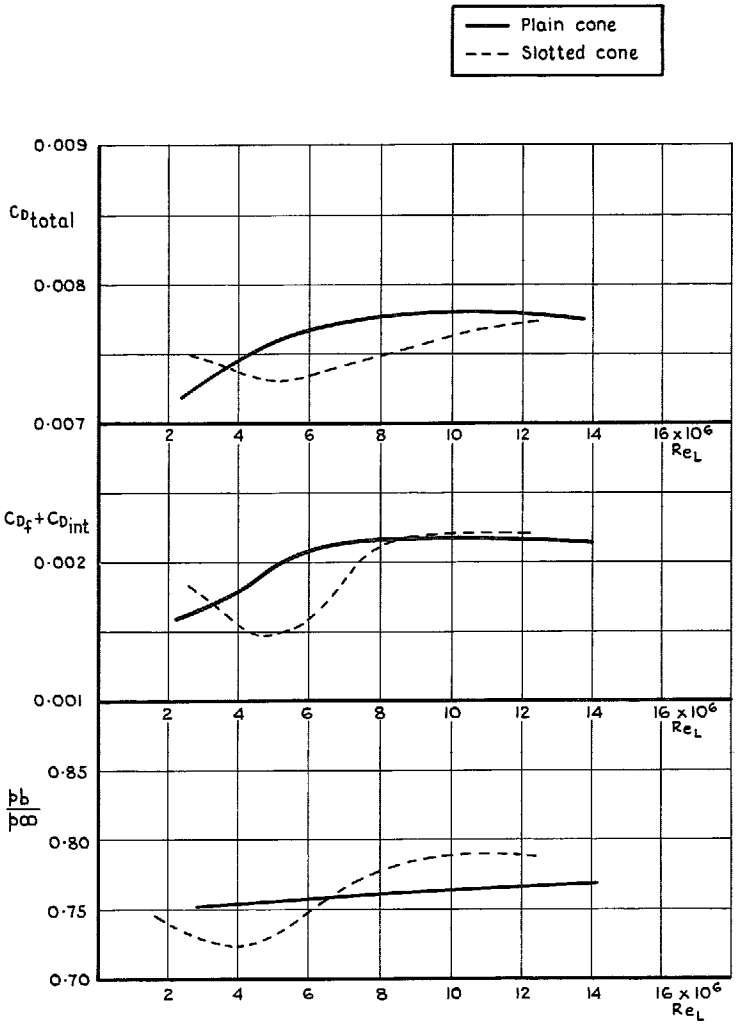

FIG. 50. Comparison of plain and slotted cones with 6° boattail (Plug 3).

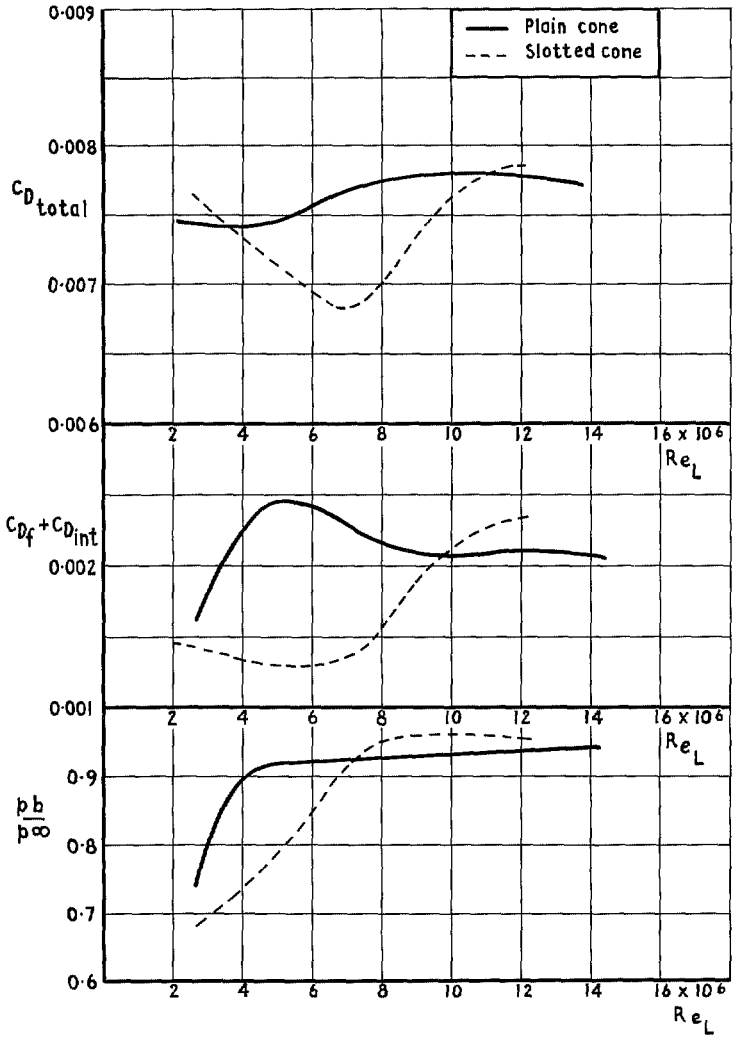

FIG. 51. Comparison of plain and slotted cones with 9° boattail (Plug 2).

Printed in England for Her Majesty's Stationery Office by J. W. Arrowsmith Ltd., Bristol 3.

Dd.135646 K.5.

Published by
HER MAJESTY'S STATIONERY OFFICE

To be purchased from
49 High Holborn, London W.C.1
13a Castle Street, Edinburgh EH2 3AR
109 St. Mary Street, Cardiff CF1 1JW
Brazennose Street, Manchester M60 8AS
50 Fairfax Street, Bristol BS1 3DE
258 Broad Street, Birmingham 1
7 Linenhall Street, Belfast BT2 8AY
or through any bookseller

R. & M. No. 3591

SBN 11 470188 1